

Surface modification of soda-lime-silica glass by superheated steam

Von der Fakultät für Ingenieurwissenschaften
der Universität Bayreuth
zur Erlangung der Würde
Doktor-Ingenieur (Dr.-Ing.)
genehmigte Dissertation

von

Barsheek Roy, M. Tech

aus

Kolkata, India

Erstgutachter: Prof. Dr.-Ing. Stefan Schafföner
Zweitgutachter: Prof. Dr.-Ing. Thorsten Gerdes
Tag der mündlichen Prüfung: 26.04.2024

Lehrstuhl Keramische Werkstoffe
Universität Bayreuth
(2024)

Acknowledgement

It is an absolute pleasure to have this opportunity to convey my heartfelt gratitude to everyone involved as background support for this work. Any support from the perspective of riding the mental and emotional desires outside the academic bubble was particularly valuable.

Sincere regards to my first supervisor, Prof. Dr.-Ing. Stefan Schafföner for his indispensable guidance throughout this memorable journey. Honestly, I feel privileged to have had the solemn opportunity to have his international character by my side. His efforts in my personal development in addition to the academic support is sincerely acknowledged. The contribution of my second supervisor, Prof. Dr.-Ing. Thorsten Gerdes was priceless. His invaluable managerial characteristics of contributing from the viewpoint of any technical support to the overall aspect is highly appreciated.

Special thanks to the colleagues of our group, Keylab Glass Technology, in addition to the other colleagues across different chairs in the entire university for their contributions. I truly appreciate their keen willingness to help whenever needed. Special mention goes to the postdoctoral researcher of our group, Dr.-Ing. Andreas Rosin for sharing his knowledge and experiences, while being compassionate to encouragingly drive me during the lows. Furthermore, the fruitful contribution of the doctoral student, Felix Baier at the Chair of Experimental Physics XI for the XPS measurements is gratefully acknowledged.

The financial support of the 'Bavarian State Ministry of the Environment and Consumer Protection' for the 'VaporCoat' project that I was employed on for three years is gratefully acknowledged.

I find it so necessary to acknowledge the critical role of the people of different nationalities that I met during my travels through the Schengen countries in pursuit of natural, cultural and self-discovery. Converting strangers of different backgrounds into friends and connecting with them was so essential for me to ride through this journey with pleasant memories to cherish.

Eventually, the role of my family back in India inevitably deserves a special mention. I am so grateful to have had their long-distance support.

Abstract

Glass surfaces govern the properties of strength, chemical durability, adhesion and optical quality of glasses. The surface acts as an interfacial site between the surrounding atmosphere and the bulk of the glass network. The reactivity of the interface to a variety of physical and chemical processes is critical to the performance of the material. The influence on the surface structure caused by an external stimulus is intimately correlated to the mechanical properties of glass surfaces. The enhancement of the mechanical properties of glasses such as hardness, scratch resistance and strength, necessitates a comprehensive knowledge of the underpinning relationship between the surface structural and mechanical properties.

The subject of the alteration of the glass network caused by the exposure to liquid water and atmospheric humidity, associated with the degradation of mechanical properties, has received considerable attention in the past. However, the lack of a thorough insight on the fundamental cause of the change in surface mechanical properties of silicate glasses in intimate correlation with the influence on the structural network continues to persist. This research was aimed to bridge the gap in knowledge by elucidating the relationship between the surface structural and mechanical properties of soda-lime-silica (SLS) glass, that finds widespread applications ranging from windows to container bottles. Superheated steam was used as a medium of interaction with the SLS glass surface to study the modification of the surface structural network in correlation to the influence on subsurface hardness. Two categories of SLS glasses, container glass and microscopic glass slide, were used for a comparative study. It was evidenced that the depth of influence of superheated steam was restricted to the near-surface region up to approximately 300 nm below the surface. The subsurface hardness was enhanced by 30% in the container SLS glass when subjected to interaction with superheated steam at sub- T_g temperature of 510 °C for 30 minutes (T_g : glass transition temperature). On the contrary, the subsurface hardness of the other variant of SLS glass (glass slide) merely increased by 4%. Both the glasses were treated by superheated steam at a temperature of 50 °C below the onset of T_g for 30 minutes. These parameters were found to be optimal with respect to the

increment in subsurface hardness associated with the mobility of the glass network. The viscosity at this temperature also facilitated the investigation of the structural changes thoroughly. The striking contrast of the influence on subsurface hardness between the two categories of SLS glasses necessitated a conscientious study of the role of the hydroxyl groups as well as the silicate network connectivity. It was demonstrated that the molecular water associated with a weak hydrogen bond to the bridging oxygen of a silicate ring occupied the interstitial voids within the silica tetrahedral units to contribute to subsurface hardening. The extent of stuffing of the interstitial voids by molecular water was determined by the network rearrangement caused by superheated steam. The diffusion of water molecules was favored by network depolymerization associated with a decrease in subsurface silicate network connectivity. This led to the availability of micro channelized pathways in the near-surface region of the container SLS glass. On the contrary, the SLS glass slide underwent silicate network repolymerization marked by the evidence of an increase in the concentration of bridging oxygens. This obstructed the pathway for the penetration of the water molecules during steam treatment. The difference in the behavior of subsurface silicate network rearrangement was attributed to the initial states of the silicate networks of the surfaces in their pristine states. The untreated SLS container glass had higher concentration of NBOs as opposed to its counterpart, that facilitated further weakening of the network on interaction with superheated steam to decrease the network connectivity.

The other remarkable discovery was related to the susceptibility of the steam-treated glass surface to ageing in ambient atmosphere. It was evidenced that the water molecules linked to the silicate network with weak hydrogen-bonds were vulnerable to escaping either to the outer atmosphere or dissipating to the bulk of the glass network, when subjected to ageing. This was accompanied by a decrease in the subsurface hardness of the container SLS glass. The occurrence of the former event of the escape of the entrapped water molecules to the outer atmosphere may be prevented by deposition of thin film coating on the glass surface.

Overall, it was discovered that the silicate network connectivity in combination with the interstitial voids within the silica tetrahedral units play a decisive role in governing the subsurface hardness of SLS glass. The role of stuffing of the interstitial voids with

hydrogen-bonded water molecules to contribute to subsurface hardening forges the basis of regarding these voids to be detrimental to the propagation of surface-initiated cracks to the depth of the glass network.

Kurzfassung

Glasoberflächen bestimmen die Eigenschaften wie Festigkeit, chemische Beständigkeit, Haftung und optische Qualität von Gläsern. Die Oberfläche fungiert als Grenzfläche zwischen der umgebenden Atmosphäre und dem Glasnetzwerk. Die Reaktivität der Grenzfläche ist bei einer Vielzahl von physikalischen und chemischen Prozessen entscheidend für die Leistungsfähigkeit des Materials. Die Beeinflussung der Oberflächenstruktur durch einen externen Stimulus steht in engem Zusammenhang mit den mechanischen Eigenschaften der Glasoberfläche. Die Verbesserung der mechanischen Eigenschaften von Gläsern, wie z. B. Härte, Kratzfestigkeit und Festigkeit, erfordert ein umfassendes Wissen über die zugrunde liegende Beziehung zwischen der Struktur des Glases an der Oberflächen sowie im Volumen.

Die durch die Einwirkung von flüssigem Wasser und Luftfeuchtigkeit verursachte Veränderung des Glasnetzwerks, die mit einer Verschlechterung der mechanischen Eigenschaften einhergeht, hat in der Vergangenheit große Aufmerksamkeit erregt. Es fehlt jedoch nach wie vor ein tiefer gehender Einblick in die grundlegende Ursache für die Veränderung der mechanischen Oberflächeneigenschaften von Silikatgläsern in Zusammenhang mit der Netzwerkstruktur des Glases. Diese Forschungsarbeit schließt diese Wissenslücke, indem sie die Beziehung zwischen der Oberflächenstruktur und den mechanischen Eigenschaften von Glas aufklärt. Untersucht wurde Natron-Kalk-Silikat-Glas (*engl.* soda-lime silicate (SLS) glass), das Anwendung zum Beispiel als Fenster- oder Behälterglas findet. In der vorliegenden Arbeit wurde überhitzter Wasserdampf als Medium für die Interaktion mit der SLS-Glasoberfläche verwendet, um die Veränderung des strukturellen Oberflächennetzwerks in Korrelation mit dem Einfluss auf die unter der Oberfläche liegende Härte zu untersuchen. Untersucht wurde zwei verschiedene Glasprodukte, zum einen ein grünes Flaschenglas, zum anderen flache Glasobjektträger für die Mikroskopie. Die Untersuchungen zeigten, dass der Einfluss des überhitzten Dampfes auf einen oberflächennahen Bereich bis etwa 300 nm unter der Oberfläche beschränkt ist. Die Härte des unter der Oberfläche liegende Behälterglases konnte um 30 % erhöht werden, wenn es 30 Minuten lang bei einer Temperatur unterhalb der Glasübergangstemperatur (T_g : 560 - 575 °C) mit überhitztem Dampf beaufschlagt wurde.

Im Gegensatz dazu erhöhte sich unter denselben Bedingungen die Oberflächenhärte des Glasobjektträgerglases lediglich um 4 %. Die Parameter der Dampfbehandlung erwiesen sich als optimal im Hinblick auf die Zunahme der Oberflächenhärte in Verbindung mit der Mobilität des Glasnetzwerks. Auch die Viskosität bei dieser Temperatur erleichterte die Untersuchung der strukturellen Veränderungen. Der auffällige Unterschied zwischen den beiden untersuchten SLS-Gläsern in Bezug auf den Einfluss auf die Oberflächenhärte erforderte eine sorgfältige Untersuchung der Rolle der Hydroxylgruppen sowie der Konnektivität des Silikatnetzwerks. Dabei konnte gezeigt werden, dass das molekulare Wasser, das mit einer schwachen Wasserstoffbindung an den verbrückenden Sauerstoff eines Silikatrings verbunden ist, die Zwischenräume innerhalb der tetraedrischen Siliziumdioxideinheiten ausfüllt und so zur Oberflächenhärtung beiträgt. Der Grad der Füllung der interstitiellen Hohlräume durch molekulares Wasser wurde durch die Änderungen des Glasnetzwerks durch den überhitzten Dampf bestimmt. Die Diffusion der Wassermoleküle wurde durch eine Depolymerisation des Netzwerks begünstigt, die mit einer Abnahme der Konnektivität des Silikatnetzwerks unter der Oberfläche einherging. Dadurch wurden Mikrokanälen im oberflächennahen Bereich des Behälterglases geschaffen. Im Gegensatz dazu kam es auf der Objektträger-Glasplatte zu einer Repolymerisation des Silikatnetzwerks, gekennzeichnet durch einen Anstieg der Konzentration von brückenbildenden Sauerstoffbindungen (*engl.* bridging oxygen, BO). Somit wurde der Weg für das Eindringen von Wassermolekülen während der Dampfbehandlung versperrt. Dieser Unterschied bei der Umlagerung des Silikatnetzwerks unter der Oberfläche wurde auf die Ausgangszustände der Silikatnetzwerke an der Oberfläche zurückgeführt. Das unbehandelte Behälterglas wies im Gegensatz zu seinem Gegenstück eine höhere Konzentration an nicht-brückenbildenden Sauerstoffionen (*engl.* non-bridging oxygen, NBO) auf, was eine weitere Schwächung des Netzwerks bei der Interaktion mit überhitztem Dampf begünstigte und die Netzwerkkonnektivität verringerte.

Die andere bemerkenswerte Änderung betraf die Anfälligkeit der dampfbehandelten Glasoberfläche für die Alterung in der Umgebungsatmosphäre. Es konnte nachgewiesen werden, dass diejenigen Wassermoleküle, die über schwache Wasserstoffbrückenbindungen mit dem Silikatnetz verbunden sind, bei der Alterung entweder in die Umgebungsatmosphäre entweichen oder sich im Volumen des

Glasnetzwerkes verteilen können. Dieser Vorgang ging mit einer Abnahme der Oberflächenhärte des SLS-Glases einher.

Die Konnektivität des Silikatnetzwerks spielt in Kombination mit den Zwischenräumen innerhalb der Silikat-Tetraedereinheiten eine entscheidende Rolle bei der Steuerung der Oberflächenhärte von SLS-Glas. Die Tatsache, dass die Füllung der interstitiellen Hohlräume mit wasserstoffgebundenen Wassermolekülen zur Oberflächenhärtung beiträgt, legt zudem den Schluss nahe, dass diese Hohlräume der Ausbreitung oberflächeninitiiertter Risse in die Tiefe des Glasnetzwerks abträglich sind.

Table of Contents

Acknowledgement	3
Abstract	4
Kurzfassung	7
Motivation	12
Chapter 1 — State of the art	14
1.1 Silicate network connectivity.....	14
1.2 Introduction to glass surface.....	17
1.2.1 Surface silanol groups.....	17
1.2.2 Near-surface structure.....	21
1.2.2.1 Investigation of the near-surface structure by XPS.....	22
1.2.2.1.1 Working principle of XPS.....	23
1.2.2.1.2 Application of XPS to glass surface.....	28
1.2.3 Surface flaws.....	30
1.2.4 Surface mechanical properties.....	32
1.3 Glass surface corrosion.....	38
1.3.1 Surface degradation by liquid water.....	38
1.3.2 Surface degradation by atmospheric influence.....	40
1.3.3 Surface degradation under hydrothermal condition.....	42
1.4 Strengthening and hardening of silicate glasses.....	43
1.4.1 Strengthening techniques.....	43
1.4.2 Hardening techniques.....	46
Chapter 2 — Methodology	48
2.1 Characteristics of as-received SLS glasses.....	49
2.2 Experimental setup of superheated steam treatment.....	51
2.3 Characterization techniques.....	52
2.3.1 Surface mechanical properties.....	52
2.3.1.1 Hardness.....	52
2.3.1.2 Scratch test.....	53
2.3.2 Surface structural network.....	53
2.3.2.1 ATR-IR.....	53
2.3.2.2 XPS.....	54
2.3.2.3 AFM.....	55
2.3.3 Bulk structural network.....	55
2.3.3.1 Solid-state ²⁹ Si NMR.....	55
Chapter 3 — Results and Discussion	56
3.1 Influence of superheated steam on surface mechanical properties.....	56
3.1.1 Subsurface hardness.....	56
3.1.2 Surface scratch resistance.....	60

3.2 Influence of superheated steam on surface structure.....	61
3.2.1 Hydroxyl groups.....	61
3.2.2 Subsurface silicate network connectivity.....	65
3.2.2.1 Relationship between silicate network connectivity and hardness.....	68
3.2.2.2 Relationship between silicate network connectivity and scratch resistance.....	77
3.3 Modification of surface topography.....	79
3.4 Alteration in surface wettability.....	82
3.5 Distribution of Q ⁿ species in the bulk silicate network.....	83
3.6 Effect of ageing in ambient atmosphere.....	85
3.7 Surface structural schematics.....	89
Chapter 4 — Conclusion and Outlook	93
4.1 Conclusion	93
4.2 Outlook.....	97
References.....	98
Appendix A1.....	109
Appendix A2.....	118
List of Figures.....	120
List of Tables.....	124
List of publications.....	125
Curriculum Vitae.....	126

Motivation

Glass surface is susceptible to incessant interaction with ambient atmosphere to affect the structural chemistry. The instantaneous state of the surface prior to an event determines the fate of the event. Adsorption of water molecules from the ambient atmosphere serves as a paradigm of a ubiquitous event. The interfacial characteristics influenced by the surface structural chemistry govern the overall performance of the material — defined by its chemical durability, corrosion resistance, optical and mechanical properties. This necessitates a thorough understanding of the underpinning surface structural chemistry of glasses.

Soda-lime-silica (SLS) glass serves a broad spectrum of societal materialization, ranging from window glasses to container bottles. The broad field of its application raises the need for an optimum performance with respect to abating the brittle behavior that restricts its failure strength to three orders of magnitude below the theoretical strength. The mechanical properties of SLS glasses are intimately related to the structural network. However, there exists a lack of a thorough insight on the relationship between the surface structural and mechanical properties. This study endeavors to bridge the gap in knowledge with an attempt to draw a correlation of the modification in surface mechanical properties in response to the rearrangement in the subsurface silicate network. The alteration of the silicate structure caused by the influence of aqueous media and atmospheric humidity was a subject of considerable research in the past with the outcome of the corrosion mechanisms. Furthermore, hydrothermal treatment of SLS glass around 150 °C reportedly had negative impact with respect to a decrease in subsurface hardness. The absence of any comparable attention to the interaction of the SLS surface with superheated steam in the vicinity of the glass transition temperature (T_g) is one of the key sources of motivation of this work. The variation in surface mechanical properties influenced by the alteration in surface structure in response to the interaction with superheated steam was studied. Surface-sensitive spectroscopic techniques were used to draw complimentary evidence of the influence on surface nanostructure. The configuration of molecular water in the glass network was discovered on the basis of its influential role on surface structural and mechanical properties. Additionally, the effect of

ambient ageing on the alteration of the surface characteristics was investigated to discover the detrimental effect of surface degradation caused by atmospheric influence.

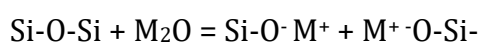
A comprehensive study of the influence of superheated steam on the surface structural and mechanical properties is presented in this thesis with an attempt to formulate a model of the surface structure. The modification of the surface structure of SLS glass is schematically represented, based on the fundamental relationship of mechanical-structural property. The discovery of the contribution of the entrapped water molecules within the interstitial voids of the silica tetrahedral network accentuated the detrimental role of the free volume to the propagation of a crack front until brittle failure. This contributed to the realization of the importance of stuffing of these voids to enhance the mechanical properties of SLS glasses.

1 State of the art

The primary goal of this chapter is to familiarize the reader with the version of the surface structure of soda-lime-silica (SLS) glass that is currently accepted. The near-surface region has received significant attention to highlight its importance in controlling the mechanical properties of glasses. An introduction to the glass surface is presented in addition to the techniques of characterizing the surface structure. The efficacy of X-ray photoelectron spectroscopy (XPS) in characterizing the surface structure deservingly found columns of a separate sub-section. The susceptibility of the glass surface to corrosion in aqueous media and ambient atmosphere is presented before summarizing the methods of strengthening and hardening of silicate glasses.

1.1 Silicate network connectivity

The backbone of the structure of soda-lime-silica (SLS) glass consists of silica tetrahedral network of SiO_4 units [1]. These SiO_4 tetrahedra share corners with each other to form a continuous, three-dimensional network that lacks periodicity. The incorporation of alkali and alkaline earth modifiers such as Na_2O , CaO , K_2O etc. to the raw batch of silica sand reduces the melting point. The network modifiers reduce the degree of connectivity of the silicate structure by replacing the bridging oxygens (BOs) by non-bridging oxygens (NBOs). Fused quartz glass (100% silica) contains silica tetrahedral network with four BOs attached to each silicon atom, each BO being shared by two silicon atoms. The alkali network modifiers enter the silicate structure of SLS glass as singly charged cations (e.g., Na^+ , K^+) to occupy the interstitial sites [2]. The positive charge is satisfied by an ionic bond to an oxygen atom. This is accomplished by breaking a bridge to attach an oxygen provided by the alkali oxide (M_2O) to the broken bridge. This is illustrated by the reaction below:



Thus, each alkali cation is expected to create one non-bridging oxygen (NBO). Each alkaline earth cation (e.g. Ca^{2+}) creates two NBOs to ensure the charge neutrality. The creation of NBO reduces the degree of silicate network connectivity to promote the mass transport related properties such as fluidity (inverse of viscosity), diffusion, electrical

conduction, chemical corrosion. The structure acquires the freedom to expand, associated with an increase in thermal expansion coefficient. A schematic representation of the structure of SLS glass with modifier cations occupying the interstitial sites is shown in Figure 1.1.

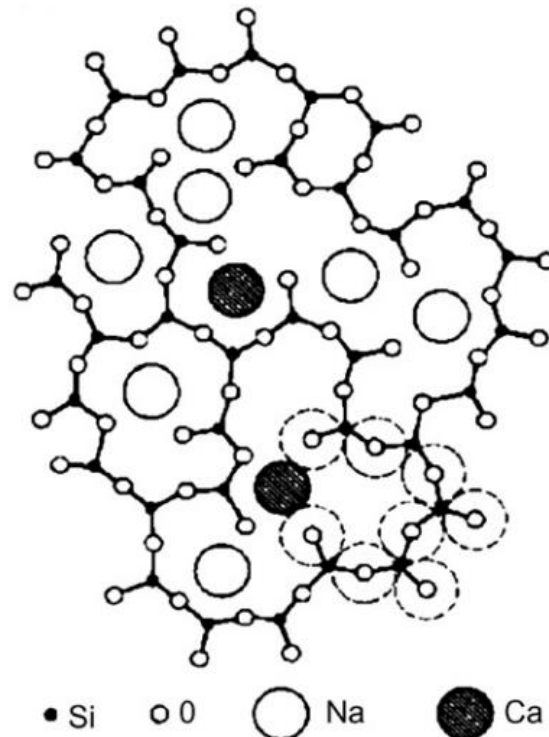


Figure 1.1. Two-dimensional schematic representation of soda-lime-silica glass structure. A fourth oxygen would be located above each silicon atom in the three-dimensional structure [1]. Reproduced with permission from the Royal Society of Chemistry.

The progressive addition of network modifiers to the silica tetrahedral network of SLS glass depolymerizes the network, associated with increase in the concentration of NBOs. The local coordination of a silica tetrahedral unit is designated by Q^n , where Q refers to the SiO₄ tetrahedron (Q) with 'n' bridging oxygens.

Magic angle spinning nuclear magnetic resonance (MAS NMR) is a powerful tool to elucidate the local environment of the various nuclei in the glass structure [3, 4, 5, 6, 7, 8]. In an NMR experiment, a nucleus possessing a magnetic moment is spun at an angle θ to an externally applied magnetic field H_0 , causing the nucleus to precess at Larmor frequency about the field axis. An oscillating electromagnetic field of the same frequency

is then allowed to interact. The resulting nuclear resonance then causes absorption of energy from the oscillating field proportional to the Boltzmann distribution of the nuclear spin population and the effective nuclear relaxation times. The NMR spectra are affected by the chemical shift anisotropy interaction resulting from the shielding of H_0 by the electrons surrounding the resonating nucleus. Any change in the local electron density around the nucleus e.g., change in coordination number can be detected. When $\theta = 54.74^\circ$ ($3\cos^2\theta - 1 = 0$), the peak-broadening interactions in the NMR spectra are removed to narrow the linewidth [3], that justifies the term 'magic angle'. In SLS glasses, the chemical anisotropy on ^{29}Si yields information regarding the second neighbors, particularly the identification of BOs and NBOs. The local configuration around the silicon atom, expressed as Q^n units ($n = 0$ to 4) is characterized to determine the extent of network depolymerization in the overall silicate structure. The chemical shift corresponding to around -93 ppm with respect to the standard reference of trimethylsilane (TMS) indicates the Q^3 species, while Q^4 species are identified by a chemical shift of around -106 ppm. The percentage abundance of each Q^n species can be calculated by the normalized integrated peak areas of the curve-fitted NMR spectra.

Raman spectroscopy is one of the popular analytical tools of investigating the silicate structure of glasses [9, 10, 11, 12, 13]. It is an inelastic light scattering phenomenon. The frequency of the monochromatic light used for excitation changes on interaction with the glass sample. The effect probes the vibrational levels of specific groups of atoms or ions. Photons of the laser light are taken up by the sample into a non-stationary, very short-lived virtual state ($\sim 10^{-15}$ s) followed by instantaneous reemission. The frequency of the reemitted photons is shifted up (anti-Stokes Raman effect) or down (Stokes effect) relative to the original single frequency, by a value called the Raman shift. This, in turn, provides information about vibrational, rotational, and other low frequency transitions in molecules or molecular groupings of the sample being analyzed. It is an essential tool of characterizing the Q^n species in the sub-surface region on the scale of micrometers below the glass surface [14]. The Raman spectrum between 150 and 1350 cm^{-1} is associated with the vibrations of the silicate structure consisting of two main regions: bending vibrations within inter-tetrahedral linkages corresponding to the low frequency (LF) region between 300 and 600 cm^{-1} ; and Si-O stretching vibrations of the depolymerized silicate species corresponding to the high frequency (HF) region between 900 and 1300 cm^{-1} [11, 12, 13]. The concentrations of the individual Q^n species can be calculated by

deconvoluting the HF band to determine the overlapping peaks. The contributions of these overlapping peaks are assigned to specific Q^n species to calculate the corresponding concentrations by the normalized integrated peak areas. An empirical formula generally used for evaluating the degree of polymerization of the glass network uses the ratio between the LF and HF band areas [15]. The Q^3 species generally dominate the bulk structure in SLS glasses with three bridging oxygens and one non-bridging oxygen linked to each silica tetrahedral unit. However, the surface structure of SLS glasses differ from the bulk, owing to the inevitable presence of silanol groups linked to NBOs, representative for a weaker network connectivity. The following section presents an introduction to the surface network.

1.2 Introduction to glass surface

Glass surfaces control the properties of strength, chemical durability, adhesion and optical quality [16]. The surface is a site for a variety of chemical and physical processes important in processing and properties of glasses. It acts as an interface between the outer atmosphere and the bulk of the glass network. The atoms at the surface act as frontiers between the two worlds that need to be crossed to access new possibilities, the development of physical and chemical rules that are amplified at the border atoms. The surface consists of “dangling” bonds in the form of Si- and Si-O- that are unsatisfied. The structure of the glass surface depends on the reactions of these dangling bonds with the surrounding environment. The ubiquitous presence of these active sites forges a basis to regard the surface as a living entity. The following sub section presents the role of these dangling bonds to form different types of silanol groups that critically define the surface structure.

1.2.1 Surface silanol groups

The reactions of the dangling bonds with the ambient atmosphere form silanol groups (SiOH). The near-surface region is essentially composed of hydroxyl groups. The inevitable interaction of the dangling bonds with atmospheric moisture leads to the formation of different kinds of silanol groups. They can exist in the form of isolated

silanols, geminal silanols, vicinal silanols and non-interacting silanols, as illustrated in Figure 1.2 [17].

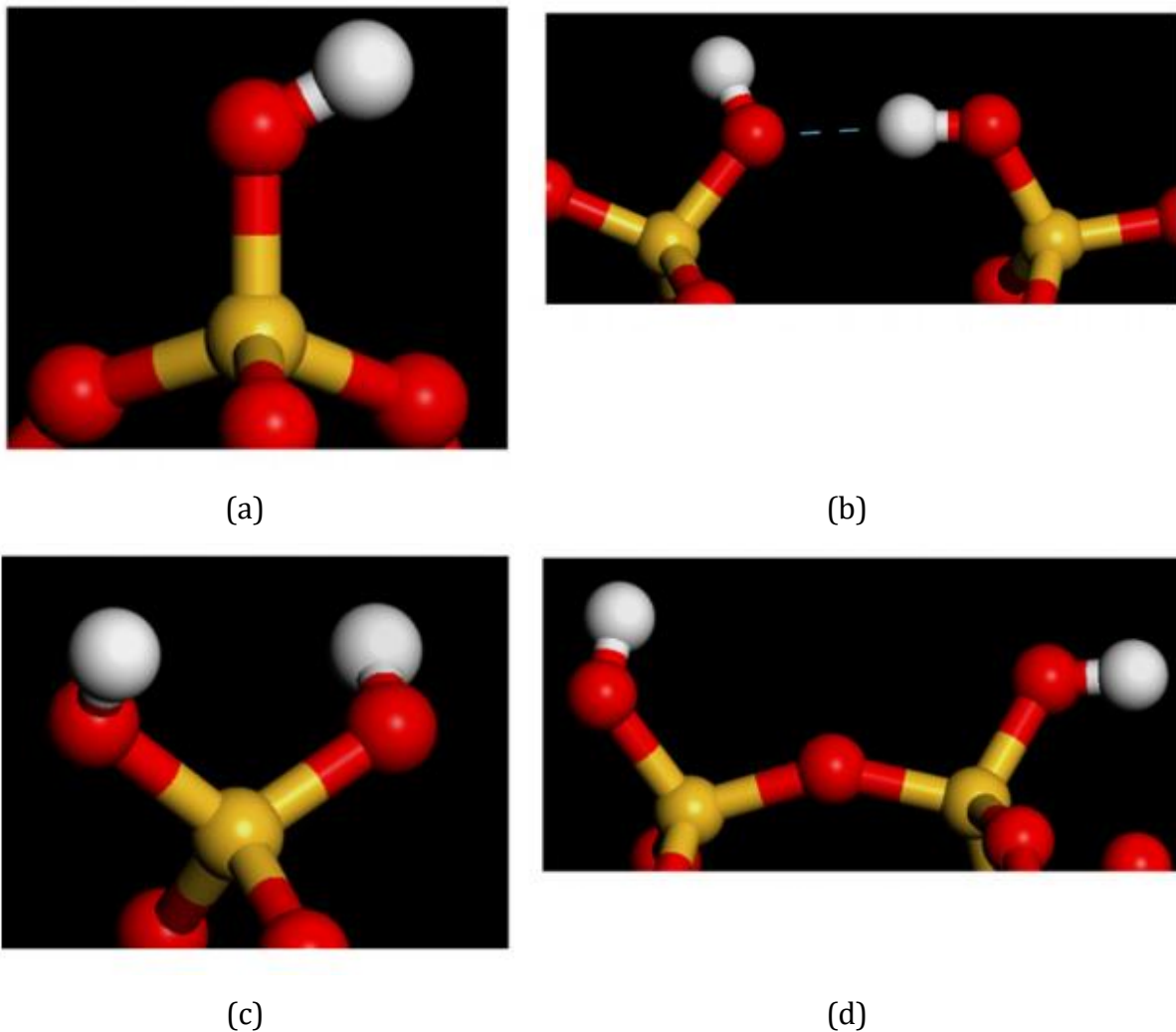


Figure 1.2. Schematic representation of (a) isolated silanol (b) vicinal silanol (c) geminal silanol (d) non-interacting silanol. Si (yellow), O (red), H (gray) [17]. Reproduced with permission from John Wiley and Sons.

Water and hydroxyl species are often retained in commercial glass from the water vapor in the melting atmosphere or the raw materials [18]. Water can exist in glass either in different forms of silanol groups (see Figure 2) or as interstitial molecular water. When the total water concentration is less than 1000-3000 ppm in the bulk, the majority of it exists as SiOH. Interstitial molecular water is dominant at higher concentration [19]. These hydrous species influence the glass structure and the properties of the glass. For instance, water reactions during the melting of silicate glasses weaken the Si-O-Si network by depolymerization and generation of terminal OH groups. Molecular water in silica glass

can affect structural relaxation [20]. Surface structural relaxation takes place much more rapidly than bulk structural relaxation, promoted by moisture in the atmosphere. It is also known that water adsorption and surface hydroxylation affect the mechanical strength [21, 22, 23, 24] and residual surface compressive stress in chemically strengthened glass [25]. The incorporation of these water species can enhance corrosion and dissolution, which forms the basis of discussion in the next section on glass surface corrosion.

The application of infrared (IR) spectroscopy to detect different water species like H, OH and H₂O in glasses has been extensively reported [18, 22, 26, 27, 28, 29, 30, 31, 32, 33]. The OH stretching vibration in the mid-IR region can be used to detect the presence of different forms of silanol groups and water molecules. Although the presence of bulk water can be evaluated by transmission IR, it lacks surface sensitivity to reveal the speciation of water in the near-surface region. Attenuated total internal reflection (ATR) mode of infrared spectroscopy (IR) enables surface-sensitive analysis in the outermost region of the surface [18, 29, 30, 31, 33]. It uses a crystal with a high refractive index (typically diamond) through which light is passed. When the crystal is in direct contact with the glass sample of lower refractive index, the light is totally reflected at the interface. The evanescent wave of the light penetrates into the glass sample in contact with the crystal surface. The absorption of this evanescent wave by the sample attenuates the total reflection of the light at the interface, which is recorded as a function of the wavelength of the reflected light. The evanescent wave decays exponentially with the distance from the surface within the specimen. Its penetration depth, d_p , is usually expressed as the distance at which the electric field intensity in the sample falls to 37% (e^{-1}) of the surface value. It is calculated by the following equation:

$$d_p = \lambda / \{ 2\pi n_1 \left[\sin^2 \theta - \left(\frac{n_2}{n_1} \right)^2 \right]^{\frac{1}{2}} \} \quad (1.1)$$

Where, λ = wavelength of the IR beam, θ = incident angle of the IR beam, n_1 = refractive index of the internal reflection crystal, n_2 = refractive index of the sample. The refractive index changes only slightly in the wavenumber range between 1600 and 4000 cm^{-1} for SLS glasses [34]. The information depth of ATR-IR is about 0.5-0.7 μm for the mid-IR stretching vibration region of hydroxyl groups and $\sim 1.1 \mu\text{m}$ for the bending vibration region of molecular water [18, 30, 33]. The penetration depth (d_p) of the squared evanescent field [35] is nearly 118 nm at 3400 cm^{-1} with a probing depth ($3d_p$) of

approximately 354 nm. The molecular water peak is observed around 1620 cm^{-1} . The OH stretching region of the mid-IR spectra confined in the range of 2500 to 4000 cm^{-1} provides surface-sensitive information about both silanol groups and molecular water. The OH stretch band is very sensitive to the strength of hydrogen bonding interactions. The bond lengths of the hydrogen bonds ($\text{H}\cdots\text{O}$) that govern the strength of these interactions are a function of the OH stretching frequency as shown in Figure 1.3 [31, 36, 37].

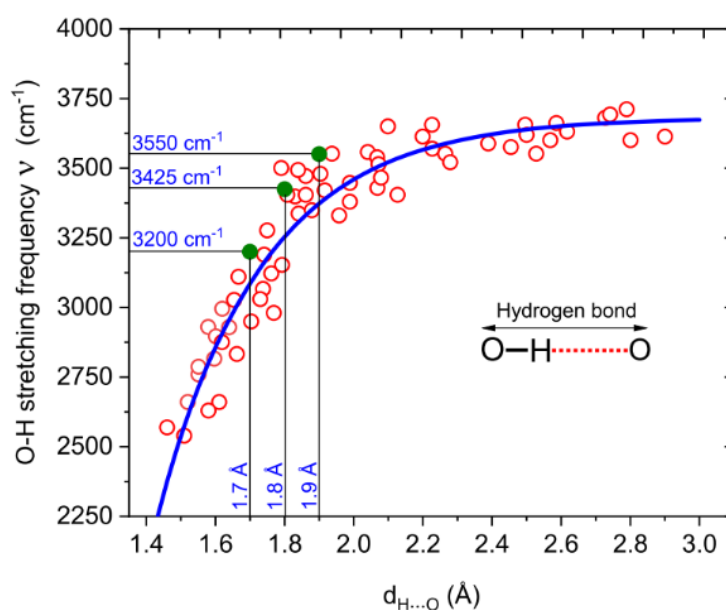


Figure 1.3. Relationship between O-H stretching frequency and $\text{H}\cdots\text{O}$ distance in solid materials [31, 36]. Reproduced with permission from Springer Nature.

Water adsorption, dissolution of glass network and ion-exchange occur at the surface and interface, which necessitates a thorough knowledge of the hydrogen bonding interactions of the hydrous species at the internal or external interfaces. Vibrational sum frequency generation (SFG) spectroscopy is a powerful technique for studying surface and interfacial species [22, 30, 31, 38, 39]. It is a second-order non-linear optical technique unlike ATR-IR spectroscopy. ATR-IR is suited to be used for the detection of hydrous species at the near-surface region of glass, while SFG is suitable for the investigation of hydrous species at the surface and interface. These hydrous species are critical to the structure of the near-surface region of the glass as discussed below.

1.2.2 Near-surface structure

The structure of the near-surface region can considerably differ from the bulk, owing to the inhomogeneous surroundings of the surface atoms and the tendency to lower the surface energy [40]. If the glass surface is melt-formed in a gaseous medium, the smooth surface of a liquid is frozen in. Formerly, it was believed that the surface had a lower refractive index corresponding to a lower density, because the surface was cooled faster than the bulk. It was later reported and complemented that the glass surface consisted of a layer of 4 nm with higher refractive index. This layer is often referred to as the “glass skin”. It evidently influences the mechanical, chemical and physical properties of glass, especially the quality of an adjacent coating. The glass skin protects the glass against the attack of surrounding media. Many evidences of glass surfaces confirmed that the skin had a higher density. The glass network may be assumed to be analogous to a fishnet. On the margin, the net mesh cannot be completely extended due to lack of three-dimensional drawing forces. Such configuration deformation results in smaller net voids. In addition, it has been reported that the glass surface is mainly formed by three or four membered silica tetrahedral rings [41], whilst the volume (bulk) is formed by six-, seven- and eight-membered rings [42]. Such a disparity in the network structure results in smaller voids in the surface layer than the bulk. A network unit of six-membered ring with the ring opening of 0.24 nm, is comparable to the diameter of a water molecule (0.28 nm) [43]. Figure 1.4 represents a schematic diagram of the glass network structure of the near-surface region.

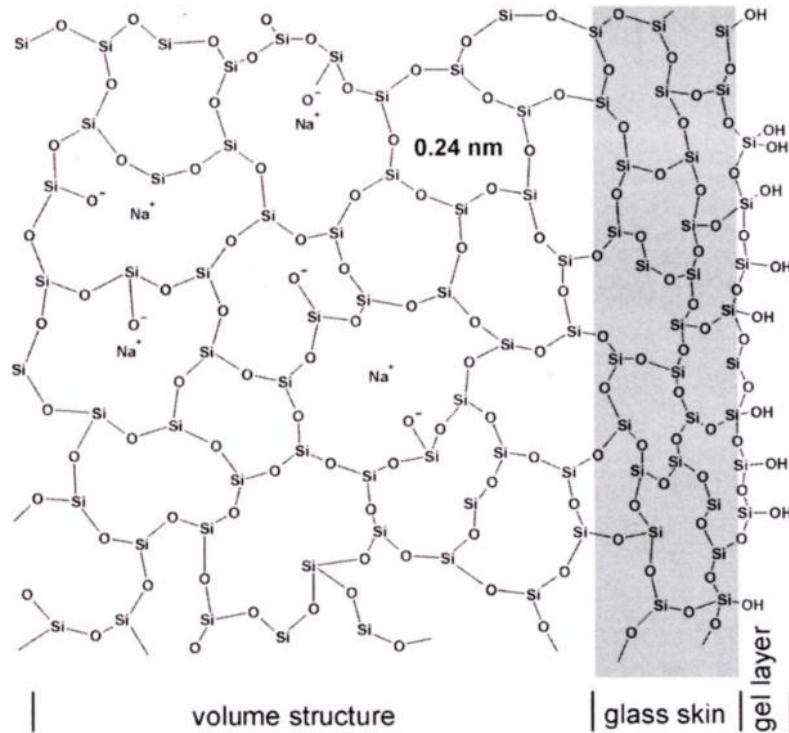


Figure 1.4. Schematic representation of the glass network structure near a surface [40].
 Reproduced with permission from the Journal of Glass Science and Technology.

The gel layer (5 to 10 nm) consists of surface silanol groups and water molecules connected by hydrogen bonds to the silanol groups. This layer can be formed in air within several minutes [44]. The skin is considered to be silica-rich due to the absence of modifier cations. The structure of the surface and the near-surface region can be effectively studied by X-ray photoelectron spectroscopy, as discussed in the subsequent sub-section.

1.2.2.1 Investigation of the near-surface structure by XPS

X-ray photoelectron spectroscopy (XPS), also known as electron spectroscopy for chemical analysis (ESCA) — is a powerful tool to characterize the chemical speciation of the top surface and the near-surface region of SLS glass [45]. It employs a soft X-ray beam to induce emission of electrons from the irradiated surface, with a sampling depth that is usually around 5-10 nm. In addition to the possibility to detect and distinguish different elements (from Li to U), the advantage of XPS is its ability to provide quantitative information on the chemical state, including the local chemical bonding environments.

This section describes the basic working principle of XPS before elaborating its application to glass surfaces.

1.2.2.1.1 Working principle of X-ray photoelectron spectroscopy

The principle of XPS is based on the well-known photoelectric effect explained by Albert Einstein in 1905 [46]. Photoelectron production in its simplest form, describes a single step process in which, an electron initially bound to an atom/ion is ejected by a photon. Since photons are massless (zero rest mass), chargeless package of energy, these are annihilated during photon-electron interaction with complete transfer of energy [47]. If this energy is sufficient, it will result in the emission of the electron from the atom/ion as well as the solid. The kinetic energy (KE) that remains on the emitted electron is the quantity measured. It is of a discrete nature and is a function of the electron binding energy (BE), which, in turn, is element and environment specific.

When a glass sample is irradiated by a beam of soft X-rays of energy $h\nu$ (few keV), electrons in orbitals with binding energies less than $h\nu$ can be ejected from the atoms. They are subsequently detected in a spectrometer and analyzed in terms of their KEs. Although KE is the quantity recorded in XPS, it is the derived BE that is used to construct the energy spectrum. The relationship among KE, BE and the initiating photon energy, $h\nu$ can be expressed by the principle of conservation of energy:

$$BE = h\nu - KE - \Phi_{spec} \quad (1.2)$$

where, Φ_{spec} is the work function of the spectrometer in ohmic contact with the solid sample (typically 3-5 eV). It represents the minimum energy necessary to remove an electron from the instrument on the assumption that a conductive sample in physical contact with the instrument is analyzed. Mg K α (1253.6 eV) or Al K α (1486.6 eV) X-ray anode sources are commonly used for XPS in laboratory instruments. The energy level diagram representative of the above equation is shown in Figure 1.5.

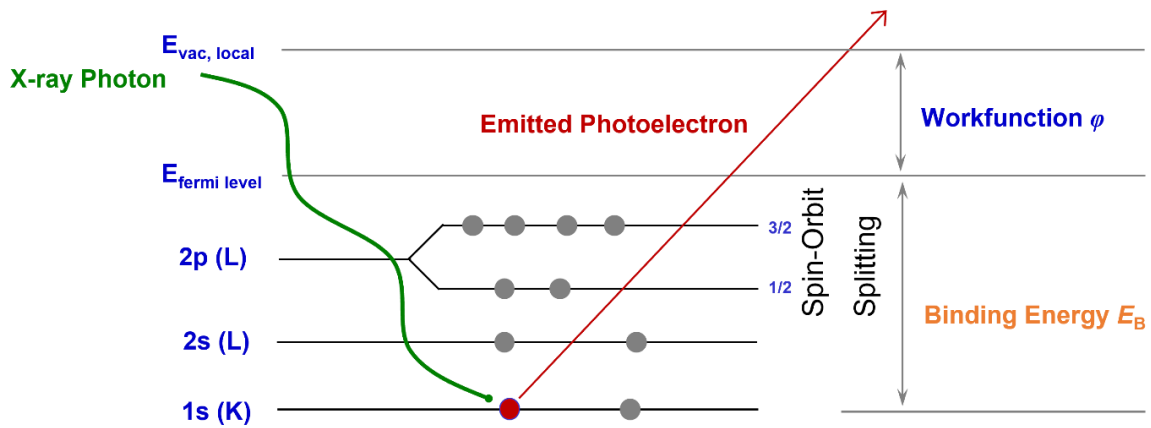
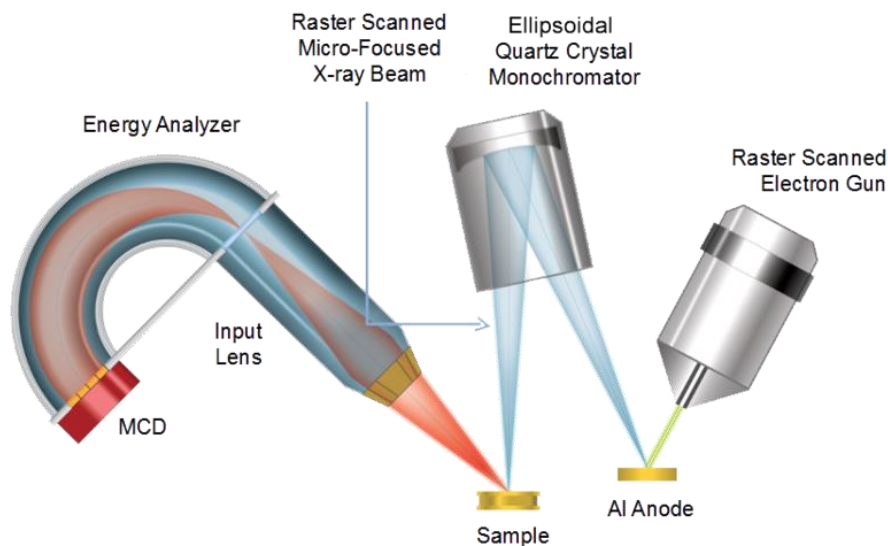


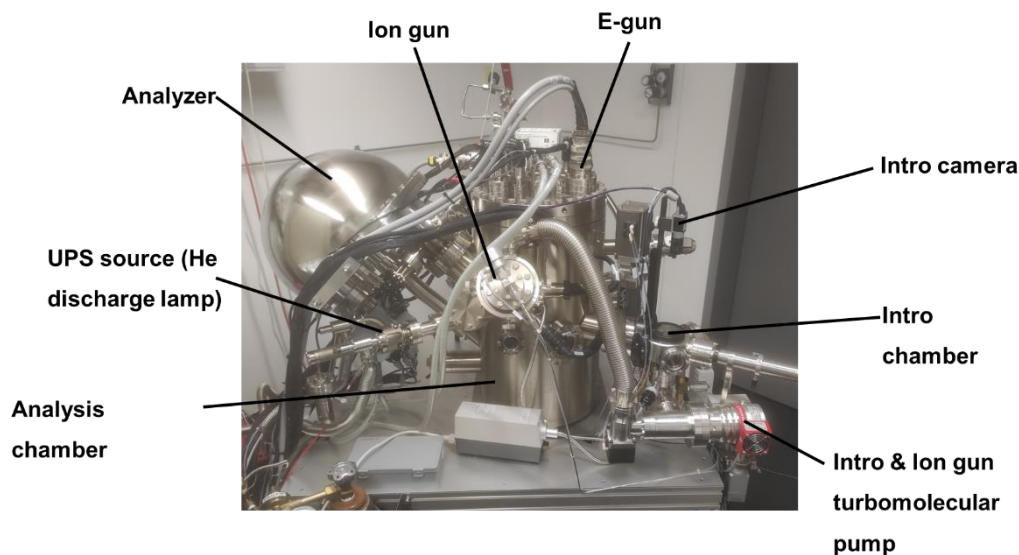
Figure 1.5. Schematic illustration of the energy level diagram of XPS. Adapted from [48]

A typical plot of XPS spectrum represents the number of emitted electrons as a function of their binding energy. The information obtained from XPS measurements relies on the observation of photoelectrons emitted from core levels of the atoms in the sample surface. The ionizing radiation can access at least one core level for all elements, with binding energies in the range of 10-1400 eV. The binding energy of a core electronic level is determined by the electrostatic interaction between the electron and the nucleus. The binding energies of the elements are well-known and tabulated with minimal overlaps [49].

The basic instrumental setup of XPS is shown in Figure 6. Al $K\alpha$ X-rays are produced by irradiating an Al anode with a focused electron beam (1486.7 eV). A quartz single crystal is used to produce monochromatic Al $K\alpha$ X-rays via defined lattice spacing and Bragg's diffraction criterion. The X-ray beam interacts with the glass surface and generates photoelectrons that are collected, focused and fed into a hemispherical electrostatic energy analyzer. The electron multipliers in the detector sample the counts based on binding energy of the emitted photoelectrons. The described process is schematically illustrated in Figure 6 (a).



(a)



(b)

Figure 1.6. (a) Basic instrumental setup of XPS [50], courtesy of Physical Electronics
 (b) PHI 5000 Versa Probe III

The environment within the XPS instrument should be such that [47]:

- (a) The photoelectron and Auger electron emissions are not affected by any external electrostatic or magnetic fields
- (b) The photoelectron and Auger electron emissions are able to traverse the region between the sample and the detector (around 1 m in distance)

- (c) The sample from which the emission arises must not be modified in any form or fashion during the course of analysis.

All external magnetic or electric fields must be minimized or accounted for. They would otherwise affect the kinetic energy and hence the binding energy of the emitted electrons. External fields also include those arising from the earth's rotation, i.e. the earth's magnetic field. Although this remains constant at a place, it does vary with location around the globe. XPS instruments also use mu-metal (~76% Ni, ~17% Fe, ~5% Cu, ~2% Cr) either in the construction of the analysis chamber, energy filter housing and detector housing or in the lining of these chambers/housings. This material acts as an effective shield against any extraneous magnetic or electrostatic fields. If used as a lining, 316L grade stainless steel (~68% Fe, ~17% Cr, ~12% Ni and 3% Mo) is then used in the chamber/housings. These materials are also used as they provide the conditions necessary for the production of ultrahigh vacuum (UHV) conditions. UHV conditions (pressure on the order of 10^{-9} mbar) are necessary in XPS to satisfy the criteria listed above. Under atmospheric conditions, there exists on the order of 2×10^{19} molecules/cm³. Such a high density of foreign molecules would otherwise prohibit the transmission of electrons from the sample surface to the detector. This necessitates UHV conditions in the chamber, which in turn, demands the solid sample to be stable under UHV.

The surface sensitivity of XPS is characterized by its ability to identify and quantify the elemental composition and speciation present over the outer 10 nm or less of any solid surface. It is based on the assumption that the element of interest exists at >0.05 atomic %. Surface specificity arises from the limited flight path an electron has within a solid before it loses a fraction of its energy by inelastic collisions against other electrons in the material that involve loss of energy. Although the X-rays that irradiate the sample surface can penetrate micrometers below the surface, photoelectrons that only originate from the outermost surface layers (usually less than 10 nm) can reach the solid surface without changing their kinetic energy for inelastic scattering. Only the electrons leaving the solid surface without any inelastic scattering contribute to the characteristic photoelectron bands. Consequently, the surface sensitivity of XPS is determined by the depth from which an electron can be generated to escape without inelastic scattering. The primary factors controlling the volume analyzed are:

- (a) The distance a photoelectron can travel within a solid before losing energy by inelastic collisions, described by the term, inelastic mean free path (λ_{IMFP}). It is defined by the average distance traveled by an electron of a specific energy within a particular single-layered homogenous amorphous solid between two successive inelastic scattering events.
- (b) The angle relative to the surface from which the photoelectrons are collected. This angle is often referred to as the take-off angle (θ).

The population of electrons of a specific energy emanating from a solid decrease exponentially with their depth of origin. The sampling depth equates to the depth from which 95.7% of all photoelectrons emanate. It is equivalent to $3 \cdot \lambda_{IMFP} \cdot \cos\theta$. The escape depth is defined by the normal to the surface from which 61.7% of the original photoelectron population originates. It is defined as $\lambda_{IMFP} \cdot \cos\theta$. 61.7% and 95.7% translate to a drop in intensity of e^{-1} and e^{-3} , respectively.

One of the strengths of XPS lies in its ability to quantify the recorded signals with relative ease without the need of any reference material. Quantification in XPS assumes homogenous amorphous-like mixtures over the volume analyzed with no diffraction effects present. The intensity of a particular photoelectron peak can simplistically be expressed in the absence of elastic scattering events as [47]:

$$I = J \cdot c_a \cdot \alpha_{pc} \cdot K_f \cdot \lambda_{IMFP} \quad (1.3)$$

Where, J represents the X-ray flux striking the analyzed area; c_a is the concentration of the photoelectron emitting atom/ion within the sampled volume (a is the element of interest); α_{pc} is the photoelectron cross-section; K_f encapsulates all instrument factors such as the transmission function. The terms α_{pc} , K_f and λ_{IMFP} are encompassed into what is referred to as the sensitivity factor F. The factor J is omitted since it remains constant during a particular analysis. The sensitivity factor is specific to the instrument used, as well as the element and level the photoelectron emanated from. The concentration of the element is derived from the sample of interest by dividing the intensity of the pertinent level by its sensitivity factor F, according to the following equation [47]:

$$c_a = (I_a/F_a) / ((I_a/F_a) + ((I_b/F_b) + \dots)) \cdot 100 \quad (1.4)$$

Where, the subscripts, a, b and so on, represent different elements.

1.2.2.1.2 Application of XPS to glass surface

There has been limited usage of XPS to study the structure of silicate glasses, until recently. NMR and Raman spectra have been more widely used, as discussed in section 1.1. This is mainly because XPS is a surface-sensitive technique rather than a technique to obtain bulk structural properties. Moreover, the spectral resolution used to be relatively low to be interpreted properly.

The bonding states of oxygen atoms are commonly determined by studying the O1s spectral line in the binding energy range of around 528-534 eV. The highest energy peak around 536 eV is a Na KLL Auger line. The O1s spectral line contains signals from overlapping peaks corresponding to BOs, NBOs and hydrous species in the form of SiOH/H₂O [7, 17]. The hydrous species are cited as a combination of surface hydroxyls and water as a distinction cannot be made without removal of physisorbed water at elevated temperatures [17]. Hereafter, the term “hydrous species” will be used in the text to refer to the combination of silanol groups and molecular water — SiOH/H₂O. Gaussian-Lorentzian curve-fitting of the O1s spectral line is a popular method of distinguishing the overlapping contributions of the individual species. The relative abundance of the oxygen speciations can be calculated by the normalized integrated peak areas to obtain their concentrations, expressed in atomic percentages. This approach has been adopted in this work with an elaborate discussion in conjunction with presenting the experimental results in Chapter 3, Section 3.2.2.

The contribution of the individual network modifier cations to the total concentration of NBOs may also be stoichiometrically calculated, along with the concentrations of BOs and SiOH/H₂O, by the following system of equations, considering charge neutrality and mass balance [17]:

$$\begin{aligned} NBO &= 2[Ca] + 2[Mg] + [Na] - [Al] \\ [OH + H_2O] &= |(-2) \cdot [O_{Total}] + (1 \cdot [Na] + 2 \cdot [Ca] + 2 \cdot [Mg] + 3 \cdot [Al] + 4 \cdot [Si])| \\ BO &= [O_{Total}] - [NBO] - [OH + H_2O] \end{aligned} \quad (1.5)$$

Apart from O1s spectral line, the Na1s and Si2p spectral lines are also taken into consideration for investigation of the structure of SLS glasses. For instance, the characteristic shift of the peak maxima of Si 2p_{3/2} to lower binding energy is indicative of

increased Na₂O content. Similarly, the Na1s peak maxima are affected by the glass composition.

The XPS probing depth is confined to less than 10 nm below the surface, defined by the inelastic mean free path of the electrons, as discussed in section 1.2.2.1.1. For instance, 95.7% ($3\lambda_{\text{IMFP}}$) of electrons with K.E. values less than 1 keV would travel less than ~ 6 nm in Si with 61.7% interacting within one-third of this distance. Information on the depth distribution of elements within this region of the solid can be attained by utilizing angle-resolved X-ray photoelectron spectroscopy (AR-XPS). This possibility stems from the fact that the sampling depth is a function of both Θ and λ_{IMFP} . In many instances, however, it is desirable to not only obtain information on the composition and speciation of the elements present at the outer surface of the glass, but also to understand how these may vary as a function of depth from the glass surface. A common method of probing further into the glass network is associated with ion beam sputtering. It facilitates removal of surface atomic layers in a controlled manner as a result of the impact of energetic ions over the area of interest. This can pave the way to the third dimension by offering the possibility of accessing depths that are otherwise inaccessible to XPS, that is, layers at depths well over the maximum sampling depth. If sputtering is carried out in an interleaved manner with collection of photoelectron spectra, depth profiles of the elements of interest can be obtained. The most commonly used ions for sputtering in XPS are Ar⁺ with typical energies in the range of 0.5 to 5 keV. There is an increased interest in the use of clustered ions such as C₆₀⁺ that induce far less damage during depth profiling of organic films. Previous reports illustrated certain drawbacks associated with Ar⁺ sputtering on the structural damage of silicate glasses with respect to the migration of alkali ions [51, 52]. The usage of C₆₀⁺ has been recently shown to have a reduced extent of structural damage [53].

For energetic monoatomic ion impact (e.g., Ar⁺), sputtering primarily occurs via the formation of a linear collision cascade. It is an elastic process with momentum being transferred to atoms/ions contained within the sample being analyzed. Since these ions can transfer this energy well below the sputtering front, significant damage of the sample can occur. During a linear collision cascade, a significant amount of kinetic energy is dissipated via elastic and inelastic processes. Only a small fraction of this energy is actually removed in the form of sputtered atoms. The remainder induces a myriad of

processes to modify both the composition (in the form of diffusion, segregation, implantation) and the electronic structure of the solid.

In case of cluster ions (C_{60}^+ , Ar_n^+ , where n is several thousands), sputtering is believed to occur primarily through low-energy inelastic processes. This may be realized by the fact that the energy of a 10-keV C_{60}^+ ion will be split among the 60 atoms yielding ~ 167 eV per atom. This reduced energy also results in significantly less sample damage. However, Ar^+ sputtering remains to be a widely used technique to probe the depth of the glass network. It is to be noted that if the region of interest is less than the sampling depth, angle-resolved measurements is more effective as it prevents the sample damage (a side-effect of sputtering).

1.2.3 Surface flaws

The tensile strength of most solids falls short of the theoretical value by a large factor [54]. In the case of brittle solids, particularly glasses, the discrepancy was attributed to stress concentration at minute flaws by Griffith in 1920 [55]. The surface flaws act as stress concentrators when subjected to externally applied stress to fail at stresses several orders of magnitude below the theoretical strength of glass. The failure strength decreases with the increase in flaw size [56]. Figure 1.7 illustrates the strength of glass products as a function of flaw size.

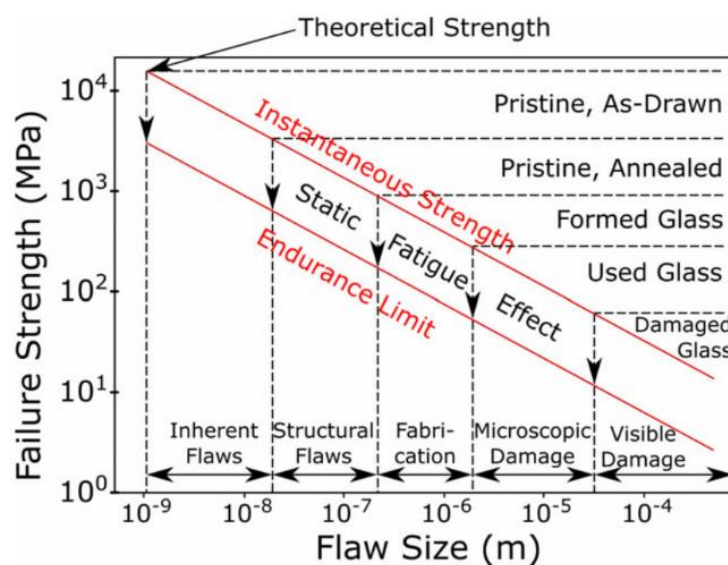


Figure 1.7. Failure strengths of glass products as a function of flaw size [56]. Reproduced with permission from John Wiley and Sons.

Flaws in glass are created as defects during glass melting (such as striations, stones, chords), glass forming (such as sharp reentrant angles between adjoining surfaces, mold crevices and insufficient fluidity), and subsequent handling by the glass makers as well as the consumers. One of the practical examples is the formation of surface scratches by abrasion. The size and severity of flaws are probabilistic. A typical strength tests shows a large distribution of strengths. The standard deviation is often exceeded by more than 25% of the mean value. On assuming the “weakest link” hypothesis for a fracture to occur, it may be shown that glass strength can be described by a Weibull distribution [56]:

$$F = 1 - e^{-\left(\frac{\sigma}{\sigma_0}\right)^m} \quad (1.6)$$

where, F is the cumulative failure probability up to an applied stress σ , σ_0 is a normalizing stress and m is the Weibull modulus. Typical values of Weibull moduli in manufactured glass are around 5. Flaws of varying severity are generated on the glass surface during handling and storage. They create a large number of indents and impacts which have sufficiently strong localized stress field to nucleate more flaws and grow them, specifically where local yield strengths are exceeded. Unlike metals, network solids such as glass do not have dislocations whose motion can be organized to display ductility once the yield stress is exceeded to lead to brittle fracture. Although theoretical estimates of forcing 2 atoms apart are as high as ~35 GPa, the failure strength decreases progressively with the incorporation of surface flaws at different stages of glass production, as demonstrated above in Figure 1.7.

From one of the accepted viewpoints, failure originates from cracks with atomically sharp tips [57, 58]. The behavior of sharp cracks can be described in terms of a fracture mechanics formulation in which the crack length is the sole strength-controlling dimension. In another view, strength-controlling flaws are considered to be intrinsically “blunt”. The strength is then related to the radius of curvature of the tip as well as to the length of the crack [59, 60, 61]. Thus, flaw lengthening (sub-critical crack growth) and flaw sharpening (crack initiation from a notch-like defect) are two mechanisms of interpreting fatigue strengths. It is conceivable that these two steps could occur sequentially in any failure process. The slower step would control the kinetics in that case. The flaws develop easily on the glass surface because of the brittle nature of glass. The

index of brittleness was defined as $B = H/K_c$, where H is hardness and K_c is fracture toughness [62]. On a brief note, hardness represents resistance to deformation while the fracture toughness represents resistance to fracture, i.e., a glass with lower hardness and higher toughness would have lower brittleness. The following section is intended to shed light on the surface mechanical properties.

1.2.4 Surface mechanical properties

The fracture of glasses is determined by crack initiation and subsequent propagation [63, 64]. Once a crack initiates in the glass surface, stress concentration occurs at the crack tips, resulting in catastrophic fracture under an applied stress much lower than the theoretical strength. Thus, the evaluation of crack initiation and crack propagation is of considerable interest for glass scientists and glass engineers. Naturally occurring flaws typically range in the scale of micrometers, that are difficult to locate and observe during their evolution to full-scale fracture. Micro indentation techniques such as Vickers indentation are particularly useful in this context to generate flaws with complete control of shape, size and site. Such flaws strongly resemble those which develop from general surface handling, machining, and polishing. Crack initiation by Vickers indenter is a commonly used technique to determine crack resistance of glass surfaces [62, 63, 64, 65, 66, 67]. Vickers hardness is used to express the extent of plastic deformation of glass. Plastic deformation consists of two processes: densification and shear flow. Densification is the inelastic plastic deformation that is accompanied by a decrease in volume, while shear flow is the volume conservative flow that occurs without any decrease in volume. Densification leads to reduction in interstitial space of the three-dimensional network in the vicinity of the indenter. This enables the region beneath the indenter to deform more easily to fit the contour of the indenter. Thus, densification reduces the stress concentration beneath the indenter to increase the crack resistance. Indentation using a sharp indenter leads to high hydrostatic stresses beneath the contact zone. Indentation-induced densification of glass has been evidenced [68, 69, 70]. The densified volume can be relaxed by annealing around the glass transition temperature. Thus, measuring the volume of indentation impression before and after annealing allows for the discrimination of the densified volume from the total indentation volume. At low peak loads, radial cracks initiate on the unloading cycle and grow to full length on complete

unload [71]. The radial cracks are nucleated by flaws at the deformation zone boundary and driven by the residual stress field arising from the strain mismatch of the plastically deformed zone embedded in the surrounding elastically restraining matrix. With increase in peak load, median cracks initiate on the loading half of the cycle as full circles beneath the deformation zone and grow in size with continued loading. On unloading, the median cracks spread outwards along the surface to leave a half-penny geometry at complete unload. At high peak loads, lateral cracks nucleate beneath the deformation zone on the unloading half of the cycle and grow on unloading to reach full size on complete unload. Figure 1.8 illustrates the different types of indentation cracks discussed.

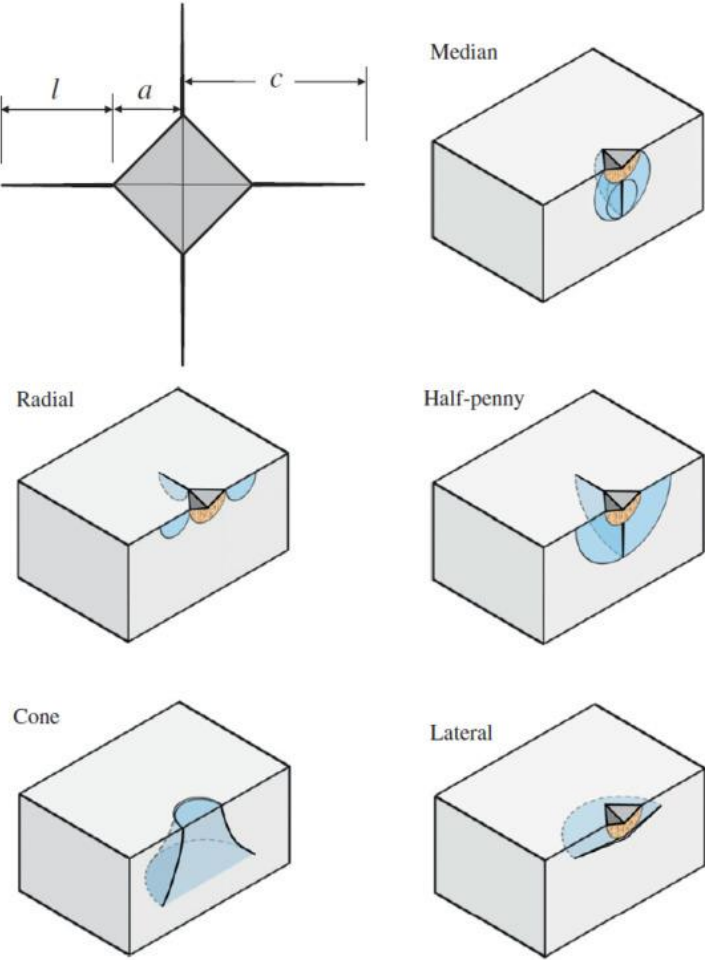


Figure 1.8. Resultant cracking systems of Vickers indentation [72]. Reproduced with permission from Elsevier.

Radial crack formation should be suppressed during and/or after unloading to increase the crack initiation load [72]. The driving force of radial crack formation is residual tensile stress surrounding the indentation. If the residual tension after indentation becomes smaller, crack formation resistance becomes higher. Crack resistance is defined as the load required for the radial cracks to initiate, indicating the difficulty of crack initiation. A crack initiation probability of 50% is considered to be the crack resistance. During loading, the glass is permanently displaced through densification and/or shearing, creating a hemispherical zone of compacted material surrounding the indentation cavity. The deformation mechanisms along with the stress fields during indentation are schematically represented in Figure 1.9.

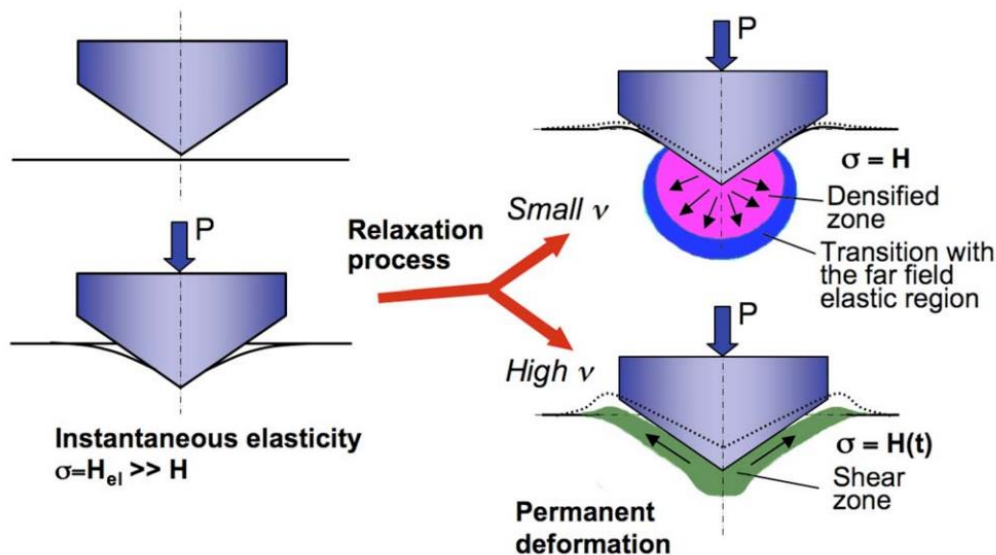


Figure 1.9. Schematic representation of the indentation deformation stages [73]. The dashed line indicates the indentation profile after unloading. Arrows indicate matter displacement. σ is the mean contact pressure. Reproduced with permission from AIP publishing.

Figure 1.9 shows the indenter pressed into the surface of the material at a given load (P). Once fully penetrated, the mean contact pressure (σ) corresponds to the instantaneous or elastic hardness (H_{el}), which is significantly larger than the hardness (H) after full recovery. The prevailing deformation mechanism is controlled by the Poisson's ratio (ν). The ratio of densification to the residual indentation volume decreases with increasing

Poisson's ratio of the glass [74]. The deformation mechanism is either densification in glasses with relatively low atomic packing density (e.g. anomalous glasses such as silica or Pyrex glass), or volume conservative shear flow in normal glasses with close-packed atomic network such as SLS or lead-silicate glasses, or a combination of both in general [74].

Vickers hardness (HV) is measured by pressing the indenter into the material under a defined test load [75]. The indenter is a square-based diamond pyramid with a face angle of 136°. After a certain dwell time, the load is removed. The Vickers hardness value is defined as the quotient of the applied load (F) and the surface area (A) of the residual indentation — the result of the permanent plastic material deformation component of the test. The indentation diagonal lengths (d) are measured on the specimen surface to determine the indentation area. Based on the Vickers indenter geometry, the Vickers hardness is given as [75]:

$$HV = \frac{0.102F}{A} = \frac{0.102F}{\frac{d^2}{2 \sin \frac{\alpha}{2}}} = 0.1891F/d^2 \quad (1.7)$$

The factor 0.102 has been inserted to equation 1.7 to produce the same hardness values after adopting Newtons instead of kilo pounds as the unit of the test load. This definition and calculation are based on the assumption that the permanent indentation is a true geometric image of the indenter after load removal. This assumption, however, is not justified for reasons concerning the non-uniform stress distribution at the point of indentation as discussed [75]. While the test load is applied, the indenter is under the same stress as the specimen and will, therefore, be subject to elastic deformation. However, the indenter is viewed as having ideal stiffness because the modulus of elasticity of diamond is very large. A Vickers indentation is never a negative imprint of the exact indenter geometry, regardless of material properties.

Universal hardness, HU, is based on indentation with a Vickers indenter. It is associated with the measurement of the indentation depth, or indenter displacement under test load. The designation of Universal Hardness implies the applicability of the method to all materials. Since the Vickers hardness or HV test is a different hardness test method, reference to the Vickers method should be avoided to prevent misunderstandings. The Universal Hardness is defined as the quotient of the test load (F) and the surface area (A) of the indentation under an applied test load. Based on the pyramid geometry, universal

hardness can be described as a function of applied load and the indentation depth under the applied load, with the assumption of an indenter of ideal stiffness [75].

$$HU = \frac{F}{A} = \frac{F}{4 * (\sin \alpha / 2) / (\cos^2 \alpha / 2) * h^2} = \frac{F}{(26.43 * h^2)} \quad (1.8)$$

The universal hardness is expressed in N/mm², that differentiates HU from HV. The values of universal hardness are generally higher than the classic Vickers hardness number by a factor of approximately ten [75]. As a result of the equilibrium between the applied test load and the resistance of the tested material to indenter penetration, the universal hardness is also physically more meaningful to be realistically used for evaluation of the surface hardness of glasses. The concept of universal hardness also fulfils the technical definition of hardness as the resistance of a material to the penetration by another object of harder material. In this research work, the approach of universal hardness, also known as Martens hardness, was adopted to evaluate the subsurface hardness at low loads analogous to nanoindentation, as discussed subsequently.

As the name implies, nanoindentation can use much smaller loads on the order of 10-100 mN to produce smaller indents with penetration depths in the range of 10-1000 nm, unlike typical hardness measurements [76, 77]. In fact, loads of only a nanonewton (nN) and displacements of 0.1 nm have been measured accurately [77, 78]. These attributes make nanoindentation an attractive choice for characterizing the mechanical properties of thin films and surfaces, such as the case depth of ion-exchanged glasses. Unlike traditional hardness measurements that involve indentation and imaging of the residual indent at a later time, nano- or ultralow load indentation is able to measure Young's modulus and hardness continuously. It measures the load (P) along with the corresponding displacement into the surface (h) during one complete cycle of loading and unloading, enabling real-time determination of F and A. The underlying equations that allow the determination of hardness from nanoindentation assume a mostly elastic contact between the indenter tip and the sample, resulting in sink-in only rather than pile-up of the material around the indent [78]. This is generally a valid assumption for the indentation of hard ceramics and glasses. A typical set of load-displacement data of instrumented indentation technique is presented in Figure 1.10 (a). The key quantities are the peak load, P_{max}, the displacement at peak load, h_{max}, and the initial unloading

contact stiffness, $S = dP/dh$, i.e., the slope of the initial portion of the unloading curve. The physical processes occurring during indentation are schematically illustrated in Figure 1.10 (b).

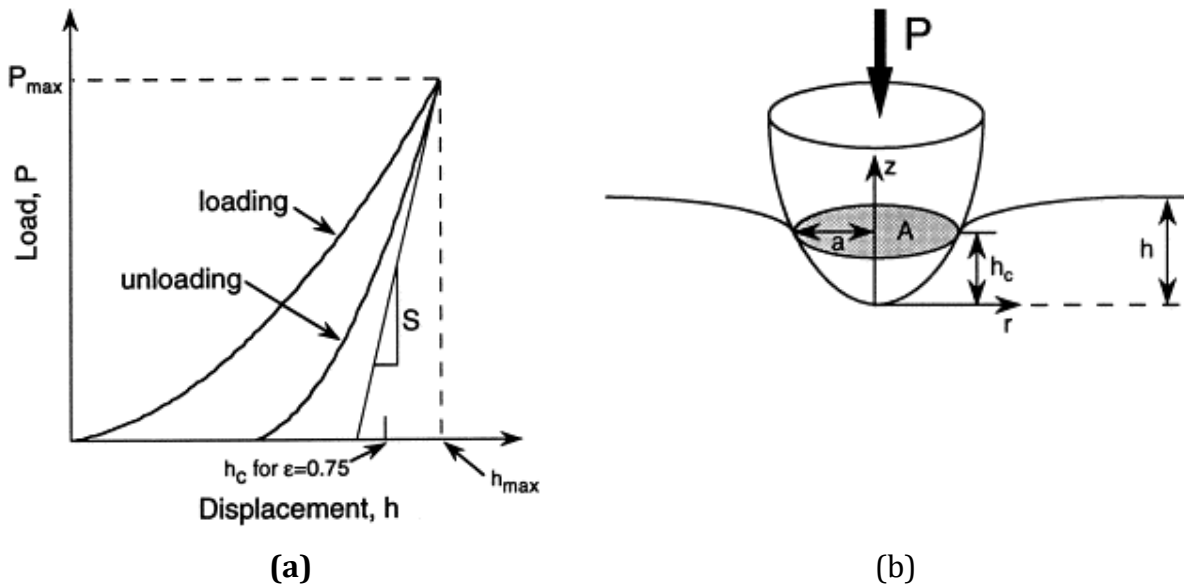


Figure 1.10. (a) Typical load-displacement curve illustrating the loading and unloading cycle during indentation (b) Physical processes involved in indentation [78]. Reproduced with permission from Elsevier.

As the indenter is driven into the material, both elastic and plastic deformation occurs, which results in the formation of a hardness impression conforming to the shape of the indenter to some contact depth, h_c . During indenter withdrawal, only the elastic portion of the displacement is recovered, which facilitates the use of elastic solutions in modeling the contact process. The Oliver-Pharr data analysis procedure [79] begins by fitting the unloading curve to the power-law relation:

$$P = B(h - h_f)^m \quad (1.9)$$

where, P is the indentation load, h is the displacement, B and m are empirically determined fitting parameters, and h_f is the final displacement after complete unloading (also determined by curve fitting). The unloading stiffness, S , is then established by differentiating the above equation at the maximum depth of penetration, $h = h_{\max}$, i.e.

$$S = \frac{dP}{dh}(\text{at } h = h_{max}) = mB(h_{max} - h_f)^{m-1} \quad (1.10)$$

The contact depth is also estimated from the load-displacement data using:

$$h_c = h_{max} - \varepsilon P_{max} S \quad (1.11)$$

Where, P_{max} is the peak indentation load and ε is a constant which depends on the indenter geometry [79]. Empirical studies have shown that $\varepsilon \approx 0.75$ for a Berkovich indenter. The hardness is given by equation 1.8.

At low indent loads, such as 0.5 N or below, the indentation size effect (ISE) has been found to affect hardness measurements in glasses. The ISE has been defined as an increase in hardness at decreasing indent penetration depths, typically below 1 μm [80]. The effect is thought to be caused by dislocation strengthening necessary to accommodate plastic deformation and/or friction between the indenter and the specimen [80, 81, 82]. Although there have been several reports on the ISE effect in bulk metallic glasses [82, 83, 84], it has been found to exist in silicate glasses and fused quartz in small magnitude [79, 85, 86, 87].

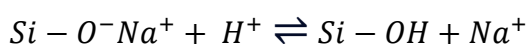
The surface structural chemistry of the silicate network is closely related to the surface mechanical properties. The relationship between surface structural and mechanical properties lacks a thorough understanding. This work aims to bridge the gap in knowledge in this field.

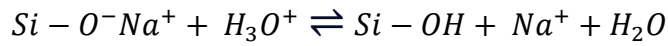
1.3 Glass surface corrosion

The presence of the network modifier cations in soda-lime-silica glasses increases the vulnerability of the surface to undergo significant alterations. The susceptibility of SLS glass surface to corrosion by water in liquid and vapor state combined with atmospheric alterations is the highlighting feature of discussion of this section.

1.3.1 Surface degradation by liquid water

Water reacts with the surfaces of SLS glasses to form a hydrated silica-rich layer [88, 89]. Ion-exchange between hydrogen or hydronium ions and alkali ions in the glass precedes the hydration reaction as follows [30, 43, 88, 89, 90]:





The concentration profiles resulting from this exchange and subsequent interdiffusion process have been characterized and reported [88, 89]. The reaction of water with alkali silicate glasses may be divided into two stages:

- (a) The first step is concerned with the amount of sodium and silica dissolved being proportional to the square root of time.
- (b) In the second stage, the amount dissolved is proportional to time.

These trends suggest the dissolution process to be initially controlled by diffusion, followed by a surface reaction. A transport process should prevail for a two-step process. A model of the hydrated layers on the surface of alkali silicate glasses is presented in Figure 1.11.

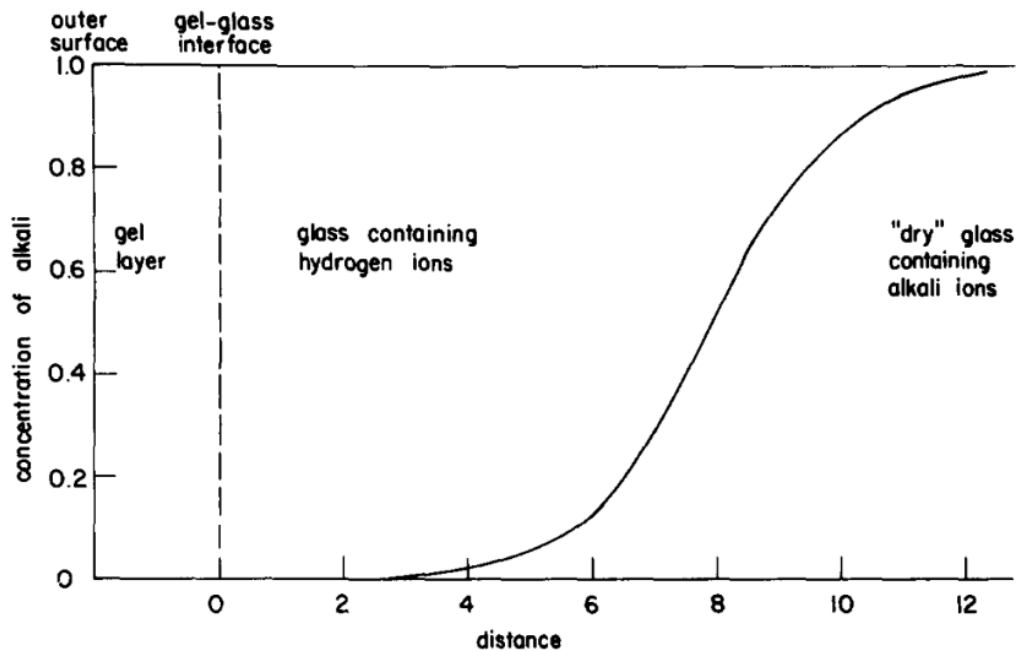


Figure 1.11. Model of the hydrated layers on the surface of alkali silicate glasses [88]. Reproduced with permission from Elsevier.

The central assumption of the Doremus model of interdiffusing ions [89] lies in the fact that in an SLS glass, the hydration consists of substitution and interdiffusion of hydrogen (H^+) or hydronium (H_3O^+) ions with the Na^+ ions in the glass. The physical basis of this model is that the Na^+ ions are the only mobile charge carriers in such a glass. The Na^+ ions

tend to diffuse out of the glass because of their mobility and the large concentration gradient at the glass surface. However, they cannot leave the glass because their negative anions are immobile. After a small diffusion of the Na⁺ ions, an electric field is set up that stops further diffusion. However, if a second positive ion (e.g. H⁺ or H₃O⁺) is introduced at the surface, this ion can interdiffuse with the Na⁺ ions, resulting in the diffusion of Na⁺ out of the glass as it is replaced by H⁺ or H₃O⁺. The transformation of the initial glass network to looser gel-like structure results from the reaction of water to break the Si-O-Si bridging oxygen network into silanol groups. The neutral water molecules could then penetrate the partly hydrated layer and react with Si-O bonds for further hydration of the glass network followed by dissolution.

While these reactions are slow at ambient conditions, they can be significantly accelerated at temperatures over 100 °C [91, 92, 93, 94]. First, the diffusion of water penetrating into the glass network is accelerated at elevated temperatures [95]. Second, the reactivity of water molecules is also higher. For example, the ionization constant of water (K_w) at 150 °C is approximately 2 orders of magnitude higher than the value at room temperature [96, 97].

1.3.2 Surface degradation by atmospheric influence

The alteration of SLS glass surface by atmospheric humidity has been a subject of considerable study in the past [98, 99, 100]. The atmospheric alteration of a commercial soda-lime-silica glass is characterized by the appearance of a slight veil on the surface composed of sodium carbonate and calcium carbonate crystals [101, 102, 103]. These crystals can develop with time into sodium sulphate and calcium sulphate crystals in a polluted atmosphere containing SO₂. The solubility of these crystals in water makes it easy to remove them. This is considered as a reversible stage from optical and mechanical viewpoint — the glass is very similar to the original glass after cleaning. In case of further alteration, some pits below the crystals may develop that can be accountable for deterioration in the mechanical properties of the glass.

The relative humidity determines the number of layers of water molecules that build on the surface. Three to four layers are reached at 60% relative humidity, that increases exponentially when approaching 100% RH. The signs of glass hydration, marked by the

presence of a hydrated layer of a few micrometers, are observed beyond relative humidity of 50%. The rate of alteration is defined as the growth of the hydrated layer. In atmospheric conditions, the hydration rate generally increases with relative humidity, but it stays slower than the dissolution rate in hydrothermal or liquid water conditions in the initial dissolution regime. The glass composition has a critical influence in determining the rate-controlling process in the first few months of alteration, during which a hydrated layer forms. The composition also controls the properties of the hydrated layer, leading to different hydration kinetics in glasses of different compositions. The influence of the weathering mechanism by atmospheric influence on the glass surface is schematically represented in Figure 1.12 to illustrate the structural modifications in an alkali silicate glass.

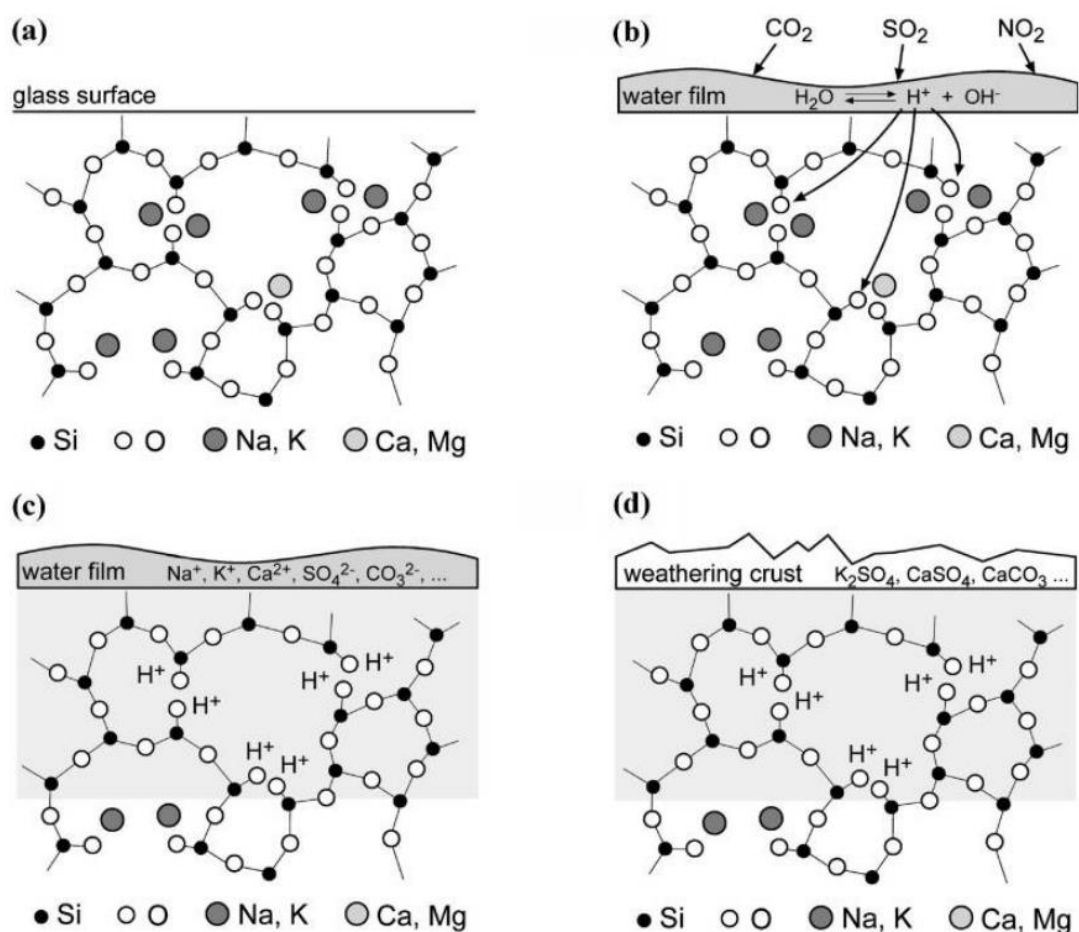


Figure 1.12. Glass weathering process starting with (a) clean surface (b) formation of a water film (c) a leached layer containing hydrogen (d) crystalline weathering products on the glass surface [104]. Reproduced with permission from ACS Publications.

The atmospheric alteration of glass is strongly influenced by the glass surface composition that may be different from the bulk composition due to process parameters [105, 106]. For instance, the tin-side of float glass that is enriched in tin, has a much better chemical durability than the air-side [107]. Similarly, the presence of SO₂ in the annealing lehr causes surface dealcalization, which improves the durability of the glass [108]. This treatment is industrially exploited in the case of glass vials. In addition, the surface composition and structure may be modified by specific protective treatments such as those used in dishwashers with zinc and bismuth, or with polyethyleneimine [109, 110].

The mechanochemical wear in soda-lime-silica glasses shows a unique dependence on humidity [22, 24]. It shows a decrease in wear with increase in humidity unlike other glass surfaces that show an increasing wear with increasing humidity of the test conditions. In case of fused quartz glass, the wear volume gradually increases with relative humidity, which can be explained by the classical stress corrosion theory of enhanced crack growth by the dissociation of Si-O-Si network by water [90, 91, 92, 111]. The phenomenon of stress corrosion accelerates the hydrolysis reactions of glass on application of mechanical stress. However, the wear behavior in SLS glass differs by the increased wear resistance observed at high relative humidity. This could be attributed to the growth of hydronium ion concentration in the Na-leached region of the SLS glass surface. When the Na⁺ ions with lower ionic radii of 0.1 nm are replaced by larger hydronium ions of ionic radii 0.14 nm, compressive stress builds up at the glass surface, which could improve the mechanical properties of the surface. As the humidity decreases, the concentration of hydronium ions in the surface decreases to make it more vulnerable to wear upon tribological shear.

1.3.3 Surface degradation under hydrothermal condition

Vapor-phase hydrothermal treatment of silicate glasses has received considerable attention [20, 30, 112, 113, 114, 115]. Hydrothermal reactions are typically carried out in a sealed reactor at temperatures over 100 °C. During the hydrothermal treatment at 200 °C and 250 °C, water can diffuse into alkali-free glasses and react forming Si-OH groups [113, 114]. However, such hydrothermal treatments in liquid water have been reported to strengthen vitreous silica glass [113, 115]. In case of SLS glass, hydrothermal treatment in liquid water was reported to create a porous surface layer [116].

One of the critical studies that further led to the advancement of understanding the influence of hydrothermal treatment of SLS glass on surface mechanical properties was reportedly focused around 150 °C [30]. The overall hardness decreased after the hydrothermal treatment. The silicate network was altered due to the reaction with water in the near-surface region associated with a modified, hydrated layer containing silanol groups. A longer treatment made the glass surface softer with a thicker modified layer. However, the resistance to crack formation increased that was attributed to the formation of silica-like surface layer to suppress crack initiation. This speculation was associated with the higher fracture toughness of silica glass than SLS glass.

The natural contribution of the inevitable surface flaws to brittle failure (Section 1.2.3) and the susceptibility of the glass surface to corrosion (Section 1.3) necessitate methods of strengthening glasses to partially overcome the massive gap between the real failure strength and the theoretical strength. The following section sheds light on some of the well-known methods of strengthening and hardening SLS glasses.

1.4 Strengthening and hardening of silicate glasses

There are several approaches of strengthening glasses, given the variety of factors that can affect the strength of the glasses. The following sub-section 1.4.1 is focused on summarizing the popular strengthening methods of silicate glasses.

1.4.1 Strengthening techniques

Some of the common methods of strengthening silicate glasses are listed below [56]:

- i. Fire-polishing during manufacturing
- ii. Etching
- iii. Polymeric coatings such as epoxides and silanes
- iv. Lamination
- v. Inclusion of a second phase
- vi. Thermal tempering
- vii. Overglazing with lower thermal expansion glass
- viii. Chemical strengthening by ion-exchange
- ix. Ion implantation

A brief description of each of the aforementioned techniques is presented in this text.

Fire-polishing of glass products during manufacturing takes little effort. It causes fluid glass to flow to close or round off the surface flaws to abate their severity [56].

Etching of glass is generally accomplished by immersing the glass in a warm 1-4% aqueous solution of ammonium bifluoride for a short time [56]. The solution removes layers of glass, thereby rounding off the flaws. Etching with acids e.g. wet SO₂ treatments — leaves a silica-rich surface layer. The treatment may also have a strengthening effect besides chemical durability.

Polymeric coatings such as epoxy and silane act to reduce the concentration of humidity at the tip of the flaws [56]. Consequently, it would impede stress-assisted subcritical crack growth velocity. A commercial example of coating the glass with epoxy is in optical fiber communication, where fibers are immediately coated with a UV-curable acrylate epoxy. After curing, the fibers can be readily rolled onto drums without the fear of breaking.

Laminated glass has attracted significant attention in the recent years with its use as a structural component for architectural applications. Flat glass plates are bonded to each other using commercially available sheets of tear-resistant and UV-resistant polymeric interlayer such as polyvinyl butyral (PVB) [56]. The interlayer can absorb some impact energy, thereby acting as a barrier to crack propagation to enhance the toughness. Laminated glasses are commonly used in automotive windshields, windows, display cases floors, staircases, walls and columns. Aircraft cockpit windshields are actually laminates of two or three plies of chemically strengthened glass bonded to each other using thick layers of PVB. Glasses for ballistic applications are invariably laminated plies with the inboard ply, being a polycarbonate.

Introduction of a second phase to the glass, either by bulk crystallization or by deliberately admixing with solid powders, causes advancing crack-fronts to be arrested or diverted, resulting in absorption of energy to enhance the fracture toughness [56]. This can substantially contribute to strengthening.

Thermal tempering is one of the more commercially exploited methods of strengthening glasses. A glass is rapidly cooled from well above the glass transition range to develop surface compression [56]. An applied tensile stress must overcome this layer of surface compression that results in strengthening. The science of compressive stress

development is quite complex. The various layers of the glass article cool from above the glass transition range with an initial temperature gradient through the thickness at different cooling rates and pass through the glass transition at different instants of time. A parabolic stress profile is expected — outside layers develop compression and the interior develops area-balanced tension. An elaborate description of the underlying science and technology of the process is available elsewhere [117].

The technique of overglazing is concerned with the fusion of a glaze of lower thermal expansion coefficient to the substrate product, that results in the development of a large surface compression. Strengthening of glass tubes and containers by flame-sprayed glazing has been reported [118].

Chemical strengthening of glasses is a common practice that involves an ion-exchange process, in which, host alkali ions with lower ionic radii in the glass are exchanged with larger ions from a salt bath. The process occurs below the transition temperature. $\text{Na}^+ \leftrightarrow \text{K}^+$ from a KNO_3 bath and $\text{Li}^+ \leftrightarrow \text{Na}^+$ from a NaNO_3 bath are the traditional exchanges employed [56]. The science and technology of chemical strengthening has been reviewed in several studies [119, 120, 121]. Examples of chemically strengthened glass products are aircraft cockpit windshields, display cover glass in smartphones such as the Gorilla® glass.

Strengthening and surface hardening by ion implantation is a relatively new approach. Chemical strengthening by implanting Ar^+ has been reported [122]. In another report, plasma was struck using a source containing ions such as Li^+ , K^+ , Mg^{2+} , using $\sim 50\text{V/mm}$ electric field to drive ions into the float glass [123]. Ion penetration is shown to be from 7 to 50 μm with strengths in the range of 200 to 400 MPa achieved in 1-20 minutes of plasma treatment.

The following sub-section describes the different approaches of hardening the glass surfaces. It is to be noted that the term “strengthening” has been used in the text to refer to an overall effect of mechanical strength of the glass product, including the surface and the bulk. The term “hardening” is predominantly a subsurface effect, and it literally refers to an increase in the resistance to plastic deformation.

1.4.2 Hardening techniques

The goal of this sub-section is to highlight some of the known methods of hardening the glass surfaces.

The microhardness of silicate glasses was shown to increase with N⁺ ion implantation [124]. The energetic ions that bombard the glass surface lose energy by inelastic collision with the stationary atoms and by excitation that causes the appearance of a vacancy in the glass structure along with interstitial clusters in the surface of the implanted glass. The implanting defect and foreign atoms lead to an expansion of the bombardment zone in the surface layer. Since this is constrained by the substrate, intense lateral compressive stress may be generated to enhance the hardness. Another study claimed to have used argon, nitrogen, carbon and potassium ions with energies in the range of 45-300 keV [125]. At low doses, the hardness decreased with an increase in both friction and surface stress, that was attributed to the electronic damage produced by ion implantation. At higher doses, the hardness increased again to reach a maximum, similar to the behavior of crystalline materials.

The hardness, elastic modulus and fracture toughness of SLS glass were shown to increase by doping egg-shell (ES) powder [126]. Different phases such as gypsum, nepheline, aragonite, cristobalite etc. were evidenced in the ES doped SLS glasses produced by melt-quenching. The enhancement of the mechanical properties was attributed to an increase in the degree of polymerization of the glass network [126].

The addition of peanut shell (PS) powder to SLS glass up to 5 wt % as a dopant was also reported to enhance the mechanical properties like hardness, Young's modulus and fracture toughness [127]. Crystalline phases like anorthite and magnesium aluminum silicate were evidenced. A similar reason was proposed in having an increased degree of polymerization of the glass network to strengthen the Si-O-Si bonds. The brittleness also decreased with the addition of PS.

The microhardness of the glass surface can also be improved by the ion-exchange process that forges the basis of chemical strengthening as discussed in Section 1.4.1. One of the studies of the chemical tempering of SLS glasses reported an enhancement in microhardness by 8-17%, accompanied by a decrease in crack initiation probability by 50% [128].

Having discussed about the different existing methodologies of strengthening and hardening of silicate glasses, I find it necessary to point out that there persists a lack of a thorough insight on the intimate relationship between the surface mechanical and structural properties of SLS glasses. This study is aimed to bridge the gap in knowledge in this field with a significant contribution to the understanding of the structure-property relationship. Superheated steam in the vicinity of the glass transition temperature was considered as a medium of interaction with the SLS glass surface to modify the surface structural and mechanical properties. To the best of my knowledge, superheated steam at temperatures around 500 °C hasn't been reported to be used for the treatment of SLS glasses for surface modification. This is the first report of this kind.

Chapter 2 describes the relevant experimental work associated with superheated treatment and the techniques used for the characterization of surface structural and mechanical properties.

2 Methodology

The experimental work with relevance to the treatment of soda-lime-silica glass surface with superheated steam forms the basis of this chapter. The analytical methods used to characterize the influence of superheated steam on surface structural and mechanical properties are described subsequently.

Two different types of SLS glasses were considered in this study – container glass and microscopic glass slides. The specimens were subjected to superheated steam treatment in close proximity of the glass transition temperature (T_g). The characteristics of the SLS specimens used are reported below.

2.1 Characteristics of as-received SLS glasses

Soda-lime-silica container glass bottles with flat surfaces supplied by ‘Wiegand-Glas’ were used in this study. The surfaces of the container bottles were not subjected to any hot-end or cold-end coatings during production. The glass bottles were green in color. Cylindrical glass samples with flat surfaces of diameter 25 mm and thickness 3 mm were cut out of the bottles by drilling (wet-cutting process) while ensuring to avoid any mechanical injury to the surface, except the edges. The elemental composition of the as-received container glass as obtained by ICP-OES analysis consisted of (in wt%): 31.4% Si, 49.5% O, 7.4% Ca, 8.7% Na, 1.1% Mg, 0.9% Al, 0.6% K, 0.3% Fe.

Standard microscopic glass slides (Thermoscientific, Menzel Gläser, ISO 8037/1) cut to the dimensions of (25x25x1) mm were used as the other variant of SLS glass. It was manufactured by a vertical stretching process, e.g. Fourcault. The elemental composition of the as-received glass slides reported by ICP-OES consisted of (in wt%): 31.9% Si, 49.7% O, 4.5% Ca, 9.9% Na, 2.5% Mg, 0.8% K, 0.6% Al.

The glass transition region (T_g) of the SLS glasses were determined by adopting the approach of ISO 7884-8:1987-12. Dilatometric analysis was performed at a heating rate of 5 °C/min using the device Netzsch 402 E/7/E-Py. The ranges of T_g and dilatometric softening point (T_d) that were experimentally obtained for both types of studied SLS glasses are shown in Figure 2.2.

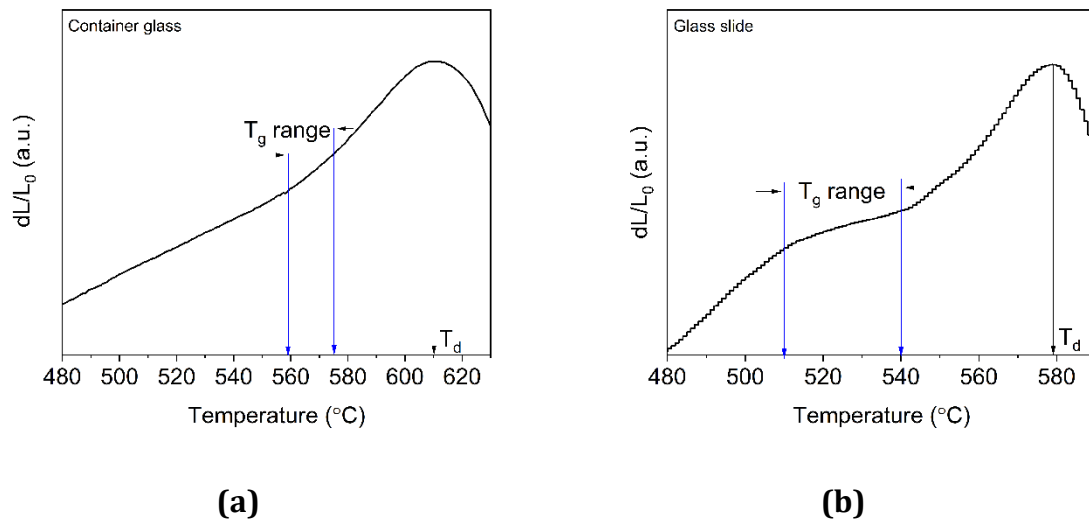


Figure 2.1. Determination of glass transition region (T_g) of the studied soda-lime-silica glasses by dilatometry (a) container glass (b) glass slide

The T_g was determined to be confined within the range of 559 $^{\circ}\text{C}$ to 575 $^{\circ}\text{C}$ for the SLS container glass, and 510 $^{\circ}\text{C}$ to 540 $^{\circ}\text{C}$ for the SLS glass slide.

The viscosities of the studied SLS glasses as functions of temperature were obtained by the 'BatchMaker' software. The glass compositions were entered into the software to estimate the viscosity as a function of temperature based on a statistical model [129]. The characteristic fixed points corresponding to specific temperatures were also determined by the software. Figure 2.2 shows a comparative plot of viscosity vs temperature of the as-received container glass and glass slide.

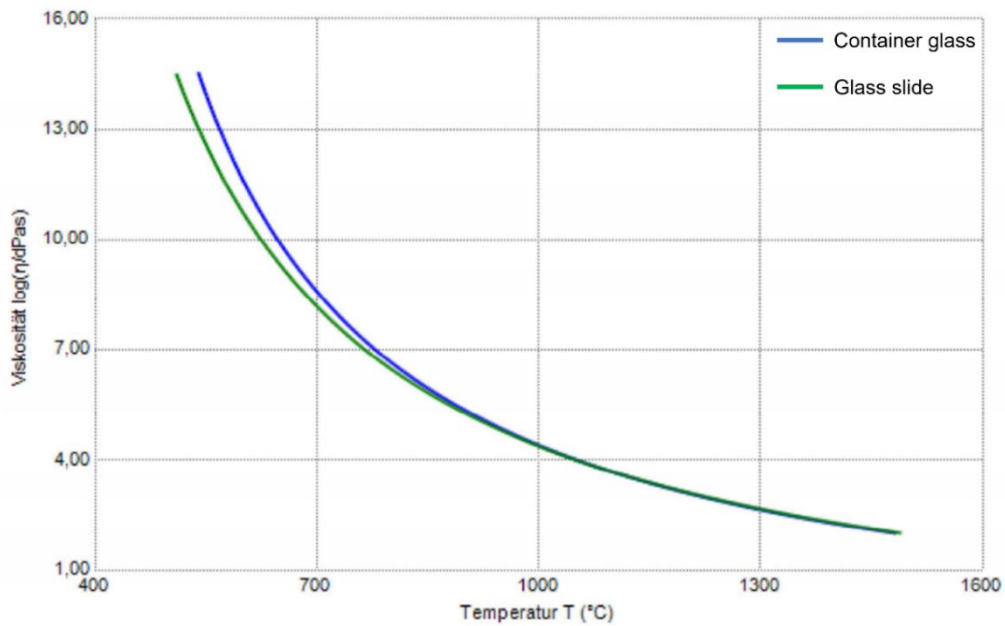


Figure 2.2 Viscosity vs temperature curve of container glass and glass slide obtained by BatchMaker software

The characteristic temperatures on the curves dependent on specific viscosities are tabulated below.

Table 2.1 Characteristic points on the viscosity-temperature curves of the SLS glasses, estimated by the BatchMaker software

Point	Viscosity log(dPa.s)	Container glass (°C)	Glass slide (°C)
Melting point	2	1485 ± 14	1492 ± 12
Working point	4	1053 ± 11	1052 ± 10
Flow point	5	934 ± 10	929 ± 9
Littleton's softening point	7.6	746 ± 7	730 ± 6
Glass transition temperature (T _g)	13.3	563 ± 8	534 ± 8

The distinction between long and short glass stems from the magnitude of the temperature interval between the working point and the softening point [1]. It is known as the working range. The time taken by the glass melt to reach from the working point to the softening point is also a crucial parameter of relevance. Melts with a large working range are often referred to as long glasses. Contrastingly, melts with relatively small working range are known as short glasses. The glass slide is a relatively longer glass, and the container glass is a shorter glass based on the differences in predicted temperatures between the working point and Littleton's softening point. The glass transition temperature (T_g) of the container glass was experimentally found to be slightly higher than the glass slide as shown in Figure 2.1. This is in close agreement with the predicted values by the BatchMaker software, reported in Table 2.1.

2.2 Experimental setup of superheated steam treatment

The experimental setup built for superheated steam treatment in laboratory scale consisted of four major components — steam generator, over-heater, tube furnace and condenser. The process scheme is shown in Figure 2.3.

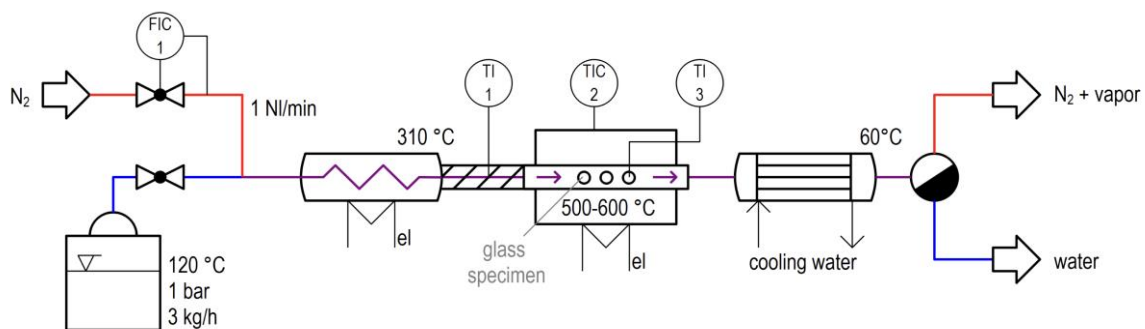


Figure 2.3 Process schematic of the experimental setup of superheated steam treatment

Liquid water was purged into the steam generator (Kärcher SC5), that produced saturated steam at a maximum flow rate of 3 kg/hr. The saturated steam was then passed through an over-heater to obtain superheated steam. The maximum temperature of the superheated steam at the outlet of the over-heater was measured to be around 310 °C by placing an external thermocouple. The outlet of the over-heater was connected to a tube furnace (Carbolite HST 12/400) with a stainless-steel tube. The temperature of the tube

furnace could be adjusted as per requirement (up to 600°C in this study). The maximum operating temperature of the tube furnace was 1200°C. The glass surface was directly exposed to a continuous laminar flow of superheated steam in the stainless-steel reactor. The superheated steam (at 310°C) entered the tube to be heated up further during its flow to reach very close to the target temperature programmed in the tube furnace. The actual temperature of the glass specimen during steam-treatment was monitored by another external thermocouple, which was placed right below the specimen. The superheated steam was subsequently guided to a condenser (tube bundle heat exchanger – model: SP-155, heating surface area: 0.33 m², number of tubes: 30), which was connected at the outlet of the tube furnace. The condensed warm water was collected to make up the balance. The process was conducted under a supporting flow of nitrogen gas (producer: 'Riessner Gase', purity: 99.999%, humidity ≤ 5%, oxygen ≤ 3%, hydrocarbons ≤ 0.2%) through the tube furnace at a rate of 1 Nl/min.

2.3 Characterization Techniques

The influence of superheated steam on the surface mechanical and structural properties was investigated by complementary characterization techniques.

2.3.1 Surface mechanical properties

The modification of the surface mechanical properties caused by superheated steam was analyzed by measuring the effect on subsurface hardness and scratchability of the glass surfaces.

2.3.1.1 Hardness

Surface hardness was measured by instrumented indentation technique using Fischerscope HM2000. The loading rate was fixed at ' $d\sqrt{F}/dt = \text{constant}$ ', with a load application time of 20 seconds. 16 indentations were performed on each sample across an array of 4x4. The load-displacement curves were dynamically generated during the penetration of the Vickers indenter from the glass surface to specific depths defined by the applied load to evaluate the Martens hardness, expressed in N/mm². The Martens hardness, HM, was evaluated by the approach described in Chapter 1, section 1.2.4. The software 'WIN-HCU' was used to process the data.

2.3.1.2 Scratch test

Scratch tests on the SLS glass surfaces were performed by an Erichsen Lineartester Model 249 using a tip 16/505 according to ISO 1518-1, with scratch stylus 'B' having a hemispherical hard-metal tip of diameter 1 mm. A fixed (high) load of 5 N was applied during the dynamic scratch tests through the length (diameter) of the glass sample at a high speed of 25 mm/s to form straight, fine surface scratches in the microabrasion regime, visible to the naked eye. The device enabled constant load application in a uniformly controlled manner during the scratch tests. The experiments were performed in a laboratory with a surrounding temperature of approximately 25 °C and relative humidity in the range of approximately 60% to 65%. The surface scratches were qualitatively examined by a field emission scanning electron microscope (SEM) (Model: Zeiss Sigma 300 VP). Secondary electron signals at a low accelerating voltage of 3 kV were used to generate surface-sensitive microstructures.

2.3.2 Surface structural network

The influence of superheated steam on the alteration of the surface structure was investigated by complementary spectroscopic techniques. The technical aspects of the analytical methods are described in the following sub-sections.

2.3.2.1 Attenuated total reflection infrared spectroscopy

The hydroxyl groups in the near-surface region were detected by attenuated total reflection infrared (ATR-IR) spectroscopy, according to the principle described in Chapter 1, section 1.2.1. The spectra of the glass surfaces before and after treatment with superheated steam were obtained by Bruker Tensor 27. A typical ATR-IR setup consists of a crystal (refractive index, n_1) that is in intimate contact with the sample surface (refractive index n_2). When the angle of incidence is higher than the critical angle ($\arcsin(n_2)/(n_1)$), total internal reflection of the IR beam at the crystal/sample interface causes an evanescent wave to penetrate into the sample that renders surface-sensitivity. A diamond crystal was used, for which the angle of incidence was fixed at 45°. The interaction of the evanescent wave with the absorption bands of hydroxyl groups in the specimen attenuated the total reflection (R), which was detected and converted to log

(1/R) to evaluate the absorbance intensity. 100 scans were performed with a resolution of 1 cm^{-1} in the spectral range of 2700 cm^{-1} to 4000 cm^{-1} corresponding to the OH stretching vibrations. The obtained spectra were baseline-corrected and smoothed, and the processed data is reported in Chapter 3.

2.3.2.2 X-ray photoelectron spectroscopy

X-ray photoelectron spectroscopy (XPS) was used to study the influence on elemental composition as well as the surface structural changes as a function of depth from the glass surface, as described in Chapter 1, section 1.2.2.1.2. A PHI 5000 Versa Probe III spectrometer with an Al K alpha source (1486.6 eV) was used to conduct XPS studies. Monochromatized X-rays were obtained by quartz crystal. Sequential XPS measurements were performed at specific time intervals in conjunction with Ar⁺ sputtering at 5 kV. The target current on the specimen holder was 3 μA while the focus beam current was 302 nA at the Faraday cup. Surface charge neutralization was achieved by the virtue of a dual beam charge neutralization system that utilizes both a cold cathode detector hood source and a very low energy ion source (<10 eV) to provide turnkey charge neutralization. The pass energy was 26 eV, while the spectral resolution was about 0.2 eV.

All spectral fittings were performed by 'MultiPak' software using Gaussian-Lorentzian composite function after Shirley background correction [130]. The best curve-fits were obtained in terms of the lowest chi-squared values (χ^2) – representative of the goodness of fit. 10%-Lorentzian component was included in O1s curve-fits to take into account the uncertainty principle associated with the core hole lifetime [47]. The curve-fittings were performed in unconstrained manner [7] while ensuring that the full-width at half maxima (FWHM) of overlapping peaks lie within a narrow range of less than 0.3 eV.

According to theory, O1s and Na1s spectral lines consist of a singlet, whereas, the Si2p spectrum is typically constituted of a spin orbit doublet. The Si2p_{1/2} peak intensity was precisely assigned half the intensity of Si2p_{3/2} in accordance with the theoretical requirement [131]. Identical FWHM values were assigned to both the peaks. The difference in binding energies between Si2p_{1/2} and Si2p_{3/2} peaks is 0.617 eV. Instead of the general tradition of C1s [132], the Ca2p spectral line was used as the standard reference while all other peaks were auto-shifted to its reference. The technical reason behind this, being the relative immobility of Ca²⁺ ions within the glass structure at room

temperature, which apparently eliminates the necessity of its analysis. Furthermore, carbon was negligibly present in the studied SLS glass specimens.

2.3.2.3 Surface topography by Atomic Force Microscopy

Atomic force microscopy (AFM) was used to study the influence of superheated steam on surface topography. The surface profile height as well as the void depths within the first monolayers were determined by AFM. High-resolution AFM measurements were performed by 'Bruker Dimension icon' (z-resolution ≈ 1 Angstrom). A silicon nitride cantilever tip was used to scan in tapping mode with a set point amplitude of 820 mV. A defined area of $1 \times 1 \mu\text{m}^2$ with 512 pixels was scanned on the untreated SLS surface. The same spot was tried to be located to the best of our ability, to re-scan after superheated steam treatment, for a precise study of the alteration of surface topography. A flood mask of 2 Angstrom was applied in the software of scanning probe microscopy 'Nanoscope Analysis' after 3rd order flattening, to map the silicate network on the topmost surface layer disseminated by the inherent voids in the form of nanochannels.

2.3.3 Bulk structural network

2.3.3.1 Solid-state nuclear magnetic resonance spectroscopy

Solid-state ^{29}Si MAS NMR study of the SLS glasses was performed to investigate the distribution of Q^n species in the bulk structural network. SLS glass in powder form was subjected to the measurements using Bruker Avance II 300 (magnetic field 7.05 T) in a 4-mm triple resonance probe. The samples were spun at 10.0 kHz. The spectra were obtained using a quantitative one-pulse experiment with a 90° pulse length of 3.5 μs and a recycle delay of 60 seconds. ^{29}Si spectra were referenced indirectly with $\text{N}(\text{SiMe}_3)_3/\sigma(\text{iso}) = 2.4$ ppm with respect to tetramethylsilane (TMS) ($\sigma(\text{iso}) = 0.0$ ppm).

3 Results and Discussion

This chapter is focused on describing the influence of superheated steam on the surface mechanical properties while drawing a correlation with the modification of the surface structure of SLS glass. The intention is to establish a relationship between the surface structural and mechanical properties by considering superheated steam as a medium of interaction with the glass surface in the vicinity of the glass transition region. The characteristics of the two categories of SLS specimens used are described in Chapter 2, Section 2.1. The glass surfaces were exposed to a continuous flow of superheated steam using the experimental setup described in Section 2.2. The temperature and duration of the treatment were varied to identify any distinguishable influence on the hardness and the structural network of the SLS surfaces, as elaborated in the following sections.

3.1 Influence of superheated steam on surface mechanical properties

3.1.1 Subsurface hardness

The variation of subsurface hardness was studied as a function of temperature and duration of steam treatment in the vicinity of the glass transition region of the container SLS glass. The T_g of the container glass was experimentally determined to be confined in the range of 559 °C to 575 °C, as stated in Chapter 2, Section 2.1 (see Figure 2.1). The temperature of superheated steam was varied between 480°C and 600°C for durations ranging from 5 minutes to 4 hours. Preliminary measurements of Vickers hardness at loads greater than 1 N corresponding to penetration depths over a micrometer below the glass surface did not exhibit any distinguishable change in hardness. This was indicative of the influence of steam limited to the near-surface region less than a micrometer below the surface. It was essential to identify the effective depth of influence of superheated steam below the surface. This necessitated the characterization of subsurface hardness by instrumented indentation technique that recorded the corresponding load-displacement curve during the measurement, as discussed in Chapter 1, Section 1.2.4. There wasn't any distinguishable influence on hardness at a load of 50 mN corresponding to a depth of penetration around 650 nm below the surface. However, when the load was decreased to 10 mN, there was a detectable change in hardness caused by the influence

of superheated steam at a depth below 300 nm. Figure 3.1 shows the statistical plot of the significance of variation in hardness as a function of temperature and duration of steam at an applied load of 10 mN. Sixteen indentations were performed across an array of 4x4 on each sample. Three samples of each category were measured. The results presented in Figure 3.1 are representative of 48 indentations of each category.

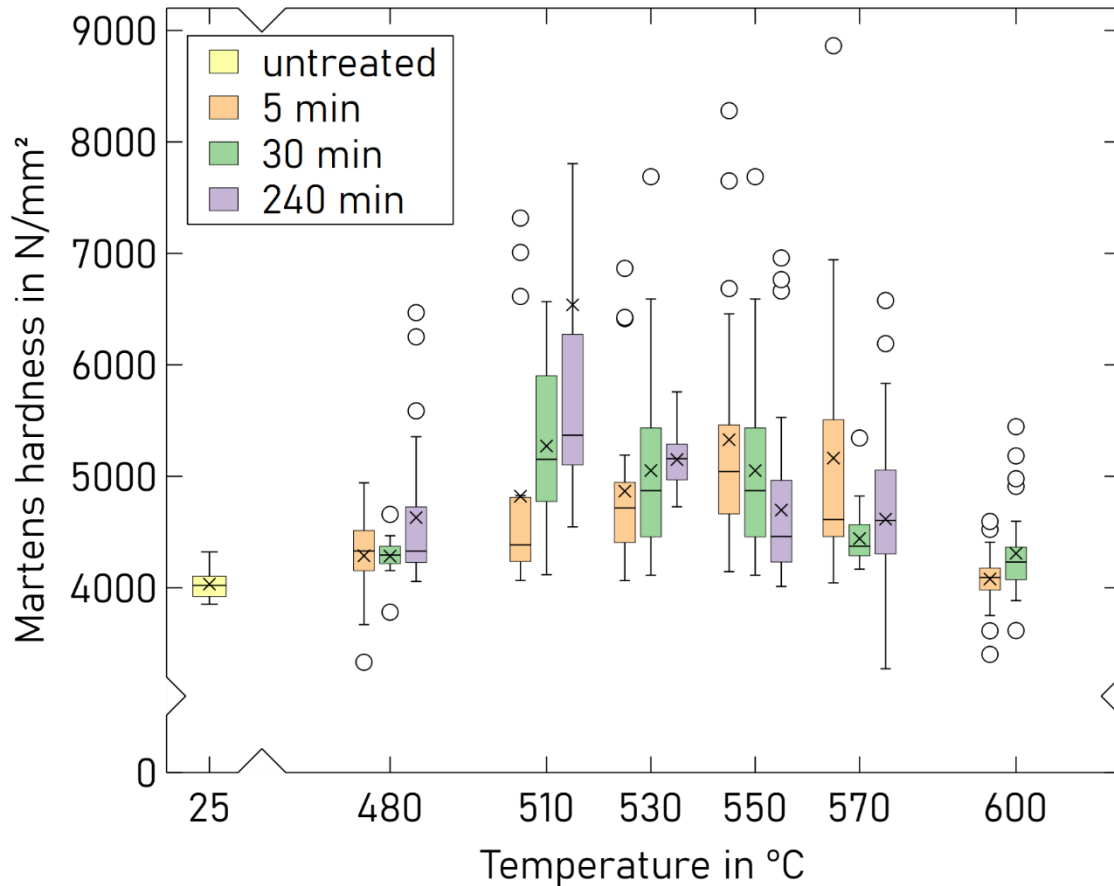


Figure 3.1 Variation of subsurface hardness of container SLS glass as a function of temperature and duration of superheated steam treatment. The applied load was 10 mN.

A consistent increment in hardness was observed with increase in temperature up to T_g , followed by a progressive decrease. This observation may be explained by an increase in network mobility with temperature that governs the diffusion of water molecules into the glass network. Optimum mobility was reached at the sub- T_g temperature of 510 °C, that was 50 °C below the onset of T_g . The subsurface hardness increased by 30% when steam-treated at 510 °C for 30 minutes. A prolonged treatment of 4 hours did not yield any

suitable effect in terms of any significant rise in hardness. With further increase in temperature beyond T_g , the hardness decreased due to the dissipation of the water molecules, owing to the increased network mobility and structural relaxation associated with lower viscosity.

Statistical analysis was performed by two-way ANOVA test to determine the effect of the independent variables — temperature and duration of steam treatment, on hardness. The resultant p-values indicated that the temperature of superheated steam had a statistically significant influence on hardness ($p= 3.6 \text{ E-}15 < 0.001$). The duration of the treatment did not have any statistically significant effect on hardness ($p= 0.08 > 0.05$). However, the interaction between the effects of temperature and time was statistically significant ($p= 7.1 \text{ E-}09 < 0.001$). This is indicative of the criticality of selecting the right combination of temperature and duration of the treatment to achieve any significant enhancement in subsurface hardness. Accordingly, the optimum process parameter of steam treatment was chosen to be 50 °C below the onset of T_g for a duration of 30 minutes, considering a 30% enhancement in hardness in container SLS glass. This set of parameters was selected for both the variants of SLS glasses considered in this study. Thus, the microscopic SLS glass slides were subjected to superheated steam at 460 °C for 30 minutes. The onset of T_g of this glass was 510 °C, as obtained experimentally (see Chapter 2, Section 2.1, Figure 2.1). Hereafter, the abbreviations H510 and S510 will be respectively used in the text to refer to the heat-treated and steam-treated container SLS specimens at 510 °C for 30 minutes. Similarly, H460 and S460 refer to heat-treated and steam treated SLS glass slides at 460 °C for 30 minutes, respectively.

The variation in Martens hardness as a function of depth from the glass surfaces is illustrated in Figure 3.2. The applied load was 10 mN. Sub- T_g heat-treatment (without steam) had a contribution of about 10% to the rise in hardness in container SLS glass (H510 specimen). Superheated steam enhanced the hardness by 30% relative to the untreated specimen, restricted to a depth of 300 nm below the surface of the S510 specimen (Figure 3.2 (a)). On the contrary, the influence of superheated steam was marginal in the SLS glass slide, reflected by a mere increase in hardness of 4% relative to the untreated specimen, as shown in Figure 3.2 (b). The reason behind the modification of subsurface hardness is explained in the subsequent sections in terms of the alteration of the surface structural network.

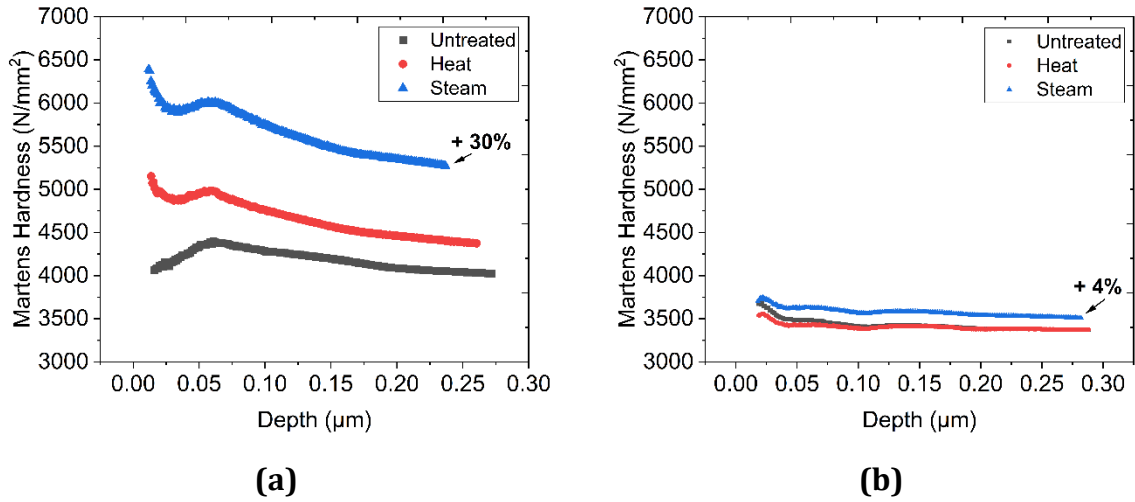


Figure 3.2 Variation of hardness as a function of depth from the SLS glass surfaces (a) container glass (b) glass slide. Peak load: 10 mN

Figure 3.2 illustrated the variation in hardness as a function of depth at a peak load of 10 mN, where the depth of penetration of the indenter was restricted below 300 nm. There was no distinguishable change in hardness of the steam-treated container SLS surface at a higher load of 50 mN, when the depth of penetration of the indenter was around 650 nm. This is shown in Figure 3.3. This was indicative of the limited influence of superheated steam restricted to the near-surface region up to around 300 nm below the glass surface. The evidence of a substantial increment in hardness caused by superheated steam in the vicinity of T_g outweighs the reported behavior of forming a soft layer with a decrease in hardness under hydrothermal treatment around 150 °C [30].

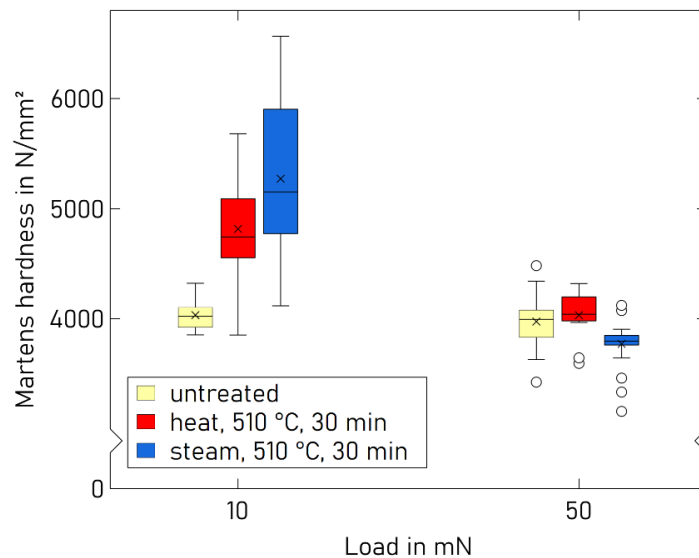
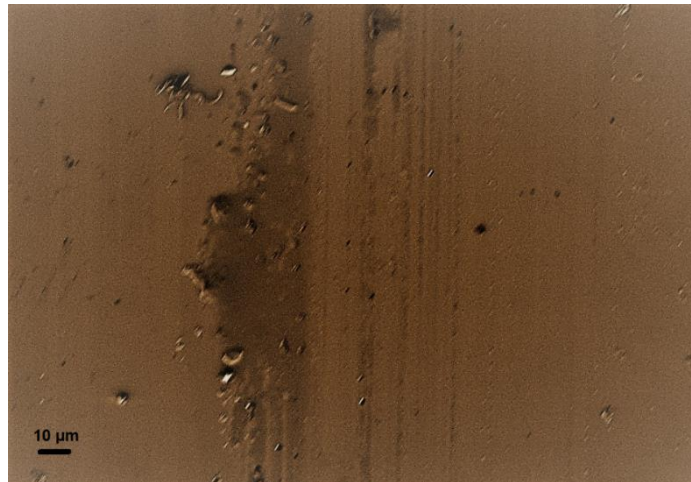


Figure 3.3 Variation of hardness of container SLS glass as a function of load

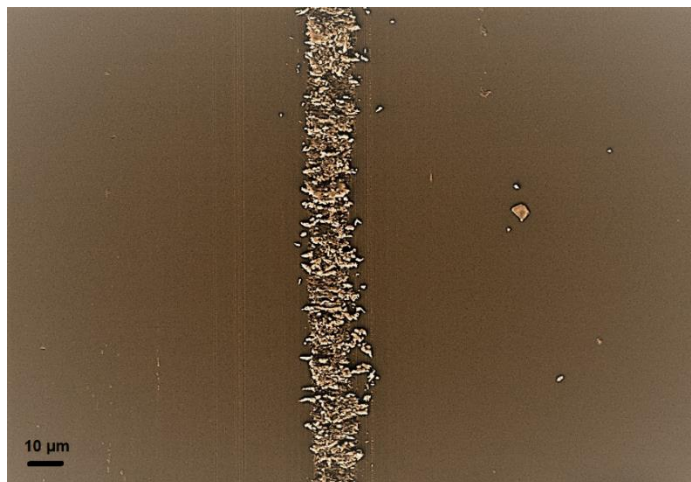
3.1.2 Surface scratch resistance

The scratch resistance of the container glass surface was characterized to determine any influence caused by superheated steam. The scratch tests were performed on the container SLS glass surface according to the methodology described in Chapter 2, Section 2.3.1.2. A uniform load of 5 N was applied across the diameter of the surface of the specimen to generate a scratch in the micro-abrasive regime [133]. The residual impression after the scratch test was qualitatively examined under scanning electron microscope (SEM). Figure 2.4 shows the SEM images of the scratches on untreated, heat-treated and steam-treated surfaces.

(a)



(b)



(c)

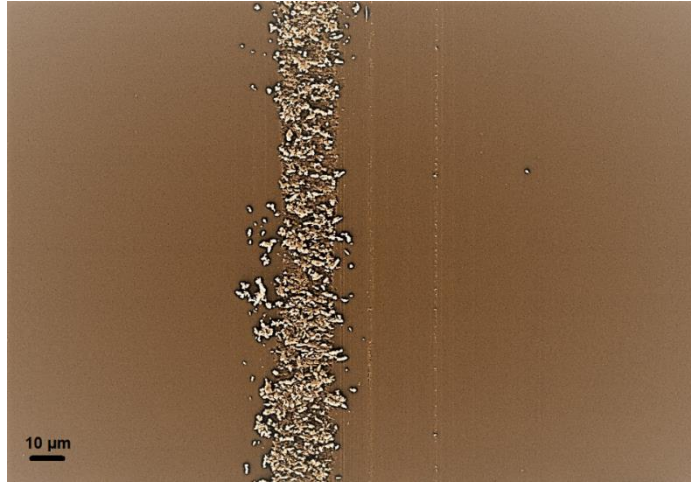


Figure 3.4 SEM images of the scratches generated at a load of 5 N on (a) untreated (b) heat-treated (c) steam-treated container SLS glass surfaces

It is clearly evident that the visibility of the scratches increases after sub- T_g heat and steam treatments relative to the untreated surface. The scratches are more prominent in Figure 2.4 (b) and (c), that suggest a decrease in scratch resistance of the surface caused by the influence of heat as well as steam at 510 °C for 30 minutes. The structural cause of the decrease in scratch resistance is explained in section 3.2.2. The subsurface hardness and scratch resistance are shown to be influenced in different ways, with an increase in the former and decrease in the latter.

The alteration of the surface nanostructure caused by the influence of superheated steam was investigated to gain a thorough insight of the structural changes accountable for the enhancement in hardness and decrease in scratch resistance. The following section describes the role of the incorporation of surface silanol groups by superheated steam.

3.2 Influence of superheated steam on surface structure

3.2.1 Hydroxyl groups

The presence of surface hydroxyl species was determined by attenuated total reflection infrared spectroscopy (ATR-IR). The information depth of ATR-IR is about 0.5-0.7 μm in the mid-IR region of OH stretching vibrations, as discussed in Chapter 1, Section 1.2.1. The spectra of the SLS surfaces were recorded within the range of 2500 cm^{-1} to 4000 cm^{-1} to investigate the influence of superheated steam. The presence of overlapping peaks

necessitated mathematical curve-fitting by Gaussian function to identify the hidden peaks. The S510 surface showed a distinguishable rise in the intensity of absorbance of the band of interest, relative to the untreated surface. There were two additional peaks towards the higher wavenumber region of the curve-fitted spectra of S510, as shown in Figure 3.3.

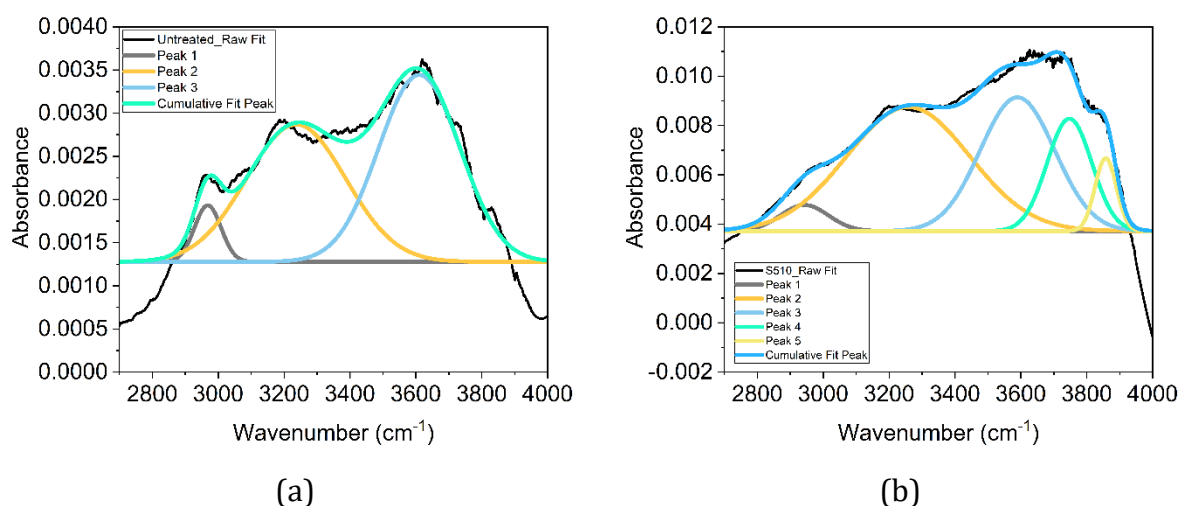


Figure 3.5 ATR-IR spectra of (a) untreated and (b) S510 container SLS surfaces. Gaussian function was used for curve-fitting (R-square > 0.9)

The different peaks of the curve-fitted ATR-IR spectra were assigned to specific OH vibrations in accordance with literatures [26, 31, 36]. The bond length increases with increasing wavenumber associated with a decrease in bond strength as described in Chapter 1, section 1.2.1 (see Figure 1.3). The peak around 3200 cm^{-1} represents a chemisorbed water molecule hydrogen-bonded to a silanol group. The peak centered around 3600 cm^{-1} corresponds to a physisorbed water molecule hydrogen-bonded to another water molecule. The additional peak observed in the S510 surface centered around 3750 cm^{-1} is assigned to the stretching vibration of a water molecule hydrogen-bonded to the bridging oxygen of a silica tetrahedral unit that is entrapped within the interstitial voids. This additional peak is also present in the steam-treated surface of the microscopic glass slide (S460), as shown in Figure 3.6. However, there is no increase in the intensity of absorbance relative to the untreated surface, unlike the container glass surface.

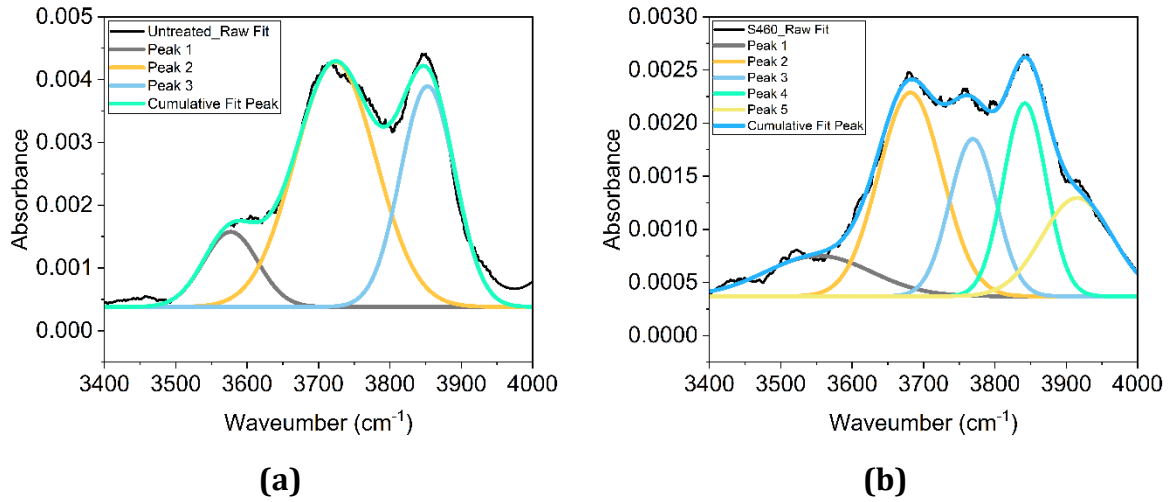
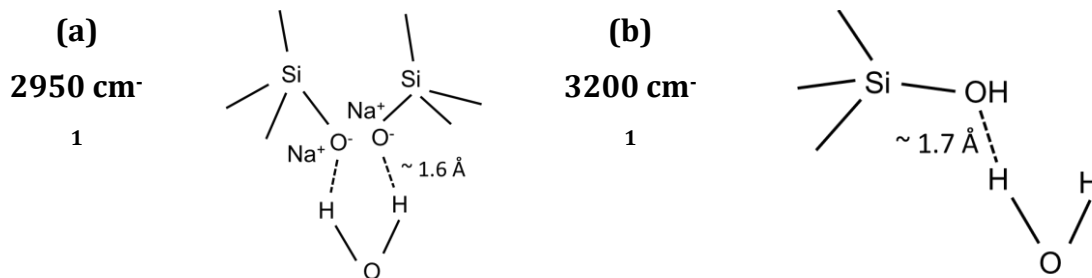


Figure 3.6 Gaussian curve-fitted ATR-IR spectra of SLS glass slide **(a)** untreated **(b)** S460

The absorbance intensity is directly proportional to the concentration of the respective hydroxyl species present in the near-surface region. The concentration of the entrapped water molecules within the silicate rings in the subsurface region of container glass is significantly higher than the counterpart of glass slide, owing to the relative rise in the intensity of absorbance by the influence of superheated steam in the former. The water molecules represented by the additional band around 3750 cm^{-1} are loosely hydrogen-bonded with a bond length of about 2.1 Angstrom, and fill up the interstitial voids within the silica tetrahedral units in the near-surface region of S510 specimen to contribute to subsurface hardening. The peaks at higher wavenumbers of 3850 cm^{-1} and 3950 cm^{-1} are ascribed to isolated silanol groups. The vibration signals of different OH groups corresponding to the peaks of the curve-fitted ATR-IR spectra are schematically represented in Figure 3.7.



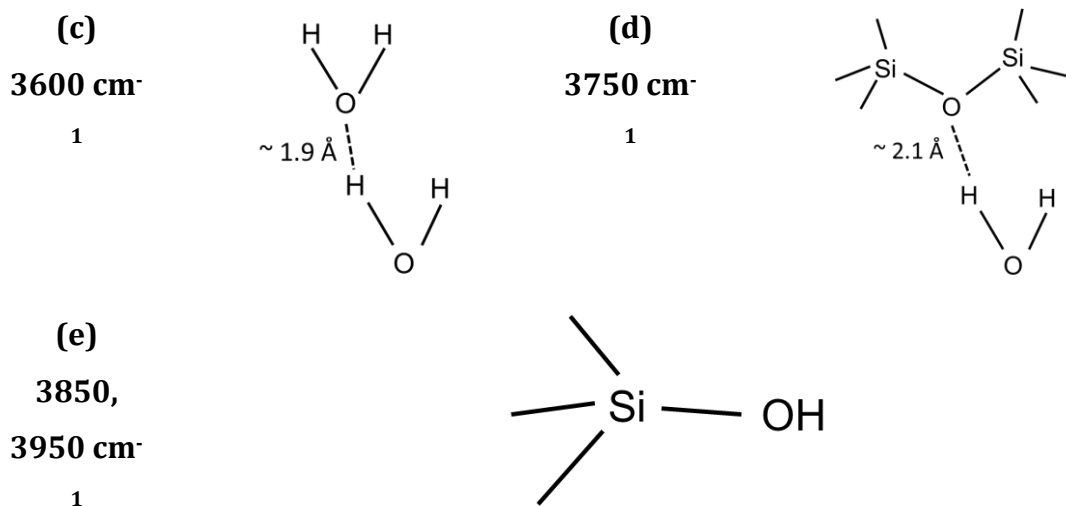


Figure 3.7 Assignment of ATR-IR peaks to specific OH vibrations

A comparative illustration of the ATR-IR spectra of superheated steam treated surfaces of container glass (S510) and glass slide (S460) is shown in Figure 3.8 to study the difference in behavior of the two glasses.

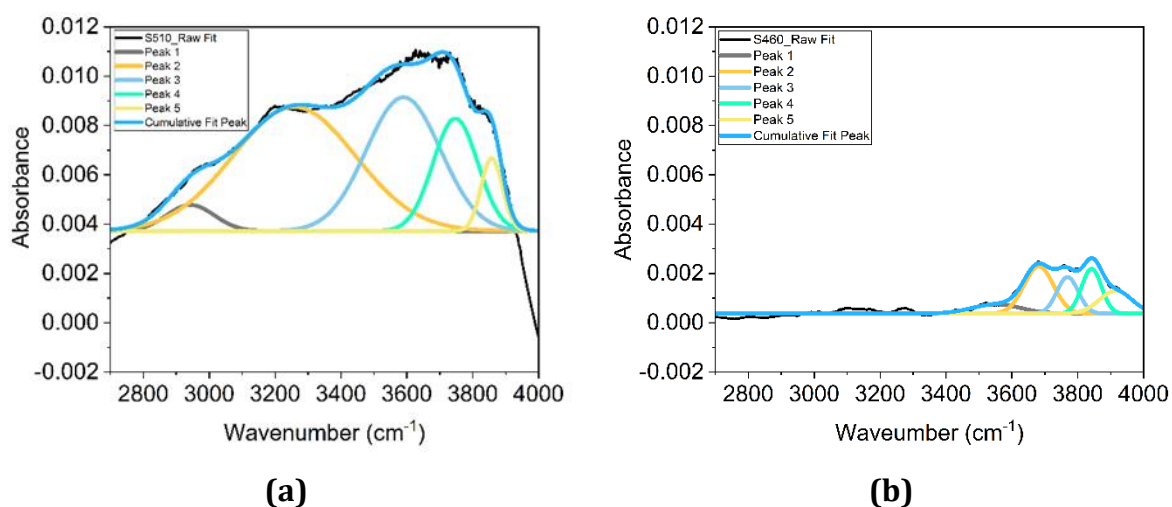


Figure 3.8 Comparative illustration of the curve-fitted ATR-IR spectra of steam-treated (a) container glass (S510) (b) glass slide (S460)

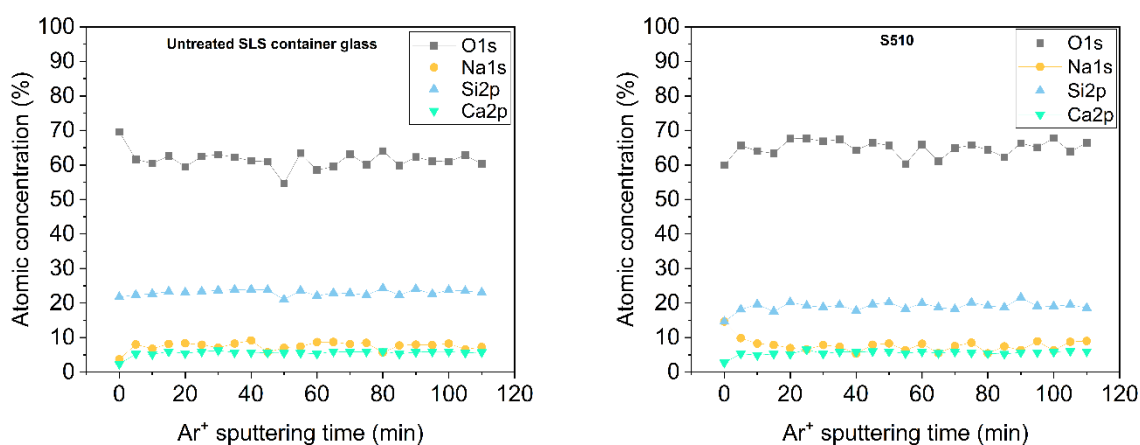
The striking difference is the intensity of absorbance corresponding to the OH stretching vibrations. Since the intensity of absorbance is directly proportional to the concentration of the corresponding species, it is evident that the interstitial voids within the container SLS surface silicate network was more abundantly stuffed up with water molecules (3750

cm⁻¹) than the SLS glass slide surface. This stuffing effect of the interstitial voids is proposed to contribute to subsurface hardening.

Having studied the influence of superheated steam on silanol groups and water molecules within the surface network, there remained an open question on the behavior of the silicate structure in the near-surface region. Thus, it was essential to investigate the alteration of the silicate network connectivity. Additionally, the potential of superheated steam to cause any ion-exchange reaction in the near-surface region associated with the volatilization of modifier cations was another subject of investigation. This necessitated the application of X-ray photoelectron spectroscopy.

3.2.2 Subsurface silicate network connectivity

X-ray photoelectron spectroscopy is a surface-sensitive tool of obtaining the chemical speciations and local chemical bonding environment of the individual elements on the outer surface up to about 10 nm, as discussed in Chapter 1, Section 1.2.2.1.1. In this work, the analysis was extended to the third dimension to study the elemental composition and structural changes as a function of depth from the glass surface by Ar⁺ sputtering. An etching rate of 1 nm/min was assumed in this study, based on a previous report of Ar⁺ sputtering on SLS glass surface under similar experimental conditions [134]. Sequential sputtering was performed for a total duration of 110 minutes that corresponded to an approximate probing depth of 110 nm. The influence of superheated steam on the elemental depth profiles of O1s, Si2p, Na1s and Ca2p are shown in Figure 3.9 for both the categories of SLS glasses.



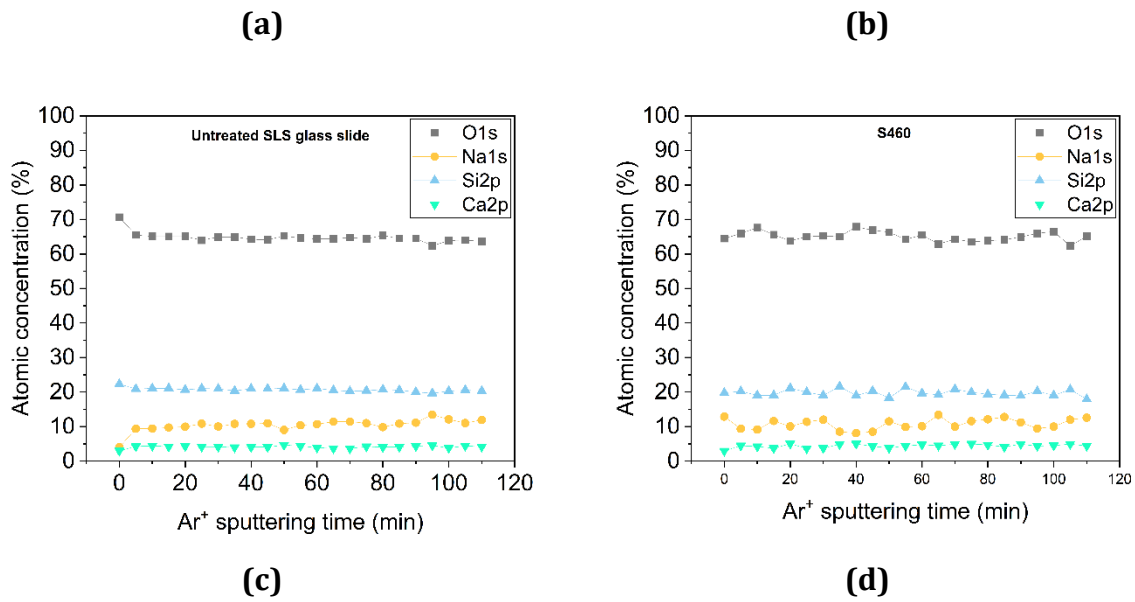


Figure 3.9 Elemental depth profile of container glass surface **(a)** untreated **(b)** steam-treated (S510); glass slide **(c)** untreated **(d)** steam-treated (S460)

Figure 3.9 serves as evidence of the absence of mobility of network modifiers (sodium and calcium ions) by the effect of superheated steam in both the glass surfaces. There was no depletion in the concentration of Na1s and Ca2p in either category of SLS glass, throughout the depth of sputtering. The lack of evidence of any ion-exchange reaction between sodium and hydronium ions in the near-surface region was unlike a previous report where an SLS glass was treated under hydrothermal conditions around 150 °C [30].

The local atomic bonding states of the oxygen atoms in the silicate network of the near-surface region were investigated by studying the O1s spectral line. It broadly lies within the binding energy range of 528 eV to 534 eV, containing overlapping signals of BOs, NBOs and hydrous species, as discussed in Chapter 1, Section 1.2.2.1.2. A typical O1s spectral line is illustrated in Figure 3.10 (a). The three relevant signals pertaining to the silicate structure of the glass network in the O1s spectral line are assigned as follows [7, 17]:

1. Non-bridging oxygen (NBO): $O_{Si-O-Na}$, corresponding to the shoulder peak around 530 eV.
2. Bridging oxygen (BO): $O_{Si-O-Si}$, corresponding to the central peak around 531 eV.
3. SiOH/H₂O species: O_{SiOH/H_2O} , corresponding to higher binding energy shoulder peak centered around 532 eV.

The assignment of the overlapping O1s peaks to the aforementioned signals corresponding to different binding energies can be explained by the electrostatic interactions [135]. This is dictated by the Linus Pauling's scale of electronegativity, which bears the following order of decreasing trend: $H > Si > Na$. Hydrogen, possessing the highest electronegativity among the three elements, has a higher tendency to attract the electron cloud of the oxygen atom. On average, it is highly likely that there are fewer electrons at the oxygen atom in Si-OH than Si-O-Si and Si-ONa. Thus, the electron-electron repulsion at the oxygen atom in Si-OH decreases, which leads to increased binding energy. This justifies the assignment of the 532 eV peak to SiOH/H₂O species. Similarly, sodium, bearing the lowest electronegativity among the three elements, is accountable for higher repulsion of the electron cloud at the oxygen atom in Si-ONa, consequently facilitating the ejection of O1s photoelectrons with a lower binding energy, in agreement with the proposition of Simonsen et al [135]. This, in turn, justifies the assignment of the intermediate peak at 531 eV to the Si-O-Si bridging oxygen, owing to the intermediate position of silicon in the order of electronegativity of the three elements apart from oxygen, which undoubtedly, possesses the highest electronegativity among the four elements in contention. The extraction of the contribution of the individual speciation was performed by fitting the high-resolution XPS O1s spectral lines by Gaussian-Lorentzian composite function. The integrated peak areas give an estimation of the concentration of the corresponding species.

The Si2p spectral fittings were performed according to the theoretical requirements [131]. The Si2p spectral line is typically constituted of a spin orbit doublet. The Si2p_{1/2} peak intensity was precisely assigned half the intensity of Si2p_{3/2}. Identical FWHM values were assigned to both the peaks. The difference in binding energies between Si2p_{1/2} and Si2p_{3/2} peaks is 0.617 eV. A typical illustration of Si2p curve-fitting is shown in Figure 3.10 (b).

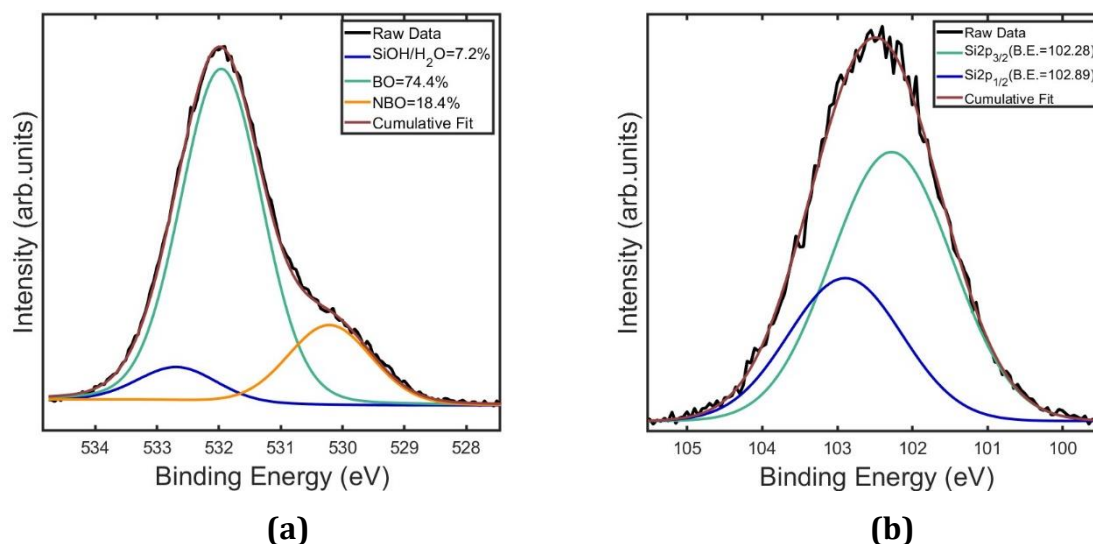
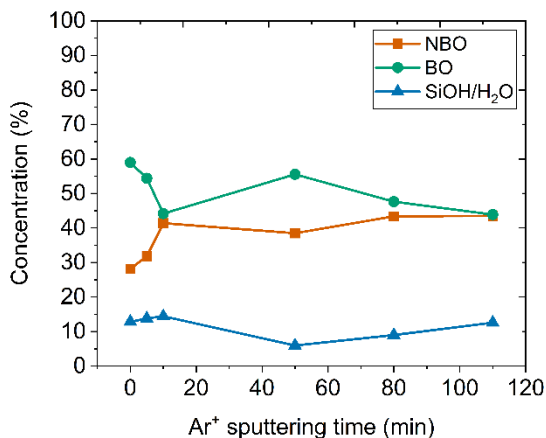


Figure 3.10. Typical illustration of (a) O1s and (b) Si2p curve-fittings by Gaussian-Lorentzian function

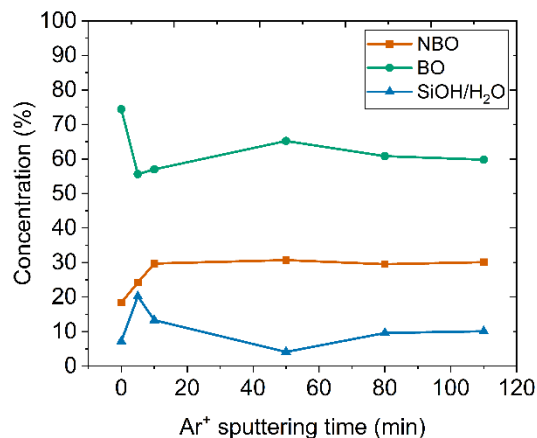
The concentrations of the individual oxygen speciations in the glass network were calculated by the normalized integrated peak areas of the respective components obtained from the curve-fittings, and represented in terms of oxygen to silicon atomic ratios to study the extent of subsurface silicate network connectivity. The O1s and Si2p curve-fittings of the untreated and steam-treated surfaces of both the variants of SLS glasses are illustrated in the Appendix (Figures A1.1-A1.8). The following sub-section describes the interrelation of network connectivity with hardness in the near-surface region of SLS glass.

3.2.2.1 Relationship between silicate network connectivity and hardness

The subsurface networks of the two categories of untreated SLS glasses were comparatively studied to distinguish the structural differences of their as-received states before superheated steam treatment. The respective concentrations of BOs, NBOs and hydrous species were extracted from the O1s curve fittings (see Appendix Figure A1.1, A1.5). A comparative plot of the variation in oxygen speciations at the subsurfaces of the two untreated glasses is shown in Figure 3.11.



(a) Untreated container glass surface



(b) Untreated glass slide surface

Figure 3.11 Concentrations of BOs, NBOs and hydrous species as a function of depth from the untreated (a) container glass surface (b) glass slide surface. Connecting lines act as a guideline to the eye.

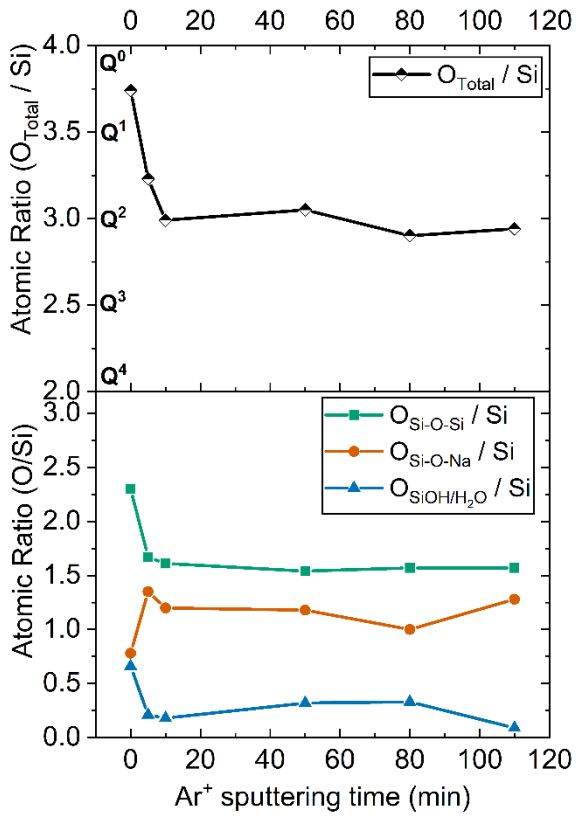
The untreated glass slide is characterized by a relatively higher concentration of bridging oxygens and lower concentration of non-bridging oxygens throughout the depth of sputtering, approximately equivalent to a depth of 110 nm below the glass surface. The NBOs and hydrous species are considered to be the “mechanically-weakening” species [136]. These reactive sites weaken the glass structure by decreasing the network connectivity, in other words, lowering the degree of polymerization of the silicate network. A higher population of these weak linkages in the subsurface network of the untreated container glass signifies lower extent of network connectivity in relation to its counterpart, the glass slide. Thus, the container glass is expected to be relatively more reactive to an external stimulus in superheated steam. This explains the higher abundance of the water molecules within the silicate rings of the steam-treated container glass corresponding to the higher intensity of absorbance of the OH stretching region in ATR-IR spectra (see Section 3.2.1, Figure 3.8). It is to be noted that the first data point without sputtering corresponds to an information depth of less than 10 nm, as discussed in Chapter 1, Section 1.2.2.1.1.

A comparative representation of the subsurface silicate network connectivity of the container glass before and after superheated steam treatment is shown in Figure 3.12. The extent of silicate network connectivity is represented by the atomic ratios of different

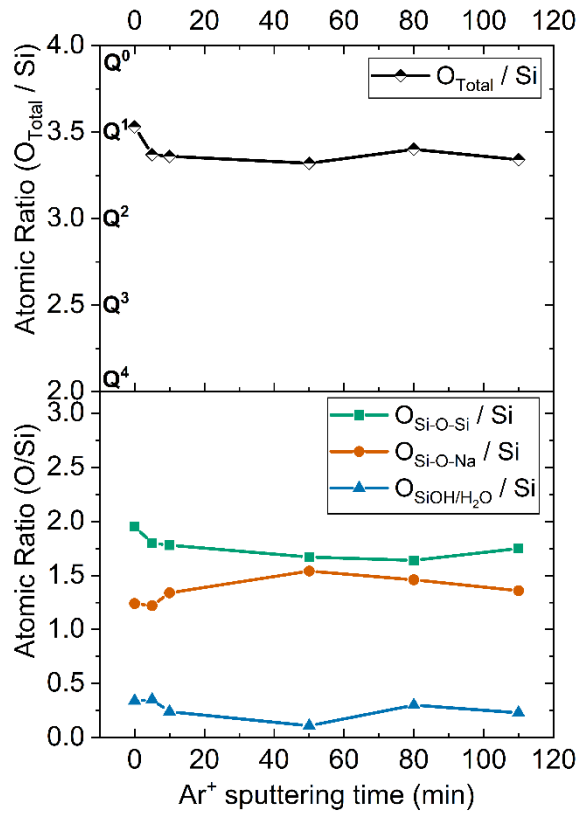
oxygen species to silicon as a function of depth from the glass surface. The corresponding individual atomic ratios are tabulated in Table 3.1.

Table 3.1 Comparative variation of the atomic ratios of different oxygen species (BO, NBO, hydrous species) to silicon as a function of Ar⁺ sputtering time before (UT: untreated) and after superheated steam treatment of the container SLS glass at 510 °C for 30 minutes (S510)

Ar ⁺ sputtering time (min)	O _{Si-O-Si} / Si		O _{Si-O-Na} / Si		O _{SiOH/H₂O} / Si		O _{Total} / Si	
	UT	S510	UT	S510	UT	S510	UT	S510
0	2.3	1.95	0.78	1.24	0.66	0.34	3.74	3.53
5	1.67	1.8	1.35	1.22	0.21	0.35	3.23	3.37
10	1.61	1.78	1.2	1.34	0.18	0.24	2.99	3.36
50	1.54	1.67	1.18	1.54	0.32	0.11	3.05	3.32
80	1.57	1.64	1	1.46	0.33	0.3	2.9	3.4
110	1.57	1.75	1.28	1.36	0.09	0.23	2.94	3.34



(a) Untreated container glass surface



(b) S510

Figure 3.11 Variation of the atomic ratio of individual oxygen speciations to silicon, as a function of Ar⁺ sputtering time (below); variation of atomic ratio of total oxygen (sum of individual contributions) to silicon, as a function of Ar⁺ sputtering time (above) **(a)** untreated container glass surface **(b)** steam-treated container glass surface (S510). Connecting lines act as guideline to the eyes

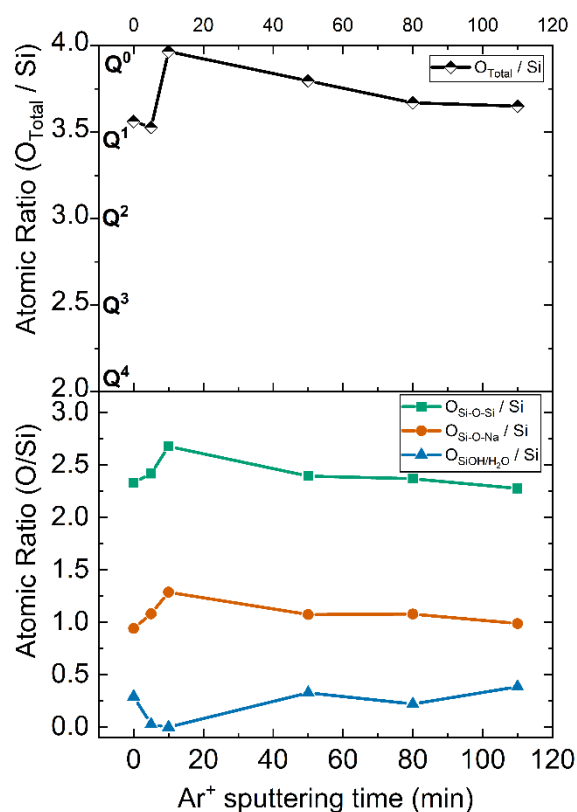
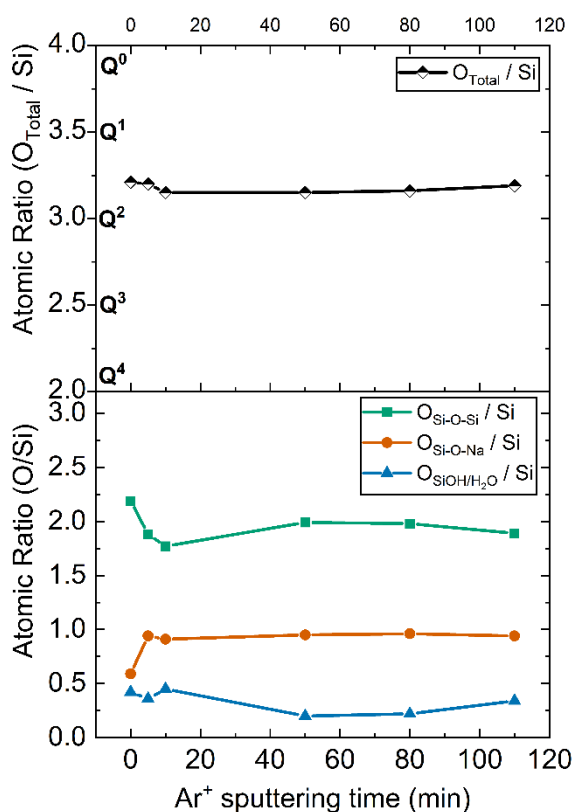
The total oxygen concentration (O_{Total}) was calculated as the sum of the contributions of the individual speciations of BO ($O_{\text{Si-O-Si}}$), NBO ($O_{\text{Si-O-Na}}$) and hydrous species ($O_{\text{SiOH/H}_2\text{O}}$) extracted from the O1s peak-fittings (see Appendix Figure A1, A3). The total oxygen to silicon atomic ratio, $O_{\text{Total}} / \text{Si}$, is representative for the Q^n structure of the silicate network [137], wherein, ‘n’ represents the number of bridging oxygens per silica tetrahedral unit. Theoretically, a value of 4.0 indicates a Q^0 species, which is a self-sustaining unit with four NBOs in a silica tetrahedral unit. A stoichiometric ratio of 3.5 is theoretically indicative of Q^1 structure associated with pyrosilicates (Si_2O_7)⁶⁻. It is marked by the presence of three NBOs linked to a silica tetrahedron. Similarly, a ratio of 3.0 represents a Q^2 structure (two

BOs and two NBOs linked to a silica tetrahedron). Q^3 and Q^4 species are reflected by $O_{\text{Total}}/\text{Si}$ ratios of 2.5 and 2.0, respectively. The experimental evidence proposes that the region constrained within the top 5 nm of the untreated glass surface (Figure 3.11 (a)) corresponding to the first data point without sputtering is essentially composed of Q^0 and Q^1 species — marked by an $O_{\text{Total}}/\text{Si}$ atomic ratio of 3.74. These are the mechanically weakening structural entities. However, it does not rule out the likelihood of the presence of stronger Q^n units ($n: 2-4$). Although the probability of encountering Q^3 and Q^4 species on the surface is lower compared to the bulk of the glass network [137]. The atomic ratio of $O_{\text{Total}}/\text{Si}$ attains a saturation close to 3.0 (Q^2 structure) throughout the depth of sputtering up to approximately 110 nm below the untreated container glass surface. The contribution of BOs (Si-O-Si) exceeds the contributions of the mechanically weakening entities of NBOs and hydrous species. The influence of superheated steam on the respective oxygen to silicon atomic ratios is shown in Figure 3.11(b). The saturation of the $O_{\text{Total}}/\text{Si}$ atomic ratio increased to 3.5 in the near-surface region, marked by Q^1 structure. On comparative consideration of the individual contributions of BOs, NBOs and hydrous species to the total atomic ratios, the concentrations of both $O_{\text{Si-O-Si}} / \text{Si}$ (BO/Si) and $O_{\text{Si-O-Na}} / \text{Si}$ (NBO/Si) increased by the influence of superheated steam. However, the increase in NBO/Si exceeded the increase in BO/Si in the near-surface region, that signified silicate network depolymerization caused by superheated steam.

The comparative illustration of the respective oxygen to silicon atomic ratios in the subsurface of the SLS glass slide is tabulated in Table 3.2 and plotted in Figure 3.12.

Table 3.2 Comparative variation of the atomic ratios of different oxygen species (BO, NBO, hydrous species) to silicon as a function of Ar⁺ sputtering time before (UT: untreated) and after superheated steam treatment of SLS glass slide at 460 °C for 30 minutes (S460)

Ar ⁺ sputtering time (min)	O _{Si-O-Si} / Si		O _{Si-O-Na} / Si		O _{SiOH/H₂O} / Si		O _{Total} / Si	
	UT	S460	UT	S460	UT	S460	UT	S460
0	2.19	2.32	0.59	0.94	0.42	0.29	3.21	3.56
5	1.88	2.41	0.94	1.08	0.36	0.02	3.2	3.52
10	1.77	2.67	0.91	1.28	0.45	0	3.15	3.96
50	1.99	2.39	0.95	1.07	0.2	0.32	3.15	3.79
80	1.98	2.36	0.96	1.08	0.22	0.22	3.16	3.66
110	1.89	2.27	0.94	0.98	0.34	0.38	3.19	3.64

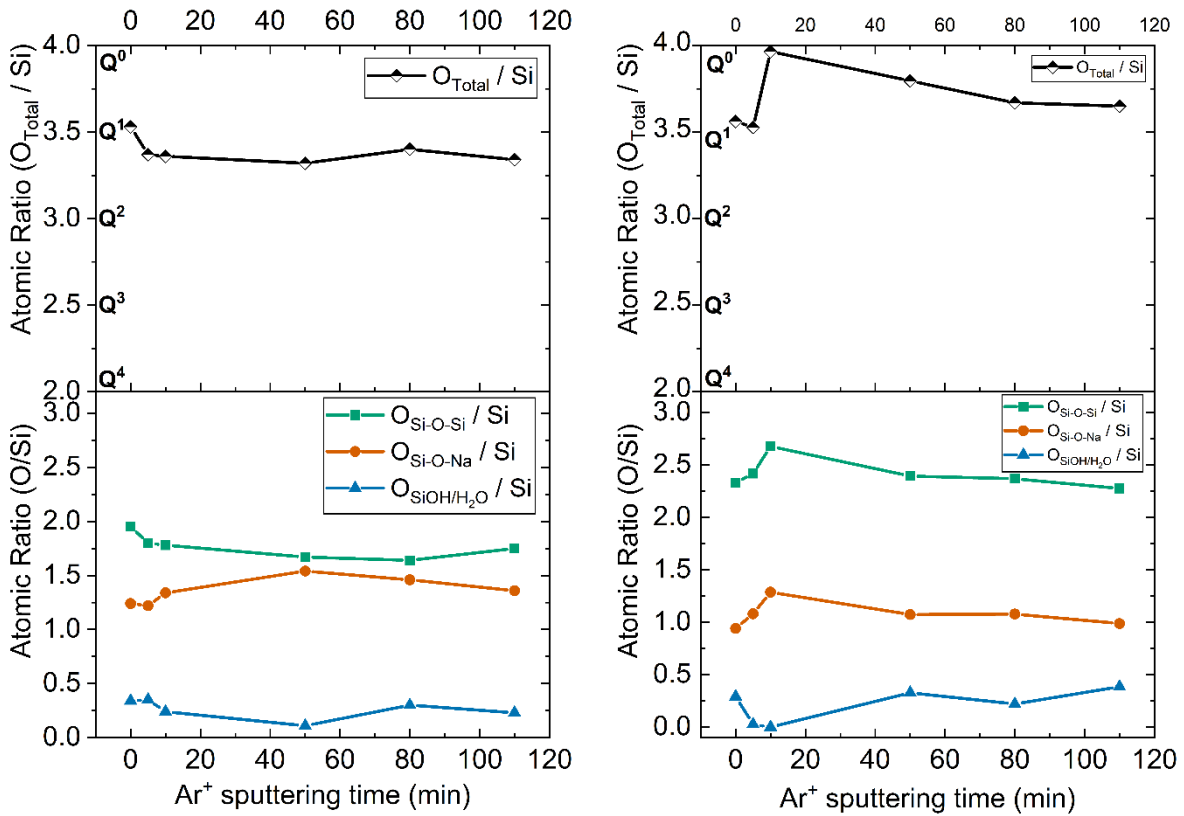


(a)

(b)

Figure 3.12 Variation of the atomic ratio of individual oxygen speciations to silicon, as a function of Ar⁺ sputtering time (below); variation of atomic ratio of total oxygen (sum of individual contributions) to silicon, as a function of Ar⁺ sputtering time (above) **(a)** untreated glass slide surface **(b)** steam-treated glass slide surface (S460). Connecting lines act as guideline to the eyes

Superheated steam increased the total atomic ratio of oxygen to silicon ($O_{\text{Total}}/\text{Si}$) in the near-surface region of the glass slide, as shown in Figure 3.12. This behavior was similar to the container SLS glass (see Figure 3.11). However, in case of the glass slide, the increase in BO/Si exceeded the increase in NBO/Si , that signified silicate network repolymerization throughout the depth of sputtering. This was in contrast with the network rearrangement evidenced in container SLS glass. The comparative illustration of the subsurface network connectivities of the steam-treated surfaces of the two variants of SLS glasses is shown in Figure 3.13. The superheated steam treated glass slide surface was marked by a relatively higher ratio of BO/Si and lower ratio of NBO/Si . A higher degree of connectivity prevented further diffusion of water molecules into the silicate network of the glass slide, unlike the container glass surface. A relatively lower effect of stuffing of the interstitial voids with molecular water in the near-surface region of the SLS glass slide meant a suppressed increase in subsurface hardness relative to its counterpart.



(a) Steam-treated container glass surface **(b)** Steam-treated glass slide surface

Figure 3.13 Variation of the atomic ratio of individual oxygen speciations to silicon, as a function of Ar⁺ sputtering time (below); variation of atomic ratio of total oxygen (sum of individual contributions) to silicon, as a function of Ar⁺ sputtering time (above). Connecting lines act as guideline to the eyes. **(a)** sub-T_g steam-treated container glass surface (S510) **(b)** sub-T_g steam-treated microscopic glass slide surface (S460)

The extent of network polymerization by the influence of superheated steam was determined by the proportion of the difference in BO/Si and NBO/Si ratios after treatment in comparison to the untreated counterparts. The contributions of both O_{Si-O-Na} and O_{SiOH/H₂O} were taken into the account of NBOs. The increase in NBO/Si after steam-treatment exceeded the increase in BO/Si in container glass surface, evident by the negative values in Figure 3.14 — indicating network depolymerization. On the contrary, the microscopic glass slide was subjected to network repolymerization by the influence of stream-treatment with the increase in BO/Si dominating the counterpart of NBO/Si with positive values in Figure 3.14.

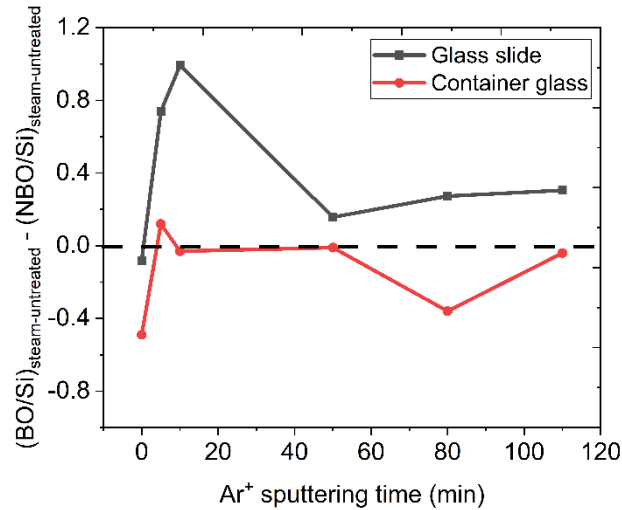


Figure 3.14 Difference in the increase in BO/Si and NBO/Si caused by the influence of superheated steam. Here, BO: $O_{Si-O-Si}$ and NBO: $O_{Si-O-Na} + O_{SiOH/H_2O}$. Positive values indicate repolymerized network after steam-treatment, while negative values are indicative of depolymerized silicate network.

The opposite behavior of network rearrangement in the two categories of SLS glasses by the influence of superheated steam could be attributed to the differences in the silicate networks of the corresponding untreated counterparts, shown in Figure 3.11. The untreated glass surface with relatively higher concentration of BOs favored network repolymerization when subjected to the interaction with superheated steam (glass slide). On the contrary, the untreated surface with relatively higher concentration of NBOs (container glass) favored network depolymerization when interacted with superheated steam. This suggested that a weaker pristine subsurface network favored the creation of NBOs by the influence of superheated steam. Consequently, it facilitated the diffusion of water molecules within the silicate network of the container SLS glass to contribute to subsurface hardening by stuffing up the interstitial voids with weakly hydrogen-bonded water molecules. This was evidenced by the relatively higher intensity of absorbance of the ATR-IR spectral vibration centered around $\sim 3750\text{ cm}^{-1}$ in container SLS glass over the counterpart of glass slide, as discussed in Section 3.2.1.

Overall, it was found that an increase in the degree of silicate network connectivity did not have any necessary impact on the subsurface hardness. The effect of stuffing of the

interstitial voids within the subsurface silicate network with molecular water played a critical role to enhance the subsurface hardness.

The following sub-section attempts to reveal the cause of scratch formation on SLS glass surface, interpreted in terms of the silicate network connectivity.

3.2.2.2 Relationship between silicate network connectivity and scratch resistance

The scratch resistance of the container glass surface was found to be directly related to the atomic ratio of total oxygen to silicon, $O_{\text{Total}}/\text{Si}$ [136]. The $O_{\text{Total}}/\text{Si}$ ratios after sub- T_g heat and steam treatments are comparatively illustrated for both the SLS glasses in Figure 3.15.

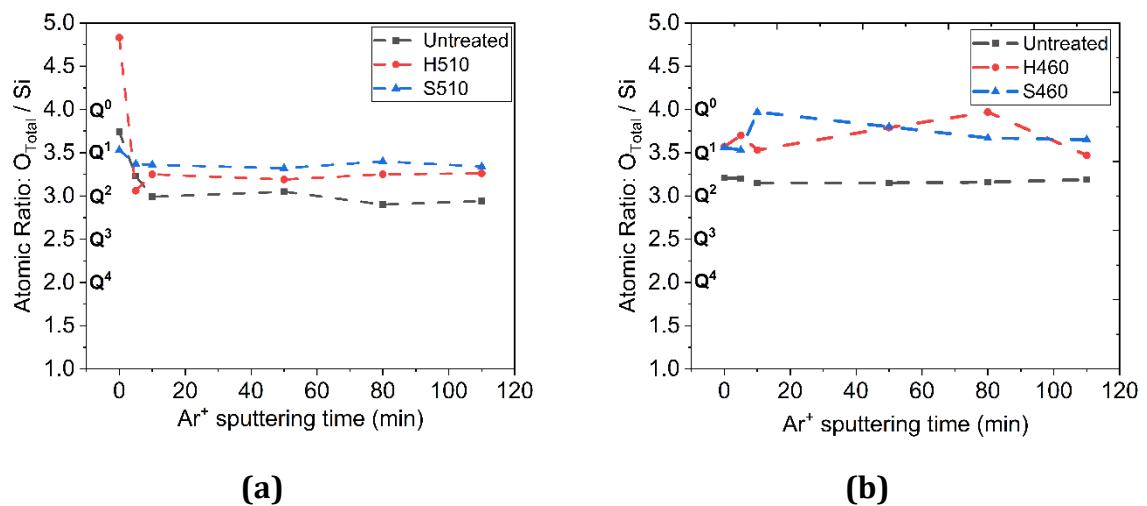


Figure 3.15 Atomic ratio of total oxygen to silicon ($O_{\text{Total}}/\text{Si}$) of untreated, heat-treated and steam-treated (a) container glass (b) glass slide as a function of Ar^+ sputtering time

The total atomic ratio of oxygen to silicon ($O_{\text{Total}}/\text{Si}$) slightly increased after sub- T_g heat treatment (without steam), with a further increase when subjected to the interaction with superheated steam. However, a high stoichiometric ratio of $O_{\text{Total}}/\text{Si}$ does not necessarily indicate weakening of the silicate network [137]. This is because of the importance of the consideration of the individual contributions of BOs, NBOs and hydrous species that account for the total oxygen concentration. The subject of the difference in the individual contributions of BO/Si and NBO/Si received prior attention in the text and were

illustrated in Figures 3.12-3.14. It is noteworthy that the XPS measurement corresponding to the first data point (without sputtering) of the H510 surface in Figure 3.15(a) yielded an $O_{\text{Total}}/\text{Si}$ ratio that exceeded 4.0. This doesn't align with the theoretical expectations. It was proposed to be due to the "free oxygens (O^{2-})" [136] that occupied the voids within the repolymerized Q^4 units on the heat-treated container glass surface.

The increase in $O_{\text{Total}}/\text{Si}$ ratio in the near-surface region between 5 nm and 100 nm was correlated to the scratch resistance of the container glass surface from the perspective of structural modification [136]. It was demonstrated that the visibility of the scratches generated in the micro-abrasive regime increased with sub- T_g heat and steam-treatment (see Section 3.1.2, Figure 3.4). The "mechanically weakening" elements associated with NBOs and hydrous species in this thin subsurface region contribute to increased vulnerability of a glass surface to scratches. Higher concentration of Q^1 and Q^2 species indicated by higher atomic ratio of $O_{\text{Total}}/\text{Si}$ in the subsurface region of heat-treated and steam-treated surfaces (Figure 3.15(a)) is proposed to be accountable for their increased susceptibility to the formation of visible scratches from the theoretical perspective.

The scratch on the untreated container glass surface in Figure 3.4 (a) is dissipated to a wider area. The scratches on heat-treated and steam-treated surfaces are confined to a narrow zone with high material pile up in the form of accumulated debris gathered in the vicinity of the scratched grooves (see Figure 3.4(b), (c)).

The root cause of scratch formation on SLS surfaces was generalized based on a comparative study of the silicate network connectivity of the near-surface and bulk structure by XPS and Raman investigations, respectively [136]. The network connectivity of the thin subsurface layer between 5 nm and 100 nm was proposed to be the critical zone of consideration. A weaker structural network in this region dominated by Q^1 species is expected to contribute to easy propagation of a surface-initiated crack to the depth of the stronger bulk network that is known to be abundantly populated by stronger Q^3 species. Any surface injuries will be subsequently accompanied by higher scratch depths, wear volume and material pile up, as observed in Figure 3.4 (b) and (c).

Having studied the influence on the silicate network connectivity of the near-surface region, there was an open question on the modification of the surface topography in terms of the void depths within the silicate rings among the first few monolayers. This was

facilitated by the effective usage of the capabilities of atomic force microscopy (AFM), as discussed in the following section.

3.3 Modification of surface topography

The surface topography of the container SLS glass was studied by AFM. The influence of superheated steam on the cross-sectional profile height was analyzed by evaluating the root mean square roughness across the surface diagonal of the same spot scanned before and after steam-treatment. The three-dimensional representations of the AFM images scanned at a definite spot of $1 \times 1 \mu\text{m}^2$ are shown in Figure 3.16. It was tried to ensure to scan the same spot after steam-treatment to precisely study the local alteration in surface topography.

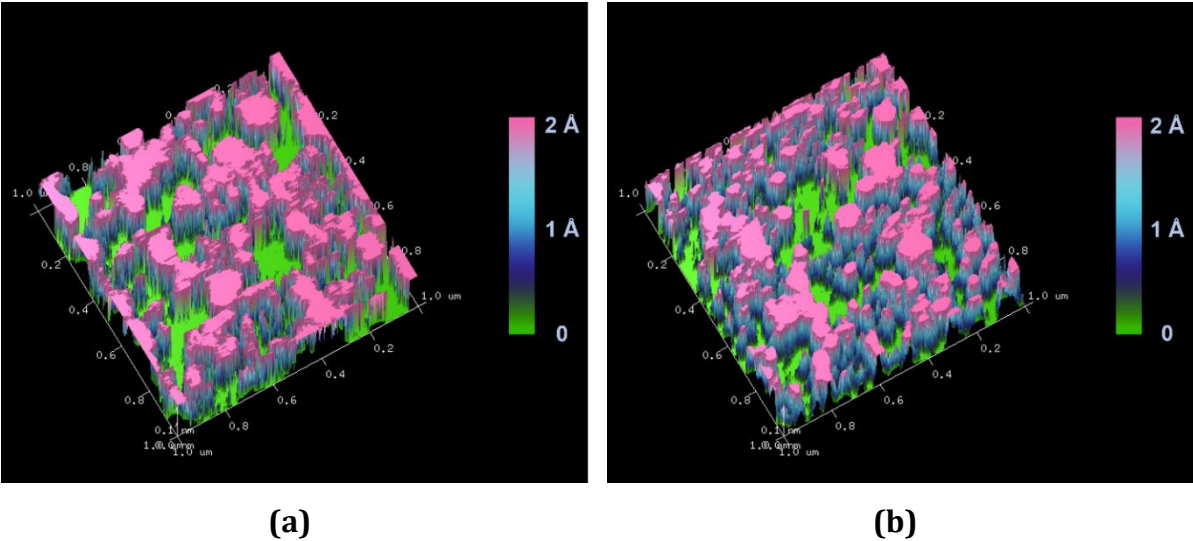


Figure 3.16 $1 \times 1 \mu\text{m}^2$ third order flattened three-dimensional AFM images of (a) untreated (b) steam-treated container glass surface

The green nanochannels represent the voids dispersed within the islands of the silicate network represented in pink. The difference in cross-sectional profile heights across the surface diagonals of both the images is illustrated in Figure 3.17.

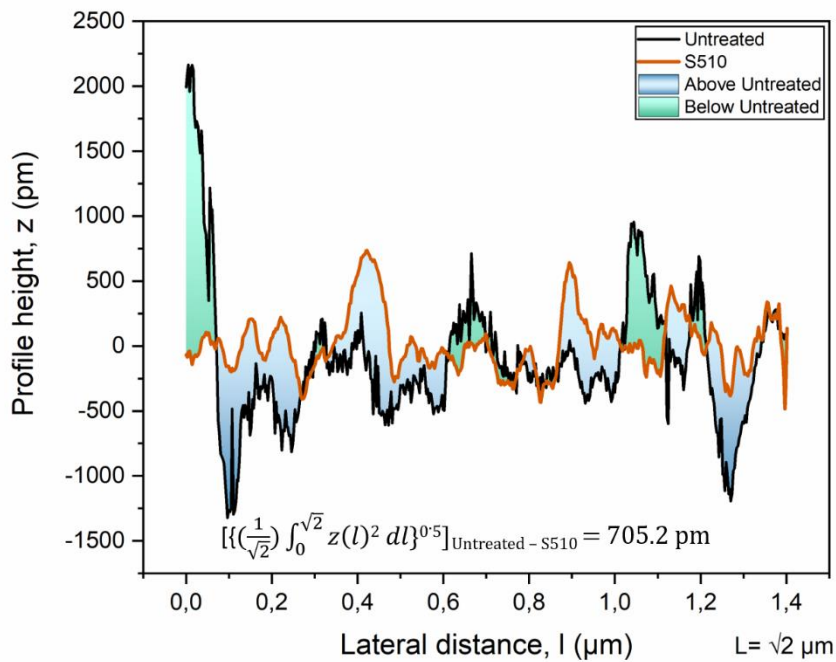


Figure 3.17 Comparative surface profile heights as a function of lateral distance across the same surface diagonal of Figure 3.20 (a) and (b), from top-left to bottom-right

The depth of the valleys (negative profile height) of the untreated surface was higher than the steam-treated counterpart — indicative of higher void depths of the untreated surface. This difference is quantitatively dictated by the difference in root mean-square roughness between the two surfaces of 705.2 picometers, calculated by the embedded equation in Figure 3.17. The difference in void depths between the two surfaces under consideration is represented in Figure 3.18.

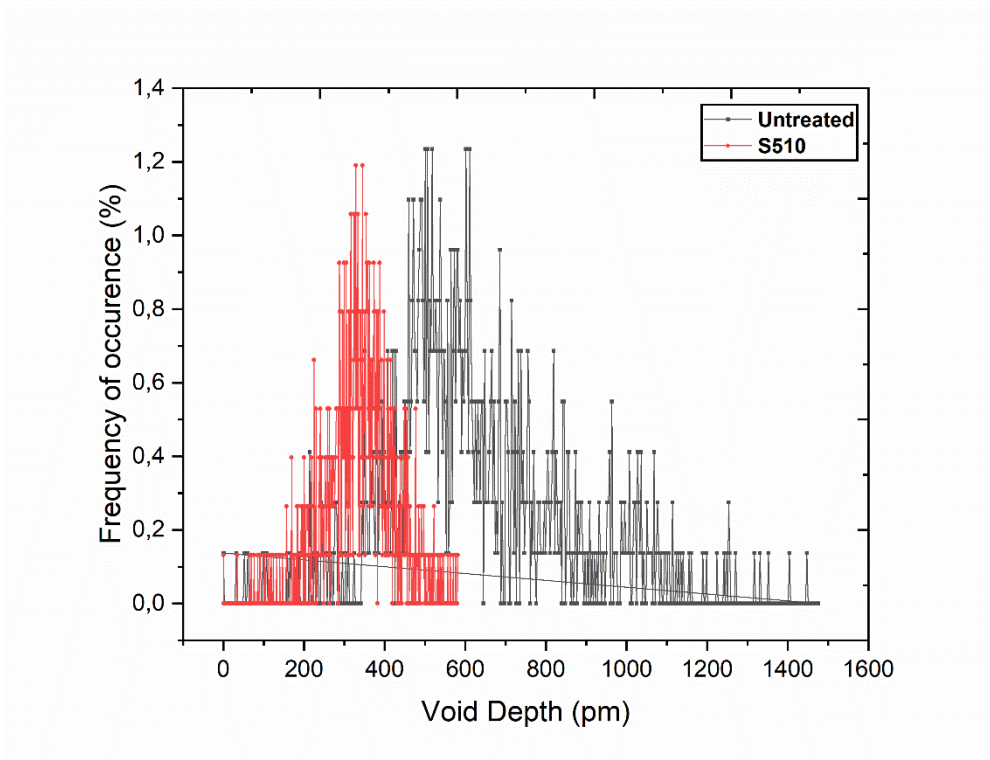


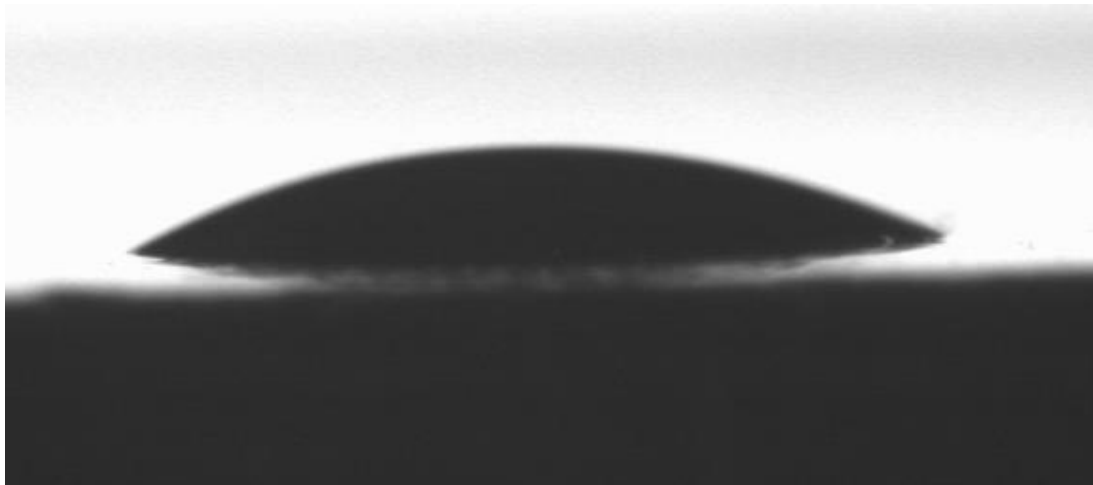
Figure 3.18 Comparative histogram representation of the distribution of void depths within the surface network of untreated and steam-treated specimens (S510)

The distribution of the void depths at the top surface that corresponded to approximately two silicate layers is represented by a histogram. The maxima of the frequency of void depths were centered around 600 pm in the untreated surface [137] in contrast to approximately 350 pm after superheated steam treatment. The lower void depth of the steam-treated surface is proposed to be associated with the presence of entrapped water molecules within the voids of the silica tetrahedral units, as evidenced by the ATR-IR spectral investigations in Section 3.2.1. These interstitial voids within the silicate network mark the availability of a directional pathway for the propagation of a crack tip through the depth of the glass network [138].

The alteration in surface topography together with the role of surface silanol groups enticed the characterization of the surface wettability. The following section presents the influence on the wetting behavior of water caused by superheated steam.

3.4 Alteration in surface wettability

The wetting characteristics of the glass surface were characterized with respect to the static contact angle of water. The measurements were performed in an ambient laboratory atmosphere with temperature around 25 °C and relative humidity of 60-65%. Figure 3.19 shows the comparative spread of a 2.5 μL droplet of water on the SLS container glass before and after superheated steam treatment.



(a)



(b)

Figure 3.19 Static contact angle of water on (a) untreated (b) steam treated (S510) SLS container glass surface. Volume of water droplet: 2.5 μL

The contact angle on the untreated surface was around 32° (see Figure 3.19 (a)). The influence of superheated steam was evident to provoke rapid spreading of the water droplet on the surface (see Figure 3.19 (b)). The contact angle was nearly zero as the

droplet dynamically spread on the surface to lead to super hydrophilic characteristics. The SLS glass slide portrayed similar wetting characteristics. This behavior was attributed to the higher density of OH groups on the outermost surface [139, 140] in the form of different silanol groups (see Section 3.2.1). These Si-OH groups promoted the adsorption of molecular water by hydrogen-bonding to contribute to the adherence on the surface, associated with rapid spreading by the virtue of increased surface energy. The technological importance of the superhydrophilicity of the SLS container glass surface caused by superheated steam is discussed in Section 4.2.

The spectroscopic investigations of ATR-IR and XPS, together with the alteration in surface topography and wetting characteristics — provided a thorough insight on the structural modifications caused by superheated steam in the near-surface region to explain the changes in subsurface hardness and scratch resistance. However, any possible influence in the bulk structure of the silicate network couldn't be completely ruled out. This necessitated the investigation of the Q^n species in the bulk silicate network by solid-state ^{29}Si MAS NMR, as discussed in the following section.

3.5 Distribution of Q^n species in the bulk silicate network

The distribution of Q^n species in the overall silicate network was quantitatively determined by the isotropic chemical shift with respect to the standard reference of tetramethylsilane by solid-state ^{29}Si nuclear magnetic resonance spectroscopy. High-resolution spectra were obtained by spinning the SLS glass specimen in powder form at the magic angle of 54.74° ($3\cos^2\theta - 1 = 0$) with respect to the static magnetic field of 7.05T at a frequency of 10 kHz. This enabled to average the anisotropy of nuclear interactions, thus preventing the loss of spectral resolution (peak-broadening) [141]. The individual Q^n species were determined by locating the overlapping peaks in the curve-fitted spectra. The shoulder peak corresponding to a chemical shift centered around -107 ppm indicates Q^4 species, while the major broad peak centered around -93 ppm corresponds to Q^3 species [7, 8]. The MAS NMR spectral fits of both the categories of SLS glasses were analyzed before and after steam-treatment to determine the changes in the concentration of Q^n species by the normalized integrated peak areas. The spectral fits of untreated and steam-treated container SLS glass are shown in Figure 3.20 (a) and (b), respectively. The untreated container SLS glass contained 84.8% Q^3 species and 15.2% Q^4 species. Sub- T_g

steam led to a conversion of 1.3% of Q^4 species into Q^3 species — indicative of a slight influence in the bulk silicate network by the virtue of overall silicate network depolymerization. Although the concentration of the change in Q^n species obtained by spectral fitting appears to be minor, it does support the evidence of subsurface network depolymerization discussed in section 3.2.2.

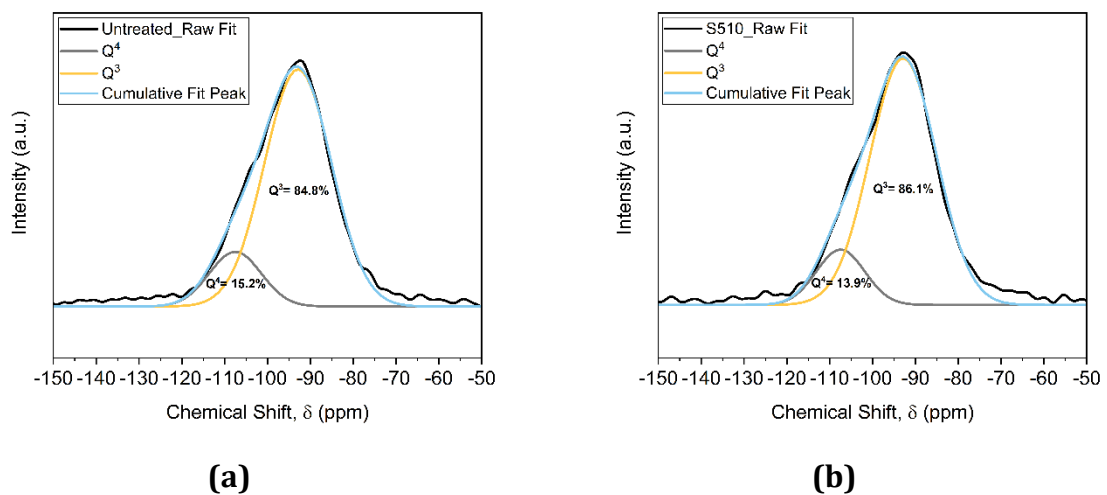
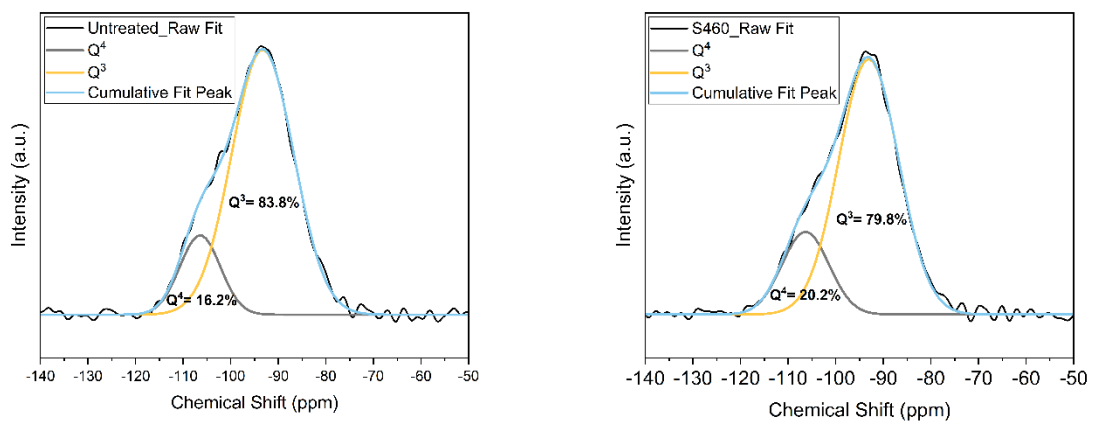


Figure 3.20 ^{29}Si MAS NMR spectral fits of (a) untreated and (b) sub- T_g steam-treated container SLS glass

The MAS NMR spectra of the untreated and steam-treated counterpart of the other category of SLS glass (glass slide) is shown in Figure 3.21.



(a)

(b)

Figure 3.21 ^{29}Si MAS NMR spectral fits of (a) untreated and (b) sub- T_g steam treated SLS glass slide

The untreated glass slide contained 83.8% Q^3 species and 16.2% Q^4 species. Sub- T_g steam treatment resulted in an increase in Q^4 species by 4% at the expense of Q^3 species. The conversion of Q^3 to Q^4 is characteristic of slight repolymerization of the bulk silicate network. This corroborates the evidence of subsurface network repolymerization, discussed in section 3.2.2. Thus, the NMR results signify slight rearrangement of the silicate network in the bulk of the glass structure caused by superheated steam. The trend of the network rearrangement of the bulk structure followed the suit of the near-surface region.

The modification of the surface and the bulk silicate structure caused by superheated steam has received considerable attention in this work, thus far. It has been clearly established and correlated with the changes in mechanical properties. However, there remains an open question if the described changes in the near-surface region are everlasting, considering the vulnerability of the glass surface to atmospheric corrosion discussed in Chapter 1, Section 1.3. This necessitated re-investigation of the steam-treated surface after subjecting it to ageing in ambient atmosphere, that forms the basis of discussion of the following section.

3.6 Effect of ageing in ambient atmosphere

The steam-treated glass surfaces were exposed to ambient laboratory atmosphere at an approximate temperature of 25°C and relative humidity in the range of 60-65%. The surfaces were investigated again after 1 week of ageing in the laboratory. The speculation of the steam-treated glass surface to be susceptible to atmospheric degradation proved to be true. The subsurface hardness of the container SLS glass was found to diminish with time, indicative of the transient nature of the fruitful effect caused by superheated steam. However, the steam treated SLS glass slide surface almost remained unaffected with ageing. The evolution of the subsurface hardness of the SLS glasses is shown in Figure 3.22.

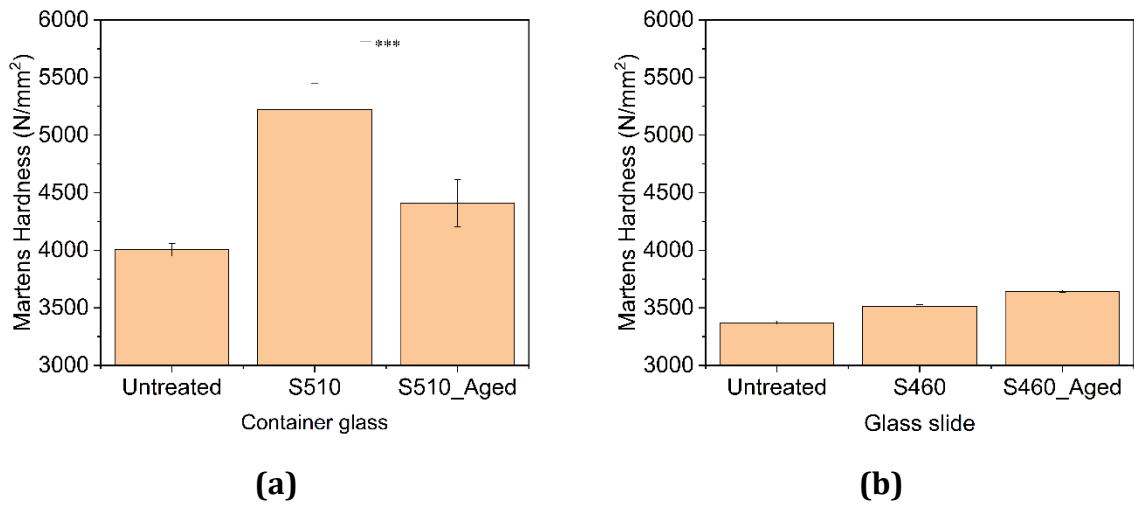


Figure 3.22 Evolution of subsurface hardness with ageing in ambient atmosphere (a) container glass (b) glass slide. Applied load: 10 mN. ANOVA single factor test: $p < 0.001$: ***

The noteworthy observation in Figure 3.22 is the vulnerability of the container SLS glass to ageing in ambient atmosphere with respect to a decrease in hardness of the steam-treated surface. This decrease was statistically significant with ANOVA test yielding a p-value less than 0.001, represented by three asterisks in Figure 3.22 (a). The influence on the subsurface silicate network that defines the susceptibility of the container SLS glass to ageing was studied by XPS accompanied by Ar⁺ sputtering, as illustrated in Figure 3.23.

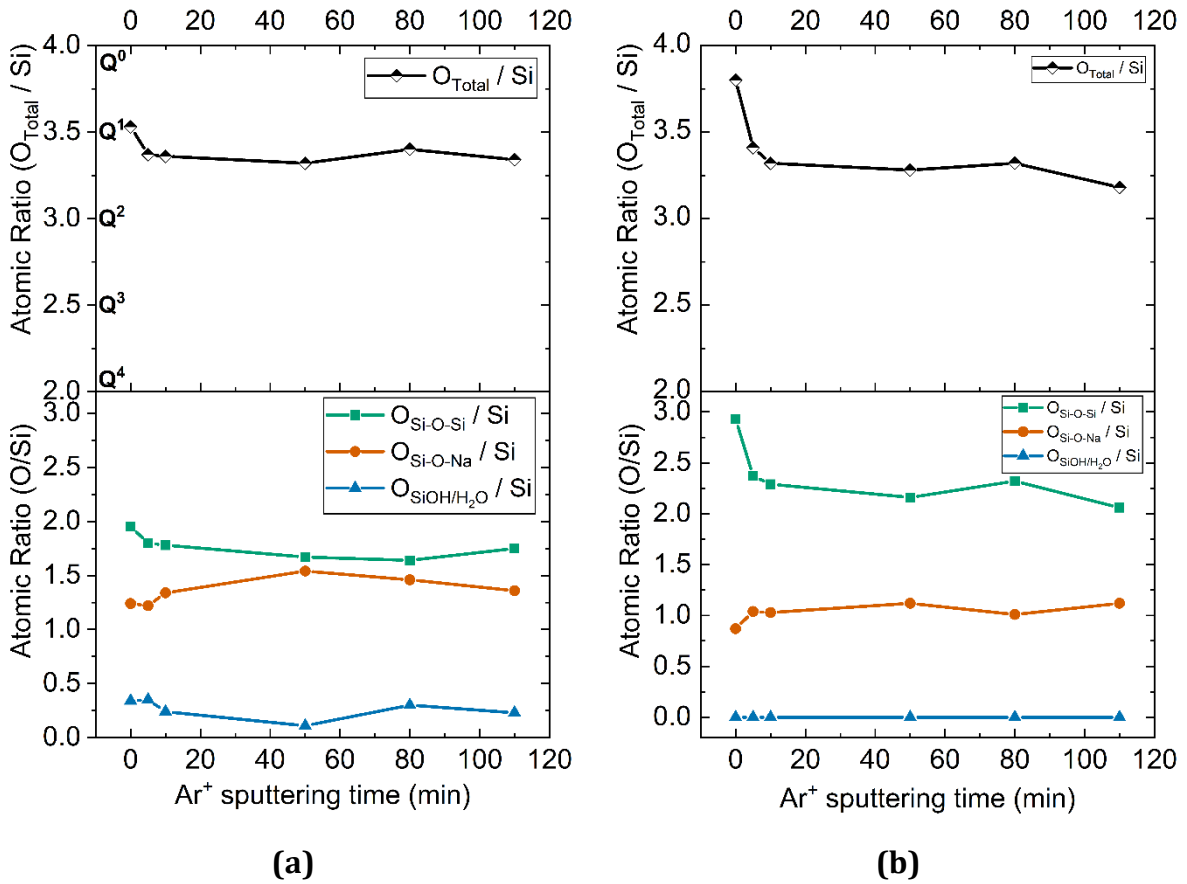
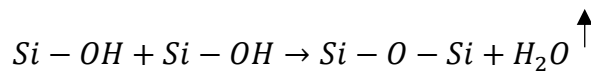


Figure 3.23 Variation of the atomic ratio of individual oxygen speciations to silicon, as a function of Ar⁺ sputtering time (below); variation of atomic ratio of total oxygen (sum of individual contributions) to silicon, as a function of Ar⁺ sputtering time (above) (a) steam-treated container glass surface (S510) (b) steam-treated container glass surface after 1 week of ageing in ambient atmosphere. Connecting lines act as a guideline to the eyes

The atomic ratio of O_{Si-O-Si} / Si of the aged glass surface increased at the expense of O_{SiOH/H₂O} / Si throughout the depth of sputtering. Furthermore, there was no contribution of O_{SiOH/H₂O} / Si to O_{Total}/ Si after ageing. This essentially signified the condensation of vicinal hydroxyls (adjacent silanol groups) to form bridging oxygens according to the following reaction:



The activation energy of the above reaction at room temperature is around 40 kJ/mol [142, 143]. The observed behavior of the rearrangement of the vicinal silanol groups to form bridging oxygens accompanied by the loss of weakly hydrogen-bonded water

molecules within the interstitial voids was a consequence of surface structural relaxation after steam-treatment during ageing [20]. The change in mass of the glass specimens as a result was negligible. The following two propositions are suggested with regard to the disappearance of the water molecules during ageing in ambient atmosphere:

- (a) The water molecules from the near-surface region could either escape to the outer atmosphere, and/or
- (b) Percolate and dissipate into the bulk of the glass network

Neither of these possibilities can be ruled out. The occurrence of the former event may be restricted by depositing a thin film coating on the glass surface. The latter case personifies a natural phenomenon that may not be evitable. The exposure of the voids resulting in free volume within the silicate network after the disappearance of the water molecules is analogous to the untreated surface. This explains the degradation in hardness of the container SLS glass with ageing in ambient atmosphere.

On the other hand, the relative absence of entrapped water molecules within the silicate network of the steam treated SLS glass slide (S460) ruled out the surface degradation phenomenon associated with deterioration of hardness in this variant of SLS glass. The slight increment in hardness after sub- T_g steam-treatment was retained after ageing, as shown in Figure 3.22 (b).

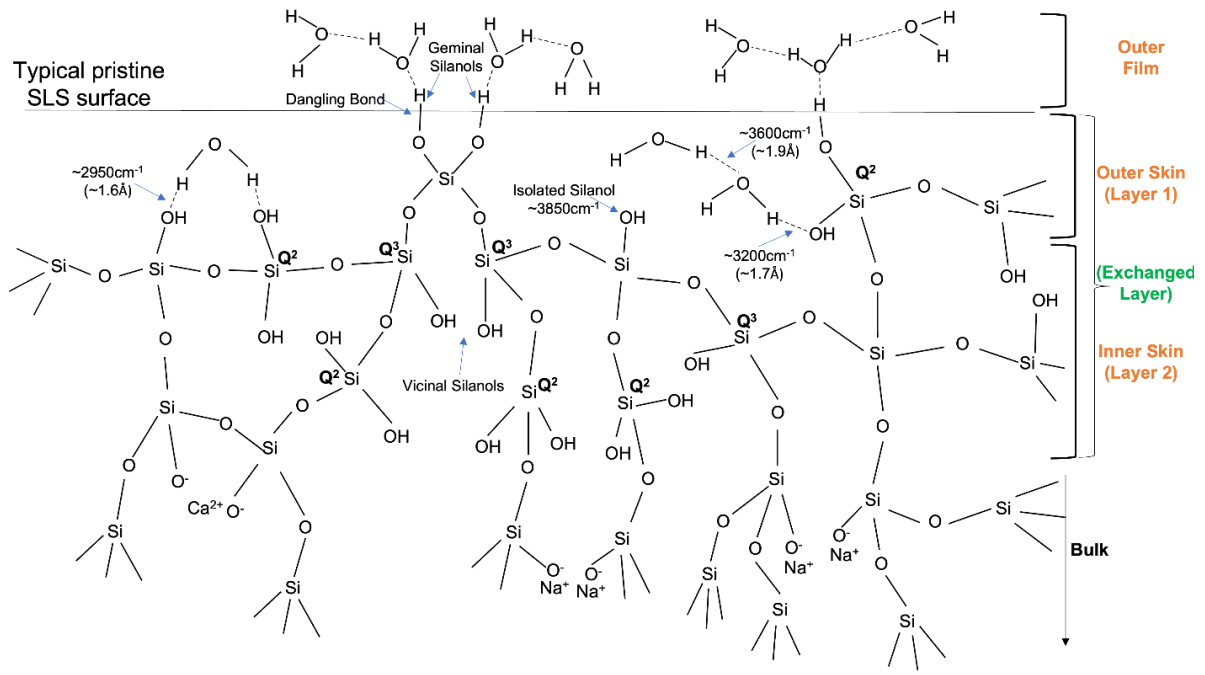
It is noteworthy to mention that the ageing of the S510 surface in ambient atmosphere did not have any influence on the alteration of its superhydrophilic characteristics (see section 3.4). This is because the OH groups on the surface that contribute to the adsorption of the water molecules would persist due to its tendency of reforming back when exposed to air [139].

Sections 3.1 through 3.4 demonstrated the influence of superheated steam on the surface structural and mechanical properties. Additionally, the susceptibility of the steam-treated surface to ageing was described in this section. Having gained a thorough insight of the surface structural changes, it was essential to schematically represent the surface structural modification caused by superheated steam to attract the reader's attention from a pictorial perspective. This is illustrated in the following section.

3.7 Surface structural schematics

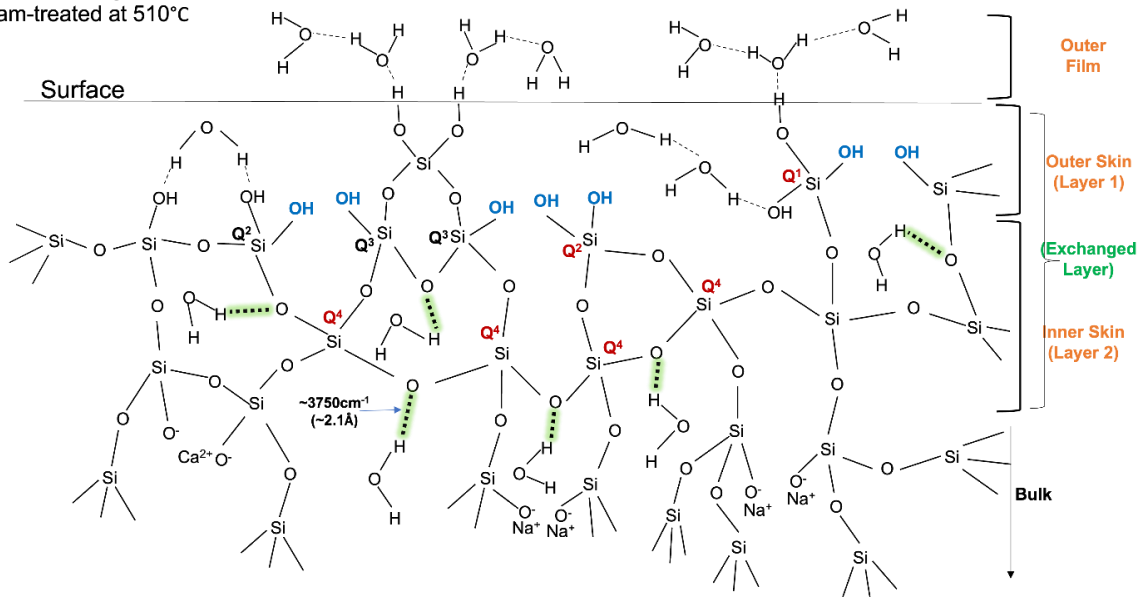
The surface structure was schematized based on the evidence of the role of surface hydroxyl groups and silicate network connectivity, obtained by complementary characterizations discussed in the preceding sections.

The surface structure of a typical untreated soda-lime-silica glass is schematically represented in Figure 3.24 (a). The different surface hydroxyl groups were assigned corresponding to the ATR-IR OH stretching vibrations, discussed in section 3.2.1. The “outer film” consists of physisorbed and chemisorbed water molecules adsorbed from the ambient atmosphere by ubiquitous interaction with atmospheric humidity. The “exchanged layer” in the near-surface region is an SiO₂-rich skin with a thickness on the order of few nanometers. It was formed by the volatilization of the mobile sodium ions during production and subsequent handling and storage [144, 145]. This region consists of different forms of silanol groups, as discussed in Chapter 1, Section 1.2.1. This sodium depleted exchanged layer is further divided into two layers: “outer skin (layer 1)” and “inner skin (layer 2)”. The outer skin has a reversible behavior with respect to the adsorption of water molecules to the silanol groups by incessant interaction with ambient atmosphere. The inner skin contains vicinal silanols (adjacent silanol groups) that are reactive during steam treatment. The schematic representation of the surface structures of steam-treated container glass and glass slide are schematically represented in Figure 3.24 (b) and 3.24 (c), respectively.



(a)

SLS container glass surface steam-treated at 510°C



(b)

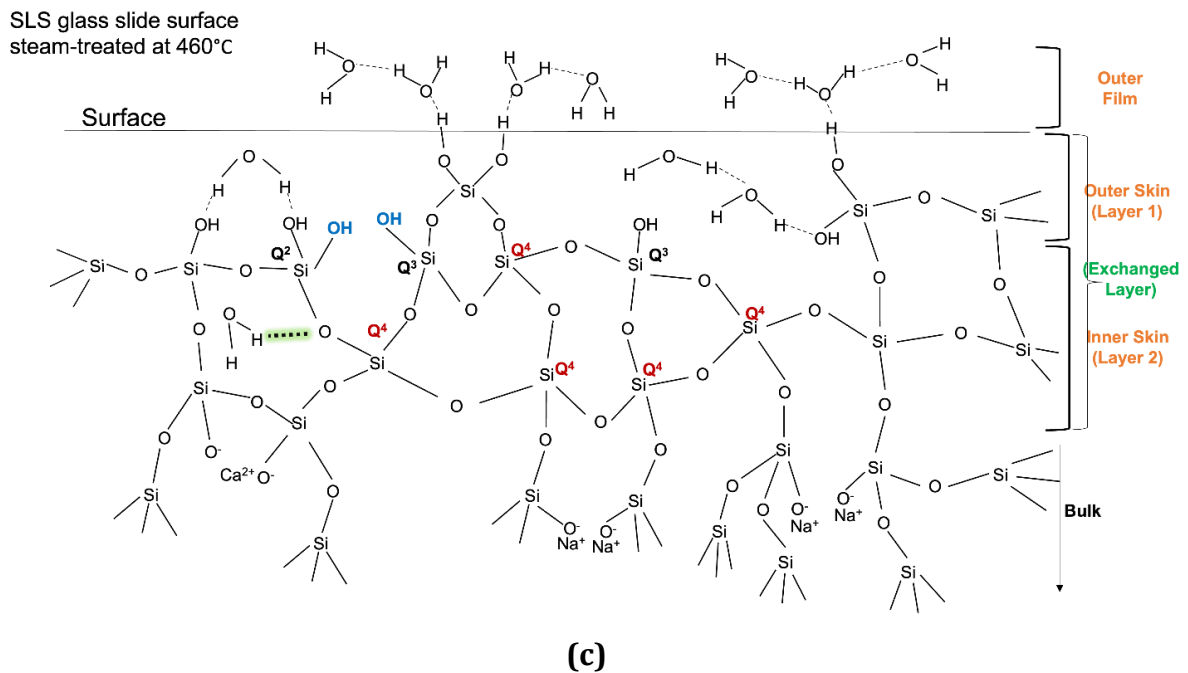


Figure 3.24 Surface structural schematic representation of **(a)** untreated **(b)** sub- T_g steam-treated container glass **(c)** sub- T_g steam treated glass slide

The inner skin (layer 2) containing vicinal silanols underwent condensation to repolymerize into bridging oxygens with silica tetrahedral units containing Q^4 species, during steam-treatment. The altered Q^n notations are highlighted in brown. The surface network of the outer skin of the container SLS glass depolymerized to form silanol groups associated with NBOs (highlighted in blue), as described in Section 3.2.2. This created a micro channelized pathway to facilitate the diffusion of water molecules to occupy the interstitial voids within the silica tetrahedral network. The weakly hydrogen-bonded water molecules corresponding to the OH stretching vibration centered around 3750 cm^{-1} in ATR-IR spectra (see section 3.2.1) are highlighted in green. On the contrary, the evidence of silicate network depolymerization in the near-surface region of the glass slide meant an increase in the population of BOs in the inner skin with more Q^4 units in Figure 3.24(c). This closed network inhibited the diffusion of water molecules into the interstitial voids. The suppression of the stuffing effect of the voids by molecular water reflects a mere increase of 4% in subsurface hardness of the microscopic glass slide, as opposed to a 30% enhancement in hardness of the container glass surface. The susceptibility of the container glass surface to ageing in ambient atmosphere may be associated with the loss of these entrapped water molecules through the outer skin (layer 1) to the outer atmosphere. This was caused by the promotion of surface structural relaxation by

molecular water [20] after its interaction with superheated steam. The relative absence of these entrapped water molecules within the silica tetrahedral network of the SLS glass slide prevented the degradation of subsurface hardness with ageing in ambient atmosphere.

4 Conclusion and Outlook

This chapter is divided into two sections. Section 4.1 presents a summary of this research, together with a concluding remark of the principal output. Section 4.2 is intended to act as a source of motivation for further research based on the output of this work.

4.1 Conclusion

This research was focused on establishing a fundamental relationship between the surface structural and mechanical properties of soda-lime-silica glass. Superheated steam was considered as a medium of interaction with the glass surface to study the modification in surface structural network in correlation with the influence on mechanical properties such as subsurface hardness. Two different categories of SLS glasses were chosen for a comparative study — container glass and glass slide. These glasses were manufactured by different processes with slightly different modifier concentrations and glass transition temperatures (T_g) were considered. The container SLS glass had a higher T_g in the range of 560 °C to 575 °C, while the microscopic SLS glass slide had a relatively lower T_g in the range of 510 °C to 540 °C. The process conditions of steam treatment to induce an optimum network mobility in the glass structure for a distinguishable alteration in surface mechanical and structural properties was determined to be 50 °C below the onset of T_g for a duration of 30 minutes at a flow rate of 3 kg/hr. Accordingly, the container SLS glass surface was treated at 510 °C and the glass slide was treated at 460 °C for 30 minutes followed by mechanical and structural characterizations. The hardness of the container glass surface was enhanced by 30% up to a depth of 300 nm below the glass surface, in contrast to a marginal increase of 4% in the latter. The surface hydroxyl groups were characterized by ATR-IR spectroscopy, which revealed the presence of hydrogen-bonded water molecules entrapped within the interstitial voids of the silica tetrahedral network. The concentration of these water molecules was higher in the container glass surface, dictated by an increased intensity of absorbance of the OH stretching peak centered around 3750 cm^{-1} . The reduction in void depths among the first monolayers within the silicate network evidenced by atomic force microscopy corroborated the presence of entrapped water molecules within the interstitial voids after steam-treatment. Having studied the role of the silanol groups, it was essential to investigate any possible network rearrangement that occurred during steam treatment to facilitate the diffusion of the water molecules.

The subsurface silicate network connectivity of the SLS glasses was studied by X-ray photoelectron spectroscopic investigations accompanied by Ar⁺ sputtering. The concentrations of the individual oxygen speciations of bridging oxygen (BO: O_{Si-O-Si}), non-bridging oxygen (NBO: O_{Si-O-Na}) and hydrous species (O_{SiOH/H₂O}) were calculated by Gaussian-Lorentzian curve-fittings of O1s spectral lines. The atomic ratios of each oxygen speciation to silicon were plotted as a function of Ar⁺ sputtering time to determine the silicate network connectivity of the near-surface region up to a depth of approximately 110 nm below the glass surface. The as-received container SLS glass surface had a higher concentration of mechanically weakening species associated with NBOs, while the surface of the as-received glass slide was more rigid with relatively higher concentration of BOs. Sub-T_g steam treatment led to an increase in the atomic ratio of total oxygen to silicon (O_{Total}/Si) in both the SLS glasses. This was correlated to the scratch resistance of the glass surface. It was observed that the visibility of the scratches on the container SLS glass increased after sub-T_g heat and steam treatments. From the structural viewpoint, the increased vulnerability of the glass surface to scratch formation in the micro-abrasive regime was attributed to an increase in the atomic ratio of total oxygen to silicon (O_{Total}/Si) in the region between 5 and 100 nm below the glass surface.

The contribution of the different oxygen species that led to the total increase in O_{Total}/Si in the two categories of glasses varied. The proportion of increase in NBO contribution exceeded the increase in BO contribution to O_{Total}/Si in the near-surface region of container glass, that indicated surface network depolymerization caused by superheated steam. On the other hand, the increase in BO dominated over the increase in NBO contribution to the total increase in oxygen to silicon atomic ratio in the subsurface network of microscopic glass slide. This essentially signified surface network repolymerization. This finding was corroborated by the ²⁹Si MAS NMR results of the distribution of Qⁿ species in the overall silicate structure including the bulk network. There was a slight increase of 1.3% Q³ species at the expense of Q⁴ in the silicate structure of the container glass that signified a slight decrease in network connectivity (depolymerization). On the contrary, the concentration of Q⁴ species increased by 4% at the expense of Q³ species in the bulk silicate structure of the glass slide. This behavior served as evidence of a slight network rearrangement in the bulk silicate network as well. The differences in network rearrangement in the two glasses were attributed to the differences in the network connectivity of the pristine surfaces. The container SLS glass

with a weaker initial network favored depolymerization when subjected to the interaction with superheated steam. This facilitated the diffusion of water molecules to occupy the interstitial voids to contribute to subsurface hardening. On the other hand, the glass slide with higher concentration of BOs in the as-received state underwent repolymerization during steam treatment that inhibited the diffusion of water molecules into the network.

One of the striking discoveries was the susceptibility of the steam-treated surface to ageing in ambient atmosphere. The subsurface hardness of the container glass degraded after one week of ageing. This behavior was associated with the loss of the entrapped water molecules within the interstitial voids by the virtue of condensation of vicinal silanol groups to form bridging oxygens. This network rearrangement was promoted by surface structural relaxation facilitated by the entrapped molecular water in the steam-treated surface network. However, the glass slide was seemingly unaffected by ageing due to the relative absence of water molecules within the silicate network after its interaction with superheated steam.

The surface structural representations of the untreated and steam treated SLS glasses were schematized based on the experimental evidence of surface hydroxyl species and silicate network connectivity. The surface network depolymerization in container glass opened up a micro-channelized pathway for the diffusion of water molecules to occupy the interstitial voids within the silica tetrahedral network to contribute to subsurface hardening. In contrast, the dominance of surface network repolymerization in microscopic glass slide meant lower availability of diffusion pathways for water molecules during superheated steam treatment. The relatively lower concentration of hydrogen-bonded water molecules within the interstitial voids was accountable for higher availability of free volume within the silicate network with a marginal rise in hardness in the latter. Overall, the two types of SLS glasses considered in this study underwent different structural rearrangements during superheated steam treatment, that explained the observed differences in subsurface hardness of the glasses.

Concluding remark

To sum it up, the relationship between the subsurface hardness and structural network of SLS glass was established. The extent of silicate network connectivity together with the interstitial voids within the silica tetrahedral units play a decisive role in governing the near-surface mechanical properties. The evidence of the enhancement in subsurface hardness due to the stuffing of the interstitial voids by hydrogen-bonded molecular water caused by superheated steam was indicative of the detrimental effect of these voids on the directional propagation of a crack front through the depth of the glass network. Furthermore, the promotion of surface structural relaxation caused by the water molecules during ageing was the underlying cause of the vulnerability of the steam-treated glass surface to atmospheric corrosion. These evidences support the invincible tendency of the glass surface network to undergo rearrangement in response to any external stimulus, that essentially governs the overall performance of the material.

4.2 Outlook

The output of this research may be considered as the basis of the following possibilities:

- A. Subsurface hardening of soda-lime-silica glass by superheated steam in the vicinity of the glass transition temperature. The effect of degradation of hardness with ageing may be prevented by depositing a thin film coating on the glass surface (e.g., alumina thin film). This is expected to additionally contribute to strengthening of the glass by preventing the direct exposure of the surface flaws.
- B. Promotion of superhydrophilicity of the glass surface by superheated steam. The technological importance of the alteration in surface wettability has been clarified. The steam-treated surface proved to be effective in promoting the adherence of a cold-end coating. The coating material “x-glas® KR 1002” with a high-water content as a solvent was developed by “Wiegand-Glas”. The objective was to replace the standard hot/cold end coatings to improve the scratch resistance of the glass surface by a one-step process that was environment friendly. Further investigations are in progress in the industry. The rapid spreading of the coating material was facilitated on the steam-treated surface in comparison to the pristine surface. This was due to the high surface energy of the superhydrophilic surface after its interaction with superheated steam.
- C. Although strengthening of silicate glass has been recently reported by superheated steam [146] by developing a compressive stress profile with a layer containing hydrogen species, the composition of the glass plays a critical role for the process to succeed. The combination of phosphorus and an alkali ion with low cationic field strength, potassium, played a significant role in promoting the ion-exchange process for enhanced strengthening. Thus, the SLS glasses used in this study with relatively high sodium concentration instead of potassium, did not exhibit any strengthening by the influence of superheated steam (see Appendix A2) due to the absence of any ion-exchange reaction. As a future work, the effect of composition on the structural changes in the surface and the bulk network caused by superheated steam may be thoroughly investigated with an objective of further enhancing the strength of the glass.

References

- [1] J. E. Shelby, *Introduction to Glass Science and Technology*, The Royal Society of Chemistry, 2021.
- [2] A.K. Varsheneya, in *Fundamentals of Inorganic Glasses*, Elsevier, 2019, p. iv.
- [3] R. Youngman, "NMR Spectroscopy in Glass Science: A Review of the Elements," *Materials*, vol. 11, p. 476, March 2018.
- [4] R. Dupree, D. Holland, P. W. McMillan and R. F. Pettifer, "The structure of soda-silica glasses: A mas NMR study," *Journal of Non-Crystalline Solids*, vol. 68, p. 399–410, November 1984.
- [5] H. Maekawa, T. Maekawa, K. Kawamura and T. Yokokawa, "The structural groups of alkali silicate glasses determined from ^{29}Si MAS-NMR," *Journal of Non-Crystalline Solids*, vol. 127, p. 53–64, January 1991.
- [6] J. F. Stebbins, "Identification of multiple structural species in silicate glasses by ^{29}Si NMR," *Nature*, vol. 330, p. 465–467, December 1987.
- [7] H. W. Nesbitt, G. M. Bancroft, G. S. Henderson, R. Ho, K. N. Dalby, Y. Huang and Z. Yan, "Bridging, non-bridging and free (O^{2-}) oxygen in $\text{Na}_2\text{O-SiO}_2$ glasses: An X-ray Photoelectron Spectroscopic (XPS) and Nuclear Magnetic Resonance (NMR) study," *Journal of Non-Crystalline Solids*, vol. 357, p. 170–180, January 2011.
- [8] A. R. Jones, R. Winter, G. N. Greaves and I. H. Smith, "MAS NMR study of soda-lime–silicate glasses with variable degree of polymerisation," *Journal of Non-Crystalline Solids*, Vols. 293-295, p. 87–92, November 2001.
- [9] R. M. Almeida and L. F. Santos, "Raman Spectroscopy of Glasses," in *Modern Glass Characterization*, John Wiley & Sons, Inc., 2015, p. 1–33.
- [10] T. Furukawa, K. E. Fox and W. B. White, "Raman spectroscopic investigation of the structure of silicate glasses. III. Raman intensities and structural units in sodium silicate glasses," *The Journal of Chemical Physics*, vol. 75, p. 3226–3237, October 1981.
- [11] L. Robinet, C. Coupry, K. Eremin and C. Hall, "Raman investigation of the structural changes during alteration of historic glasses by organic pollutants," *Journal of Raman Spectroscopy*, vol. 37, p. 1278–1286, 2006.
- [12] C. Calahoo, J. W. Zwanziger and I. S. Butler, "Mechanical–Structural Investigation of Ion-Exchanged Lithium Silicate Glass using Micro-Raman Spectroscopy," *The Journal of Physical Chemistry C*, vol. 120, p. 7213–7232, March 2016.
- [13] N. Terakado, S. Uchida, Y. Takahashi, T. Fujiwara and M. Arakawa, "Depth analysis of a compression layer in chemically strengthened glass using depth-resolved micro-Raman spectroscopy," *Journal of the Ceramic Society of Japan*, vol. 124, p. 1164–1166, 2016.
- [14] F. Adar, E. Lee, S. Mamedov and A. Whitley, "Experimental Evaluation of the Depth Resolution of a Raman Microscope," *Microscopy and Microanalysis*, vol. 16, p. 360–361, July 2010.

- [15] P. Colomban, A. Tournie and L. Bellot-Gurlet, "Raman identification of glassy silicates used in ceramics, glass and jewellery: a tentative differentiation guide," *Journal of Raman Spectroscopy*, vol. 37, p. 841–852, 2006.
- [16] R. H. Doremus, *Glass Science*, Wiley, 1994.
- [17] J. Banerjee, V. Bojan, C. G. Pantano and S. H. Kim, "Effect of heat treatment on the surface chemical structure of glass: Oxygen speciation from in situ XPS analysis," *Journal of the American Ceramic Society*, vol. 101, pp. 644-656, 2018.
- [18] S.-i. Amma, S. H. Kim and C. G. Pantano, "Analysis of Water and Hydroxyl Species in Soda Lime Glass Surfaces Using Attenuated Total Reflection (ATR)-IR Spectroscopy," *Journal of the American Ceramic Society*, vol. 99, pp. 128-134, 2016.
- [19] A. Stuke, H. Behrens, B. C. Schmidt and R. Dupree, "H₂O speciation in float glass and soda lime silica glass," *Chemical Geology*, vol. 229, p. 64–77, May 2006.
- [20] M. Tomozawa, D.-L. Kim, A. Agarwal and K. M. Davis, "Water diffusion and surface structural relaxation of silica glasses," *Journal of Non-Crystalline Solids*, vol. 288, p. 73–80, August 2001.
- [21] G. Soraru, R. Dal Maschio and G. Della Mea, "Correlation between surface modifications and resistance to the formation of radial cracks in soda-lime glass," *Glass technology*, vol. 27, p. 69–71, 1986.
- [22] L. C. Bradley, Z. R. Dilworth, A. L. Barnette, E. Hsiao, A. J. Barthel, C. G. Pantano and S. H. Kim, "Hydronium Ions in Soda-lime Silicate Glass Surfaces," *Journal of the American Ceramic Society*, vol. 96, p. 458–463, December 2012.
- [23] N. D. Surdyka, C. G. Pantano and S. H. Kim, "Environmental effects on initiation and propagation of surface defects on silicate glasses: scratch and fracture toughness study," *Applied Physics A*, vol. 116, p. 519–528, June 2014.
- [24] H. He, L. Qian, C. G. Pantano and S. H. Kim, "Mechanochemical Wear of Soda Lime Silica Glass in Humid Environments," *Journal of the American Ceramic Society*, vol. 97, p. 2061–2068, June 2014.
- [25] J. H. Seaman, P. J. Lezzi, T. A. Blanchet and M. Tomozawa, "Degradation of ion-exchange strengthened glasses due to surface stress relaxation," *Journal of Non-Crystalline Solids*, vol. 403, pp. 113-123, 2014.
- [26] Hair Michael L., "Hydroxyl groups on silica surface," in *Glass Surfaces*, Elsevier, 1975, p. 299–309.
- [27] A. M. Efimov, V. G. Pogareva and A. V. Shashkin, "Water-related bands in the IR absorption spectra of silicate glasses," *Journal of Non-Crystalline Solids*, vol. 332, p. 93–114, December 2003.
- [28] G. Navarra, I. Iliopoulos, V. Militello, S. G. Rotolo and M. Leone, "OH-related infrared absorption bands in oxide glasses," *Journal of Non-Crystalline Solids*, vol. 351, p. 1796–1800, July 2005.

- [29] S.-i. Amma, J. Luo, S. H. Kim and C. G. Pantano, "Effects of fictive temperature on the leaching of soda lime silica glass surfaces," *Journal of the American Ceramic Society*, vol. 100, p. 1424–1431, February 2017.
- [30] J. Luo, H. Huynh, C. G. Pantano and S. H. Kim, "Hydrothermal reactions of soda lime silica glass – Revealing subsurface damage and alteration of mechanical properties and chemical structure of glass surfaces," *Journal of Non-Crystalline Solids*, vol. 452, pp. 93–101, 2016.
- [31] D. Ngo, H. Liu, Z. Chen, H. Kaya, T. J. Zimudzi, S. Gin, T. Mahadevan, J. Du and S. H. Kim, "Hydrogen bonding interactions of H₂O and SiOH on a boroaluminosilicate glass corroded in aqueous solution," *npj Materials Degradation*, vol. 4, January 2020.
- [32] T. Uchino, T. Sakka and M. Iwasaki, "Interpretation of Hydrated States of Sodium Silicate Glasses by Infrared and Raman Analysis," *Journal of the American Ceramic Society*, vol. 74, p. 306–313, February 1991.
- [33] S.-i. Amma, J. Luo, C. G. Pantano and S. H. Kim, "Specular reflectance (SR) and attenuated total reflectance (ATR) infrared (IR) spectroscopy of transparent flat glass surfaces: A case study for soda lime float glass," *Journal of Non-Crystalline Solids*, vol. 428, p. 189–196, November 2015.
- [34] M. Rubin, "Optical properties of soda lime silica glasses," *Solar Energy Materials*, vol. 12, p. 275–288, September 1985.
- [35] E. Tyrode, M. W. Rutland and C. D. Bain, "Adsorption of CTAB on Hydrophilic Silica Studied by Linear and Nonlinear Optical Spectroscopy," *Journal of the American Chemical Society*, vol. 130, pp. 17434–17445, 2008.
- [36] E. Libowitzky, "Correlation of O-H stretching frequencies and O-H...O hydrogen bond lengths in minerals," *Monatshefte für Chemie / Chemical Monthly*, vol. 130, p. 1047–1059, August 1999.
- [37] H.-W. Wang, M. J. DelloStritto, N. Kumar, A. I. Kolesnikov, P. R. C. Kent, J. D. Kubicki, D. J. Wesolowski and J. O. Sofo, "Vibrational Density of States of Strongly H-Bonded Interfacial Water: Insights from Inelastic Neutron Scattering and Theory," *The Journal of Physical Chemistry C*, vol. 118, p. 10805–10813, May 2014.
- [38] S. Nihonyanagi, J. A. Mondal, S. Yamaguchi and T. Tahara, "Structure and Dynamics of Interfacial Water Studied by Heterodyne-Detected Vibrational Sum-Frequency Generation," *Annual Review of Physical Chemistry*, vol. 64, p. 579–603, April 2013.
- [39] H.-F. Wang, L. Velarde, W. Gan and L. Fu, "Quantitative Sum-Frequency Generation Vibrational Spectroscopy of Molecular Surfaces and Interfaces: Lineshape, Polarization, and Orientation," *Annual Review of Physical Chemistry*, vol. 66, p. 189–216, April 2015.
- [40] C. Wang, W. Häfner, G. Krausch, E. Rädlein, S. Tratzky, M. Schramm and K.-P. Martinek, "Study of surface changes on industrial glasses with AFM, FE-SEM, EDX, SNMS and LM. Part 1 Glass skin and corrosion," *Glass Science and Technology -Frankfurt am Main-*, vol. 77 (2004), pp. 103–110, June 2004.

- [41] L. W. Hobbs, "Network topology in aperiodic networks," *Journal of Non-Crystalline Solids*, Vols. 192-193, pp. 79-91, 1995.
- [42] D. L. Griscom, "Defect structure of glasses," *Journal of Non-Crystalline Solids*, vol. 73, p. 51-77, August 1985.
- [43] B. C. Bunker, "Molecular mechanisms for corrosion of silica and silicate glasses," *Journal of Non-Crystalline Solids*, vol. 179, pp. 300-308, 1994.
- [44] M. M. C. Carter, N. S. McIntyre, H. W. King and A. R. Pratt, "The aging of silicate glass surfaces in humid air," *Journal of Non-Crystalline Solids*, vol. 220, p. 127-138, November 1997.
- [45] G. Pintori and E. Cattaruzza, "XPS/ESCA on glass surfaces: A useful tool for ancient and modern materials," *Optical Materials: X*, vol. 13, p. 100108, January 2022.
- [46] A. Einstein, "Über einen die Erzeugung und Verwandlung des Lichtes betreffenden heuristischen Gesichtspunkt," *Annalen der Physik*, vol. 322, p. 132-148, 1905.
- [47] P. van der Heide, "X-ray Photoelectron Spectroscopy: An introduction to Principles and Practices," 2011.
- [48] V. Sharma, Spectroscopic ellipsometry for the in-situ investigation of atomic layer depositions, Dresden: Sächsische Landesbibliothek – Staats- und Universitätsbibliothek Dresden (SLUB), 2014.
- [49] C. Powell, *X-ray Photoelectron Spectroscopy Database XPS, Version 4.1, NIST Standard Reference Database 20*, National Institute of Standards and Technology, 1989.
- [50] Physical Electronics, Inc. (PHI) , 2023. [Online]. Available: <https://www.phis.com/surface-analysis-techniques/xps-esca.html>.
- [51] Y. Yamamoto and K. Yamamoto, "Ar ion damage on the surface of soda-lime-silica glass," *IOP Conference Series: Materials Science and Engineering*, vol. 18, p. 022005, March 2011.
- [52] Y. Yamamoto, "Precise XPS depth analysis of soda-lime-silica glass surface after various treatments," *Surface and Interface Analysis*, vol. 44, p. 931-933, January 2012.
- [53] Y. Yamamoto and K. Yamamoto, "Precise XPS depth profile of soda-lime-silica float glass using C60 ion beam," *Optical Materials*, vol. 33, p. 1927-1930, October 2011.
- [54] F.M. Ernsberger, "Detection of strength-impairing surface flaws in glass," *Proceedings of the Royal Society of London. Series A. Mathematical and Physical Sciences*, vol. 257, p. 213-223, September 1960.
- [55] A.A. Griffith, "VI. The phenomena of rupture and flow in solids," *Philosophical Transactions of the Royal Society of London. Series A, Containing Papers of a Mathematical or Physical Character*, vol. 221, p. 163-198, January 1921.
- [56] A. K. Varshneya, "Stronger glass products: Lessons learned and yet to be learned," *International Journal of Applied Glass Science*, vol. 9, p. 140-155, February 2018.
- [57] D. B. Marshall and B. R. Lawn, "Surface flaws in glass," 1983.

- [58] B. R. Lawn, B. J. Hockey and S. M. Wiederhorn, "Atomically sharp cracks in brittle solids: an electron microscopy study," *Journal of Materials Science*, vol. 15, p. 1207–1223, May 1980.
- [59] R. H. Doremus, "Modification of the Hillig-Charles theory for static fatigue of glass," *Engineering Fracture Mechanics*, vol. 13, p. 945–953, January 1980.
- [60] R. H. Doremus, "Fracture and Fatigue of Glass," in *Glass III - Treatise on Materials Science and Technology*, Elsevier, 1982, p. 169–239.
- [61] S. Ito and M Tomozawa, "Crack Blunting of High-Silica Glass," *Journal of the American Ceramic Society*, vol. 65, p. 368–371, August 1982.
- [62] B.R. Lawn and D. B. Marshall, "Hardness, Toughness, and Brittleness: An Indentation Analysis," *Journal of the American Ceramic Society*, vol. 62, p. 347–350, July 1979.
- [63] Y. Kato, H. Yamazaki, S. Yoshida and J. Matsuoka, "Effect of densification on crack initiation under Vickers indentation test," *Journal of Non-Crystalline Solids*, vol. 356, p. 1768–1773, August 2010.
- [64] Y. Kato, H. Yamazaki, S. Itakura, S. Yoshida and J. Matsuoka, "Load dependence of densification in glass during Vickers indentation test," *Journal of the Ceramic Society of Japan*, vol. 119, p. 110–115, 2011.
- [65] T. Haranoh, H. Ishikawa, N. Shinkai and M. Mizuhashi, "Crack evolution in Vickers indentation for soda-lime-silica glass," *Journal of Materials Science*, vol. 17, p. 1493–1500, May 1982.
- [66] S. Yoshida, J.-C. Sangleboeuf and T. Rouxel, "Indentation-induced densification of soda-lime silicate glass," *International Journal of Materials Research*, vol. 98, p. 360–364, May 2007.
- [67] A. Koike, S. Akiba, T. Sakagami, K. Hayashi and S. Ito, "Difference of cracking behavior due to Vickers indentation between physically and chemically tempered glasses," *Journal of Non-Crystalline Solids*, vol. 358, p. 3438–3444, December 2012.
- [68] F. M. Ernsberger, "Role of Densification in Deformation of Glasses Under Point Loading," *Journal of the American Ceramic Society*, vol. 51, p. 545–547, October 1968.
- [69] A. Arora, D. B. Marshall, B. R. Lawn and M. V. Swain, "Indentation deformation/fracture of normal and anomalous glasses," *Journal of Non-Crystalline Solids*, vol. 31, p. 415–428, April 1979.
- [70] A. Kailer, K. G. Nickel and Y. G. Gogotsi, "Raman microspectroscopy of nanocrystalline and amorphous phases in hardness indentations," *Journal of Raman Spectroscopy*, vol. 30, pp. 939-946, 1999.
- [71] R. F. Cook and G. M. Pharr, "Direct Observation and Analysis of Indentation Cracking in Glasses and Ceramics," *Journal of the American Ceramic Society*, vol. 73, p. 787–817, April 1990.

- [72] K. Januchta and M. M. Smedskjaer, "Indentation deformation in oxide glasses: Quantification, structural changes, and relation to cracking," *Journal of Non-Crystalline Solids: X*, vol. 1, p. 100007, March 2019.
- [73] T. Rouxel, H. Ji, J. P. Guin, F. Augereau and B. Rufflé, "Indentation deformation mechanism in glass: Densification versus shear flow," *Journal of Applied Physics*, vol. 107, p. 094903, May 2010.
- [74] S. Yoshida, J.-C. Sangleboeuf and T. Rouxel, "Quantitative evaluation of indentation-induced densification in glass," *Journal of Materials Research*, vol. 20, p. 3404–3412, December 2005.
- [75] W. Weiler, "The relationship between vickers hardness and universal hardness," *Plating and surface finishing*, vol. 79, p. 53–53, 1992.
- [76] C. Calahoo, X. Zhang and J. W. Zwanziger, "Nanoindentation Study of the Surface of Ion-Exchanged Lithium Silicate Glass," *The Journal of Physical Chemistry C*, vol. 120, p. 5585–5598, March 2016.
- [77] X. Li and B. Bhushan, "A review of nanoindentation continuous stiffness measurement technique and its applications," *Materials Characterization*, vol. 48, p. 11–36, February 2002.
- [78] G. M. Pharr, "Measurement of mechanical properties by ultra-low load indentation," *Materials Science and Engineering: A*, vol. 253, p. 151–159, September 1998.
- [79] W. C. Oliver and G. M. Pharr, "An improved technique for determining hardness and elastic modulus using load and displacement sensing indentation experiments," *Journal of Materials Research*, vol. 7, p. 1564–1583, June 1992.
- [80] G. M. Pharr, E. G. Herbert and Y. Gao, "The Indentation Size Effect: A Critical Examination of Experimental Observations and Mechanistic Interpretations," *Annual Review of Materials Research*, vol. 40, p. 271–292, June 2010.
- [81] M. E. Stevenson, M. Kaji and R. C. Bradt, "Microhardness anisotropy and the indentation size effect on the basal plane of single crystal hematite," *Journal of the European Ceramic Society*, vol. 22, p. 1137–1148, July 2002.
- [82] J.-i. Jang, B.-G. Yoo, Y.-J. Kim, J.-H. Oh, I.-C. Choi and H. Bei, "Indentation size effect in bulk metallic glass," *Scripta Materialia*, vol. 64, p. 753–756, April 2011.
- [83] N. Li, L. Liu and M. Zhang, "The role of friction to the indentation size effect in amorphous and crystallized Pd-based alloy," *Journal of Materials Science*, vol. 44, p. 3072–3076, June 2009.
- [84] Y. Huang, J. Shen, Y. Sun and J. Sun, "Indentation size effect of hardness of metallic glasses," *Materials & Design*, vol. 31, p. 1563–1566, 2010.
- [85] I. Manika and J. Maniks, "Size effects in micro- and nanoscale indentation," *Acta Materialia*, vol. 54, p. 2049–2056, May 2006.
- [86] H. Li and R. C. Bradt, "The indentation load/size effect and the measurement of the hardness of vitreous silica," *Journal of non-crystalline solids*, vol. 146, p. 197–212, 1992.

- [87] T. Ebisu and S. Horibe, "Analysis of the indentation size effect in brittle materials from nanoindentation load–displacement curve," *Journal of the European Ceramic Society*, vol. 30, p. 2419–2426, 2010.
- [88] R. H. Doremus, "Interdiffusion of hydrogen and alkali ions in a glass surface," *Journal of Non-Crystalline Solids*, vol. 19, p. 137–144, December 1975.
- [89] W. A. Lanford, K. Davis, P. Lamarche, T. Laursen, R. Groleau and R. H. Doremus, "Hydration of soda-lime glass," *Journal of Non-Crystalline Solids*, vol. 33, p. 249–266, June 1979.
- [90] M. Ciccotti, "Stress-corrosion mechanisms in silicate glasses," *Journal of Physics D: Applied Physics*, vol. 42, p. 214006, October 2009.
- [91] S.M. Wiederhorn and Bolz L.H., "Stress Corrosion and Static Fatigue of Glass," *Journal of the American Ceramic Society*, vol. 53, p. 543–548, October 1970.
- [92] T.-j. Chuang and E. R. Fuller, "Extended Charles-Hillig Theory for Stress Corrosion Cracking of Glass," *Journal of the American Ceramic Society*, vol. 75, p. 540–545, March 1992.
- [93] T. Akai, K. Kuraoka, D. Chen, Y. Yamamoto, T. Shirakami, K. Urabe and T. Yazawa, "Leaching Behavior of Sodium from Fine Particles of Soda-Lime-Silicate Glass in Acid Solution," *Journal of the American Ceramic Society*, vol. 88, p. 2962–2965, October 2005.
- [94] P. B. McGinnis and J. E. Shelby, "Diffusion of water in float glass melts," *Journal of Non-Crystalline Solids*, vol. 177, p. 381–388, November 1994.
- [95] J. E. Shelby, "A Limited Review of Water Diffusivity and Solubility in Glasses and Melts," *Journal of the American Ceramic Society*, vol. 91, p. 703–708, March 2008.
- [96] A. V. Bandura and S. N. Lvov, "The Ionization Constant of Water over Wide Ranges of Temperature and Density," *Journal of Physical and Chemical Reference Data*, vol. 35, p. 15–30, March 2006.
- [97] A. K. Covington, M. I. A. Ferra and R. A. Robinson, "Ionic product and enthalpy of ionization of water from electromotive force measurements," *Journal of the Chemical Society, Faraday Transactions 1: Physical Chemistry in Condensed Phases*, vol. 73, p. 1721, 1977.
- [98] N. Carmona, M. A. Villegas and J. M. F. Navarro, "Corrosion behaviour of R_2O – CaO – SiO_2 glasses submitted to accelerated weathering," *Journal of the European Ceramic Society*, vol. 25, p. 903–910, March 2005.
- [99] N. Papadopoulos and C. Drosou, "Influence of weathering conditions on glass properties," *Journal of the University of Chemical Technology and Metallurgy*, vol. 47, p. 429–439, 2012.
- [100] O. Majérus, P. Lehuédé, I. Biron, F. Alloteau, S. Narayanasamy and D. Caurant, "Glass alteration in atmospheric conditions: crossing perspectives from cultural heritage, glass industry, and nuclear waste management," *npj Materials Degradation*, vol. 4, August 2020.

- [101] M. H. Chopinet, M. Verità, R. Falcone, P. Lehuédé, M. Vallotto, M. Nardone and A. Sodo, "Soda-Lime-Silica Glass Containers: Chemical Durability and Weathering Products," *Advanced Materials Research*, Vols. 39-40, p. 305–310, April 2008.
- [102] M. Verità, R. Falcone, G. Sommariva, M. Chopinet and P. Lehuédé, "Weathering of the inner surface of soda-lime-silica glass containers exposed to the atmosphere," 2009.
- [103] T. Lombardo, A. Chabas, R.-A. Lefèvre, M. Verità and F. Geotti-Bianchini, "Weathering of float glass exposed outdoors in an urban area," *Glass technology*, vol. 46, p. 271–276, 2005.
- [104] M. Melcher, R. Wiesinger and M. Schreiner, "Degradation of glass artifacts: application of modern surface analytical techniques," *Accounts of chemical research*, vol. 43, p. 916–926, 2010.
- [105] N. P. Mellott, S. L. Brantley, J. P. Hamilton and C. G. Pantano, "Evaluation of surface preparation methods for glass," *Surface and Interface Analysis*, vol. 31, 2001.
- [106] İ. Sökmen, S. Oktik and K. Bange, *Modification Technologies of Glass Surfaces*, Wiley, 2021, p. 751–762.
- [107] S. Takeda, "Oxygen and silver diffusion into float glass," *Journal of Non-Crystalline Solids*, vol. 352, p. 3910–3913, October 2006.
- [108] U. Senturk, J. R. Varner and W. C. LaCourse, "Structure-hardness relation for high-temperature SO₂-dealkalized float glass," *Journal of Non-Crystalline Solids*, vol. 222, p. 160–166, December 1997.
- [109] J. N. de Carvalho, J. A. S. Cleaver, N. F. Kirkby and P. A. Holmes, "An experimental study of the effect of zinc treatment on float glass," *Glass Technology-European Journal of Glass Science and Technology Part A*, vol. 55, p. 14–22, 2014.
- [110] K. Hahn, "Protection of glassware in the automatic dishwashing process—a detergent manufacturer's insight and experiences," *Glass Atmospheric Alteration—Cultural Heritage, industrial and Nuclear Glasses*, p. 209–214, 2019.
- [111] S. M. Wiederhorn, "Influence of Water Vapor on Crack Propagation in Soda-Lime Glass," *Journal of the American Ceramic Society*, vol. 50, p. 407–414, August 1967.
- [112] R. J. Charles, "Static Fatigue of Glass. II," *Journal of Applied Physics*, vol. 29, p. 1554–1560, November 1958.
- [113] S. M. Wiederhorn, F. Yi, D. LaVan, L. J. Richter, T. Fett and M. J. Hoffmann, "Volume Expansion Caused by Water Penetration into Silica Glass," *Journal of the American Ceramic Society*, vol. 98, p. 78–87, October 2014.
- [114] A. Oehler and M. Tomozawa, "Water diffusion into silica glass at a low temperature under high water vapor pressure," *Journal of non-crystalline solids*, vol. 347, p. 211–219, 2004.
- [115] P. J. Lezzi, Q. R. Xiao, M. Tomozawa, T. A. Blanchet and C. R. Kurkjian, "Strength increase of silica glass fibers by surface stress relaxation: A new mechanical strengthening method," *Journal of Non-Crystalline Solids*, vol. 379, p. 95–106, November 2013.

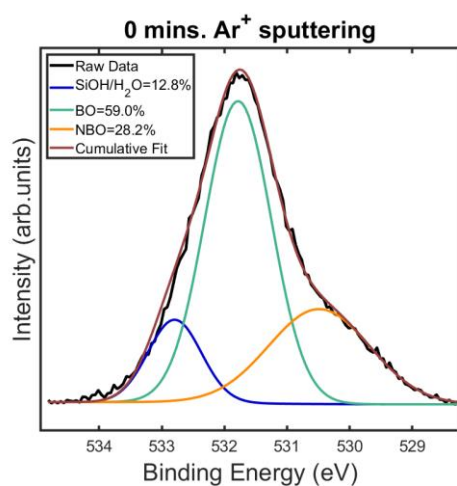
- [116] X. Liu and J. He, "One-Step Hydrothermal Creation of Hierarchical Microstructures toward Superhydrophilic and Superhydrophobic Surfaces," *Langmuir*, vol. 25, p. 11822–11826, July 2009.
- [117] R. Gardon, "Thermal tempering of glass," in *Glass Science and Technology*, New York, Academic Press, 1980, pp. 1630-1634.
- [118] V. A. Sozanski M.R., "Strengthening of glass tubes and containers by flame-sprayed glazing," *American Ceramic Society Bulletin*, vol. 66, no. 11, pp. 1630-1634, 1987.
- [119] A.K. Varsheneya, "Chemical strengthening of glass: lessons learned and yet to be learned," *International Journal of Applied Glass Science*, vol. 1, pp. 131-142, 2010.
- [120] S. Karlsson, B Jonson, C. Stalhandske, "The technology of chemical glass strengthening — a review," *Glass Technology: European Journal of Glass Science and Technology Part A*, vol. 51, pp. 41-54, 2010.
- [121] R. Gy, "Ion exchange for glass strengthening," *Materials Science and Engineering: B*, vol. 149, no. 2, pp. 159-165, 2008.
- [122] B. P. Navet B., "Glass substrate for chemical strengthening and method for chemically strengthening with controlled curvature". Patent Euro Patent EP 3181533 A1, 2017.
- [123] V.S. Veeraswamy, X. Hu and G.A. Cerny "Method of strengthening glass by plasma induced ion exchanges, and articles made according to the same". Patent World Patent WO 2013032734 A1.
- [124] C. Wang, Y. Tao and S. Wang, "Effect of nitrogen ion-implantation on silicate glasses," *Journal of non-crystalline solids*, vol. 52, pp. 589-603, 1982.
- [125] S. Bull, "Effects of ion implantation on the hardness and friction behavior of soda-lime-silica glass," *Journal of Materials Science*, vol. 27, pp. 3605-3616, 1992.
- [126] B. Aktas, M. Albaskara, K. Dogru and S. Yalcin, "Mechanical properties of soda-lime-silica glasses doped with eggshell powder," *Acta Physica Polonica A*, vol. 132, pp. 436-438, 2017.
- [127] B. Aktas, M. Albaskara, K. Dogru and S. Yalcin, "Mechanical properties of soda-lime-silica glasses with variable peanut shell contents," *Acta Physica Polonica A*, vol. 131, pp. 511-513, 2017.
- [128] İ. Erdem, D. Guldiren and S. Aydin, "Chemical tempering of soda lime silicate glasses by ion exchange process for the improvement of surface and bulk mechanical strength," *Journal of Non-Crystalline Solids*, vol. 473, pp. 170-178, 2017.
- [129] A. Fluegel, "Glass viscosity calculation based on a global statistical modelling approach," *Glass Technology-European Journal of Glass Science and Technology Part A*, vol. 48, p. 13–30, 2007.
- [130] D. A. Shirley, "High-resolution X-ray photoemission spectrum of the valence bands of gold," *Physical Review B*, vol. 5, p. 4709, 1972.

- [131] D. Pleul, R. Frenzel, M. Eschner and F. Simon, "X-ray photoelectron spectroscopy for detection of the different Si–O bonding states of silicon," *Analytical and bioanalytical chemistry*, vol. 375, p. 1276–1281, 2003.
- [132] G. Greczynski and L. Hultman, "X-ray photoelectron spectroscopy: towards reliable binding energy referencing," *Progress in Materials Science*, vol. 107, p. 100591, 2020.
- [133] E. Moayedi and L. Wondraczek, "Quantitative analysis of scratch-induced microabrasion on silica glass," *Journal of Non-Crystalline Solids*, vol. 470, p. 138–144, August 2017.
- [134] H. Yamanaka, M. Yamashita, J. Matsuoka, H. Wakabayashi and R. Terai, "Depth profiling by XPS for corroded glass," *Journal of Non-Crystalline Solids*, vol. 116, p. 286–288, February 1990.
- [135] M. E. Simonsen, C. Sønderby, Z. Li and E. G. Søggaard, "XPS and FT-IR investigation of silicate polymers," *Journal of Materials Science*, vol. 44, p. 2079–2088, April 2009.
- [136] B. Roy, A. Rosin, T. Gerdes and S. Schafföner, "Revealing the surface structural cause of scratch formation on soda-lime-silica glass," *Scientific Reports*, vol. 12, February 2022.
- [137] B. Roy, F. Baier, A. Rosin, T. Gerdes and S. Schafföner, "Structural characterization of the near-surface region of soda–lime–silica glass by X-ray photoelectron spectroscopy," *International Journal of Applied Glass Science*, vol. 14, pp. 229-239, 2023.
- [138] L. Wondraczek, J. C. Mauro, J. Eckert, U. Kühn, J. Horbach, J. Deubener and T. Rouxel, "Towards Ultrastrong Glasses," *Advanced Materials*, vol. 23, p. 4578–4586, September 2011.
- [139] T. Suzuki, T. Sekine, K. Yamamoto and K. Fukutani, "Change in the surface OH group on soda lime silicate glass and silica glass after heat treatment in nitrogen atmosphere," *Journal of Non-Crystalline Solids*, vol. 464, pp. 89-91, 2017.
- [140] S. Takeda, K. Yamamoto, Y. Hayasaka and K. Matsumoto, "Surface OH group governing wettability of commercial glasses," *Journal of non-crystalline solids*, vol. 249, pp. 41-46, 1999.
- [141] B. Reif, S.E. Ashbrook, L. Emsley and M. Hong, "Solid-state NMR spectroscopy," *Nature Reviews Methods Primers*, vol. 1, January 2021.
- [142] E.F. Vasant, P.V.D. Voort and K.C. Vrancken, "Chapter 5 The distribution of the silanol types and their desorption energies," in *Studies in Surface Science and Catalysis*, Elsevier, 1995, p. 93–126.
- [143] L. T. Zhuravlev, "The surface chemistry of amorphous silica. Zhuravlev model," *Colloids and Surfaces A: Physicochemical and Engineering Aspects*, vol. 173, p. 1–38, November 2000.
- [144] D. C. Cornish, *The properties of glass surfaces: By L. Holland, Chapman and Hall, London, 1964, pp. xvi+ 546, 80s. Net in UK only, Pergamon, 1964.*
- [145] H. H. Dunken, "Glass surfaces," in *Treatise on Materials Science & Technology*, vol. 22, Elsevier, 1982, p. 1–74.

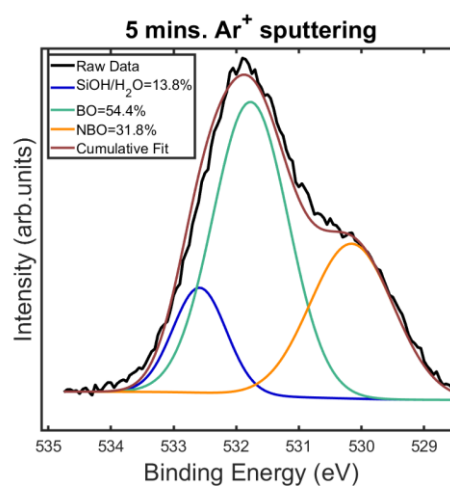
[146] T. M. Gross, A. R. Sarafian, J. Wu and Z. Zheng, "Glass compositions and methods for strengthening via steam treatment". US Patent WO 2020/102127 A2, 2020.

Appendix A1

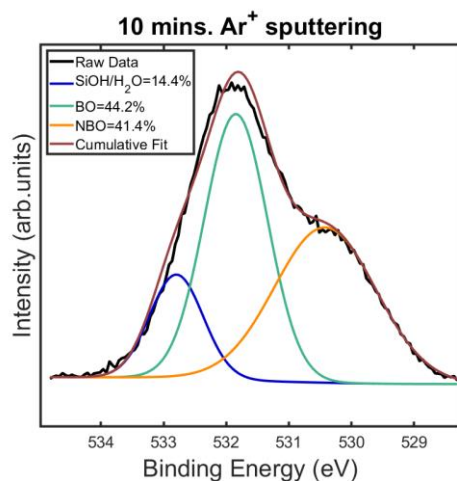
XPS O1s & Si2p curve-fittings of untreated and steam-treated SLS glass surfaces are presented in this section. 90% Gaussian-10% Lorentzian composite function was used to obtain the best fits in terms of lowest chi-squared values.



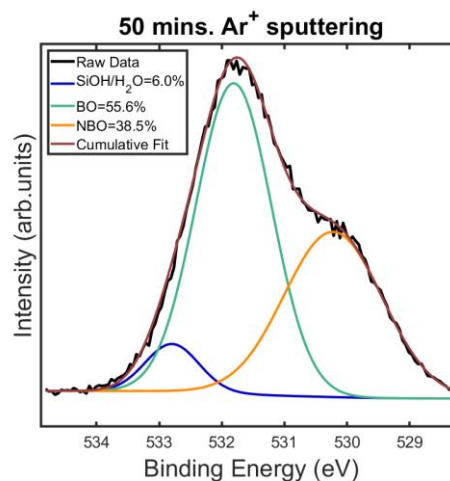
(a)



(b)



(c)



(d)

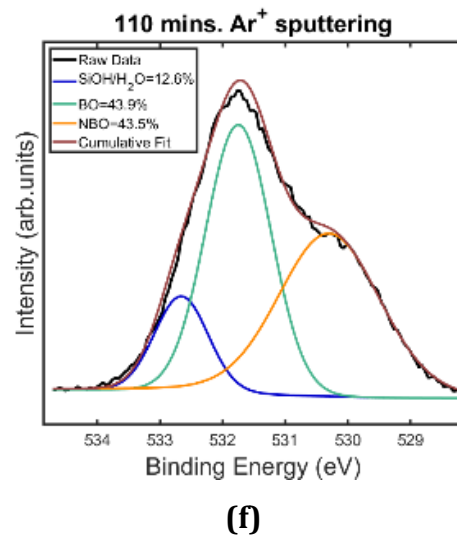
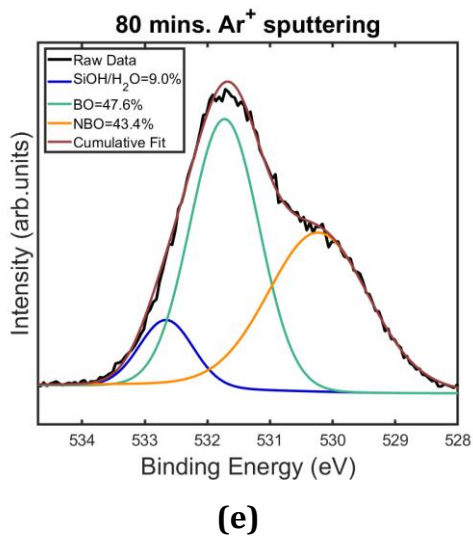
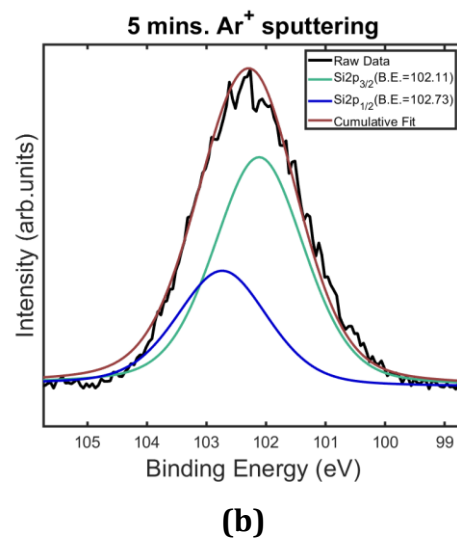
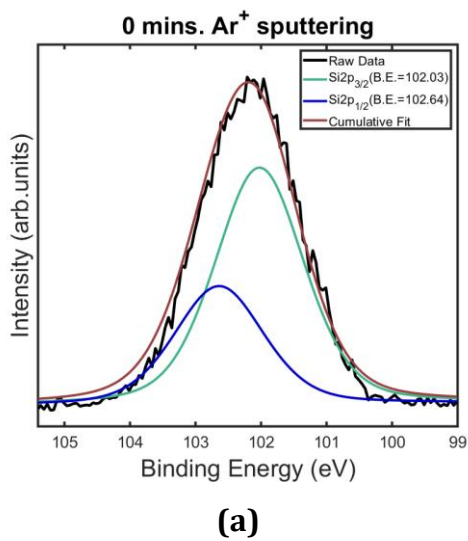


Figure A1.1 Gaussian-Lorentzian curve-fits of O1s spectral lines of untreated container glass surface as a function of Ar⁺ sputtering time (i) 0 min. (ii) 5 min. (iii) 10 min. (iv) 50 min. (v) 80 min. (vi) 110 min.



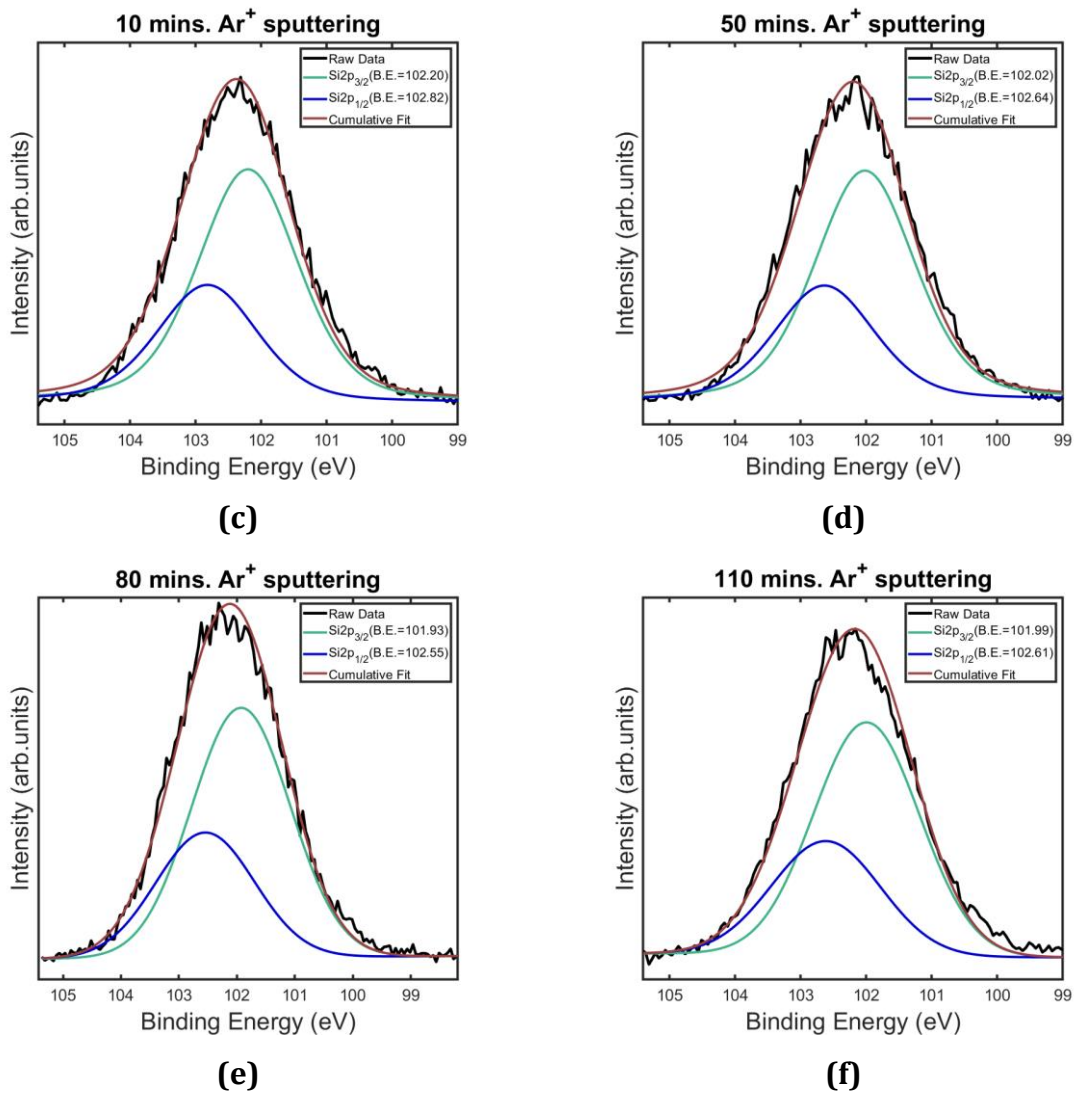


Figure A1.2 Curve-fitted Si2p spectral lines of untreated container glass surface as a function of Ar⁺ sputtering time (i) 0 min. (ii) 5 min. (iii) 10 min. (iv) 50 min. (v) 80 min. (vi) 110 min.

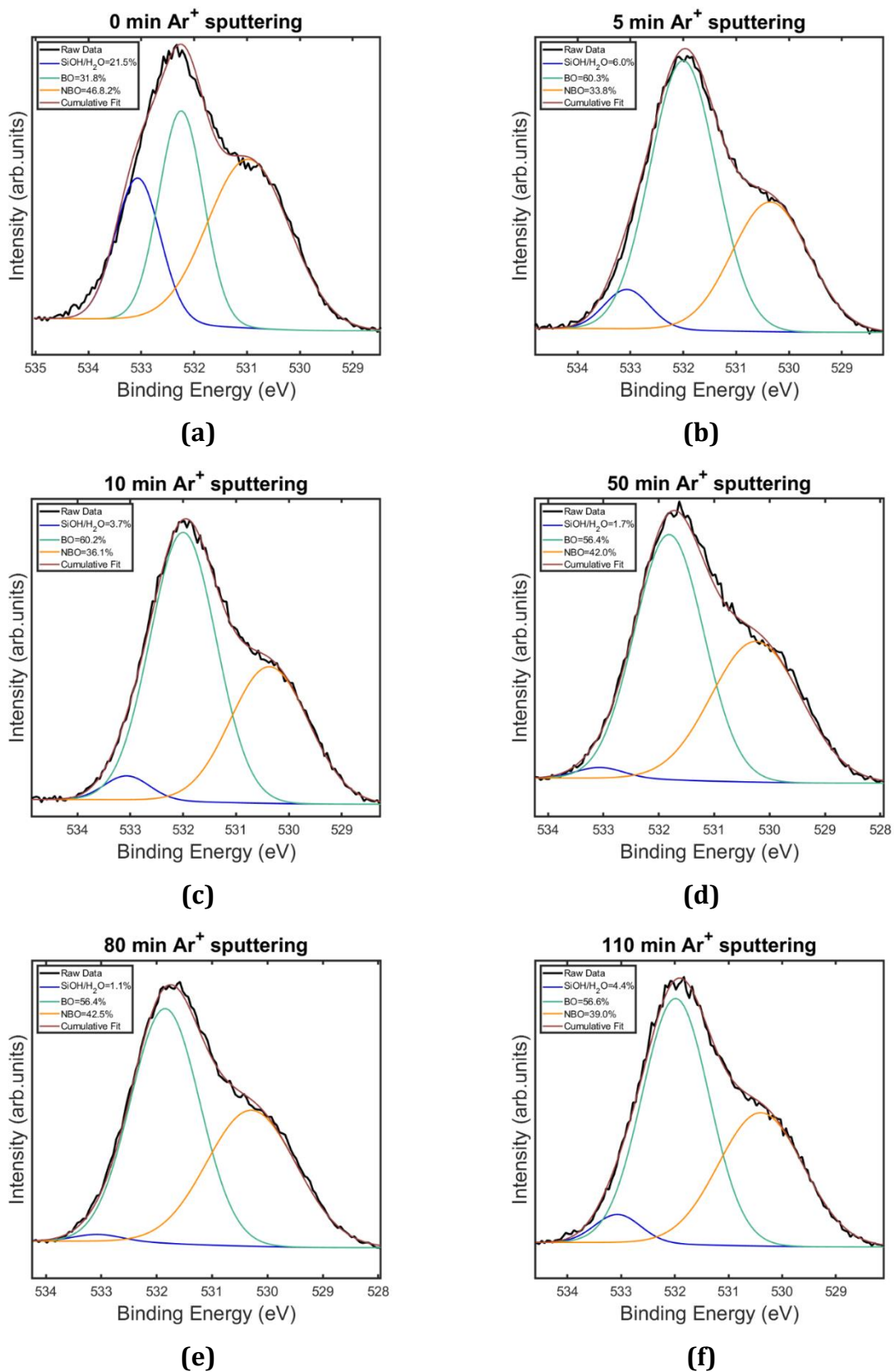


Figure A1.3 O1s curve fittings of sub-T_g steam-treated container glass surface as a function of Ar⁺ sputtering time (a) 0 min. (b) 5 min. (c) 10 min. (d) 50 min. (e) 80 min. (f) 110 min.

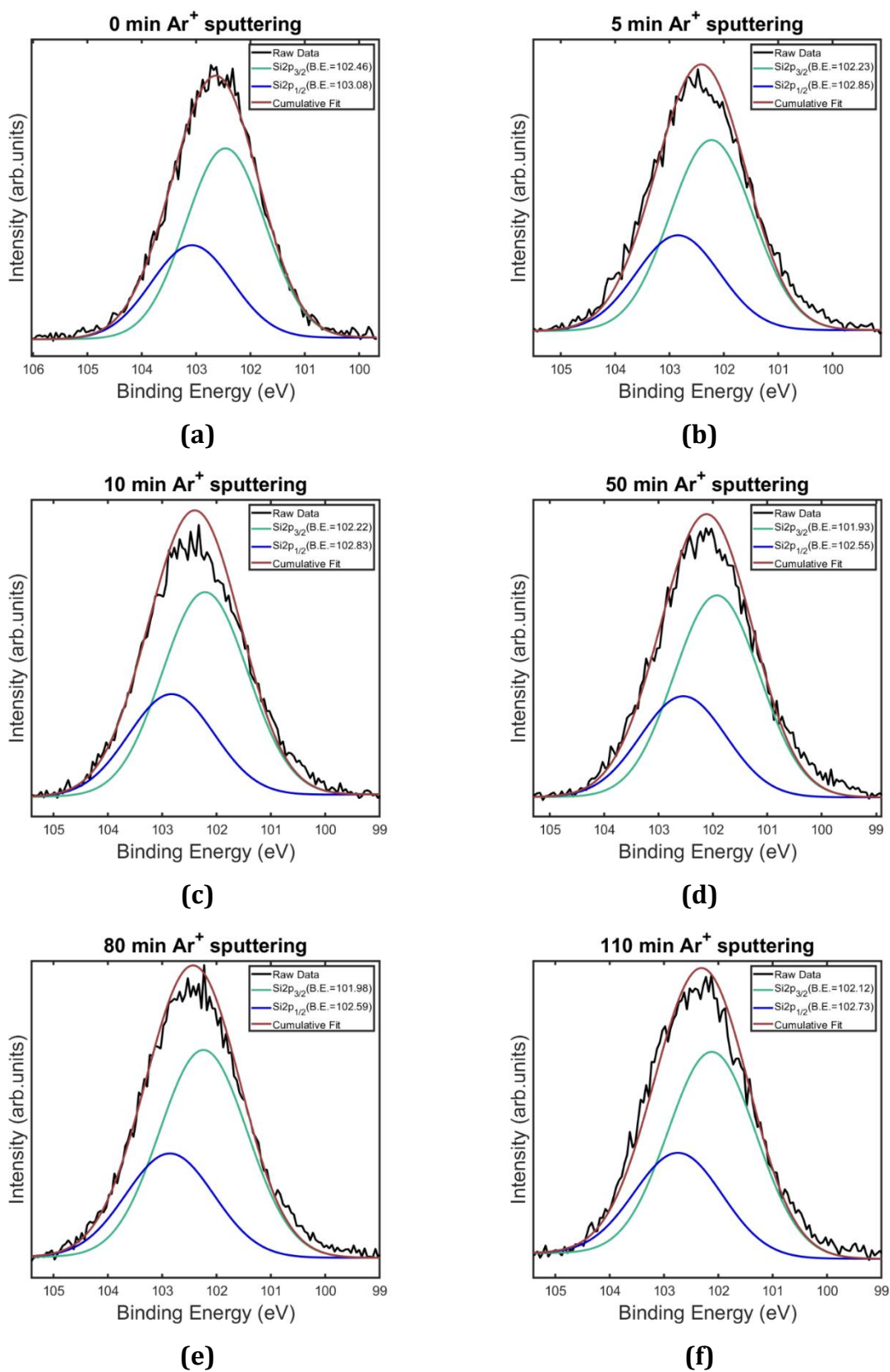


Figure A1.4 Si2p curve-fittings of steam-treated container glass surface as a function of Ar⁺ sputtering time (a) 0 min. (b) 5 min. (c) 10 min. (d) 50 min. (e) 80 min. (f) 110 min.

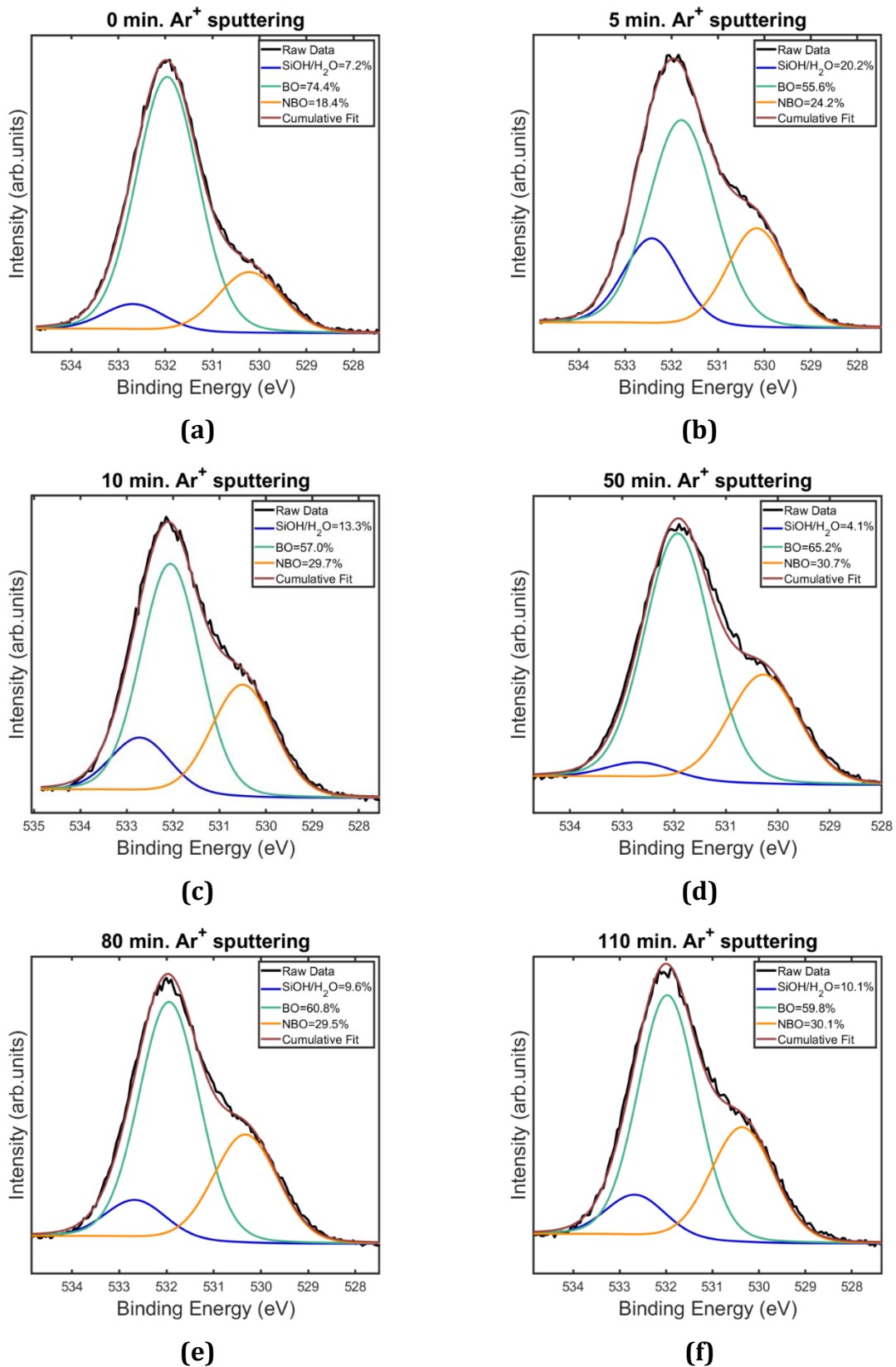


Figure A1.5 O1s curve fittings of untreated microscopic glass slide surface as a function of Ar⁺ sputtering time (a) 0 min. (b) 5 min. (c) 10 min. (d) 50 min. (e) 80 min. (f) 110 min.

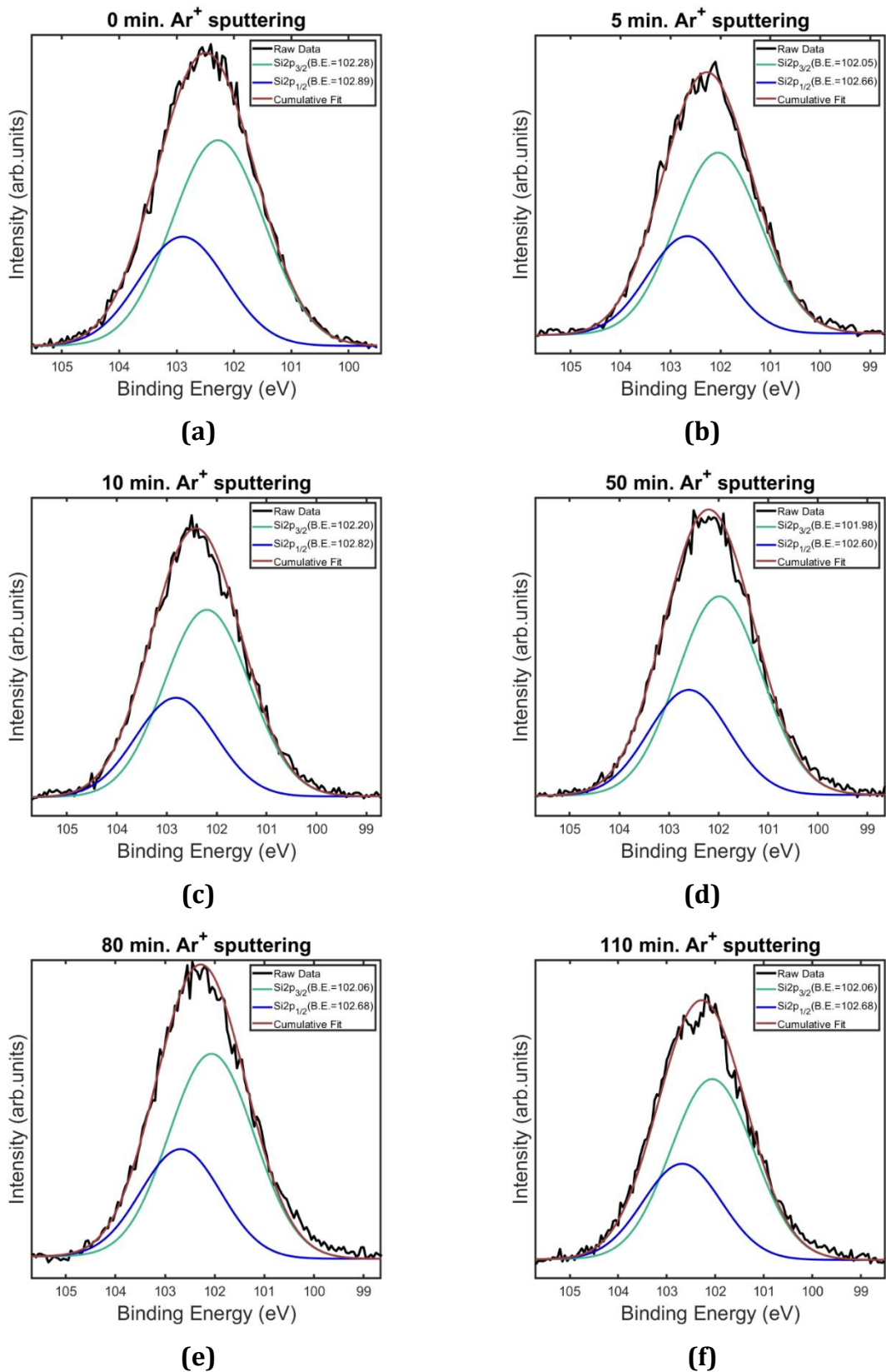
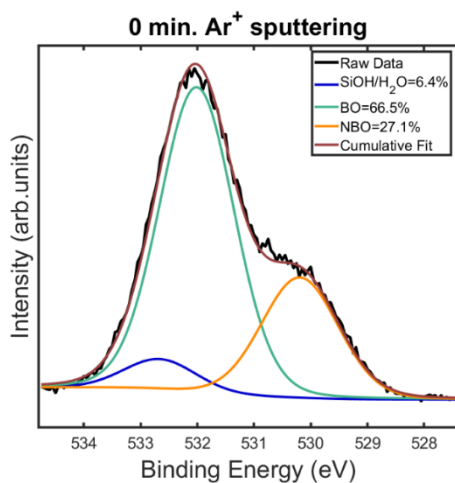
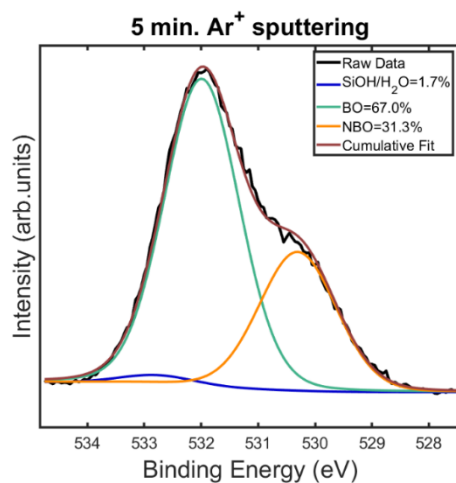


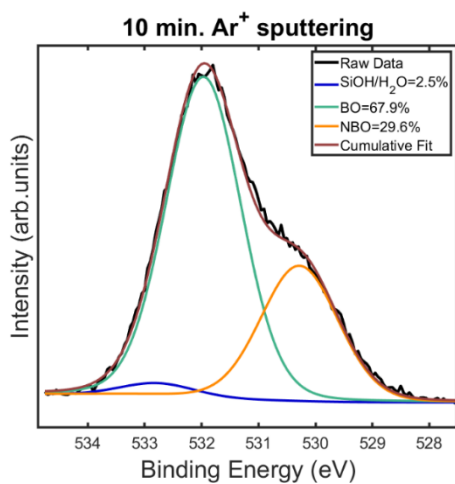
Figure A1.6 Si2p curve-fittings of untreated microscopic glass slide as a function of Ar⁺ sputtering time (a) 0 min. (b) 5 min. (c) 10 min. (d) 50 min. (e) 80 min. (f) 110 min.



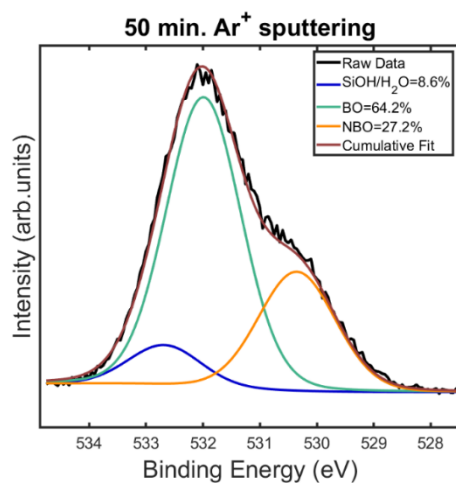
(a)



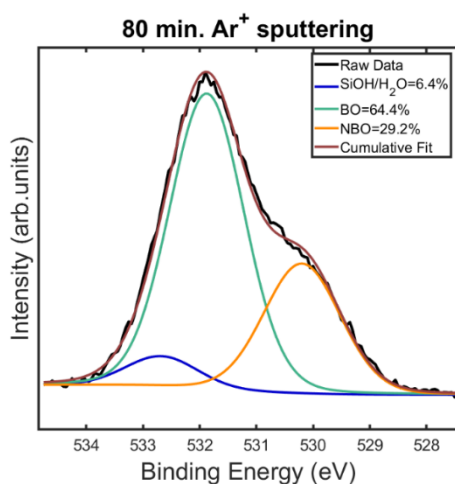
(b)



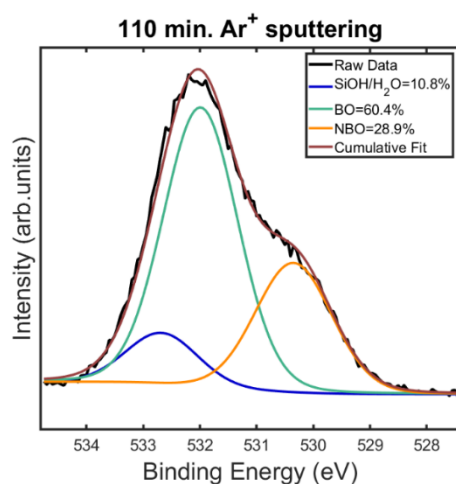
(c)



(d)

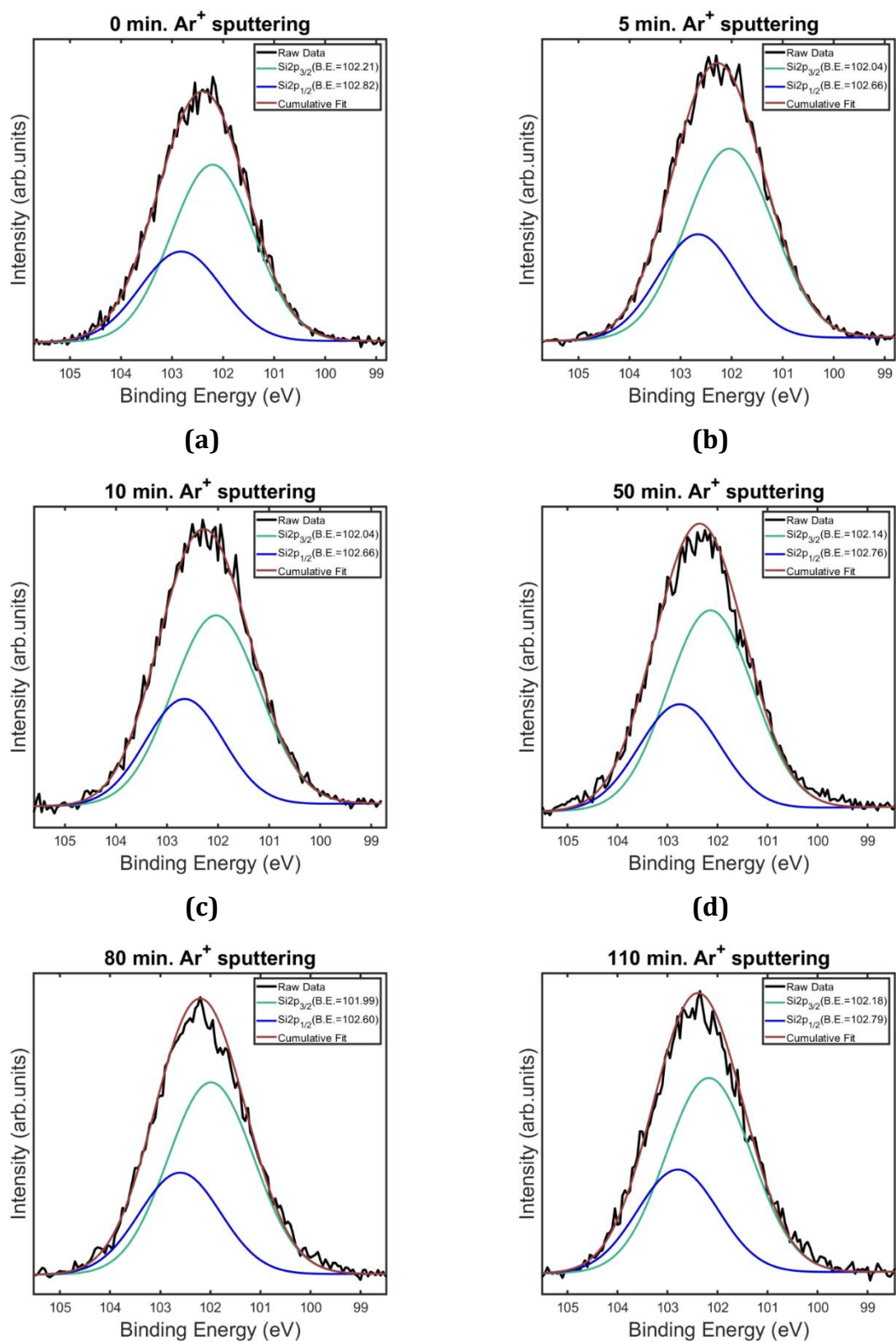


(e)



(f)

Figure A1.7 O1s curve-fittings of superheated steam-treated microscopic glass slides as a function of Ar⁺ sputtering time (a) 0 min. (b) 5 min. (c) 10 min. (d) 50 min. (e) 80 min. (f) 110 min.



(e)

(f)

Figure A1.8 Si2p spectral fits of steam-treated microscopic glass slide surfaces as a function of Ar⁺ sputtering time (a) 0 min. (b) 5 min. (c) 10 min. (d) 50 min. (e) 80 min. (f) 110 min.

Appendix A2

The failure stresses of the untreated, heat-treated (H510) and steam-treated (S510) container SLS glasses were characterized by ring-on-ring tests. Figure A2.1 illustrates the comparative plot of the failure stress against the probability of failure of the three categories of SLS specimens. 15 samples of each category were subjected to the test.

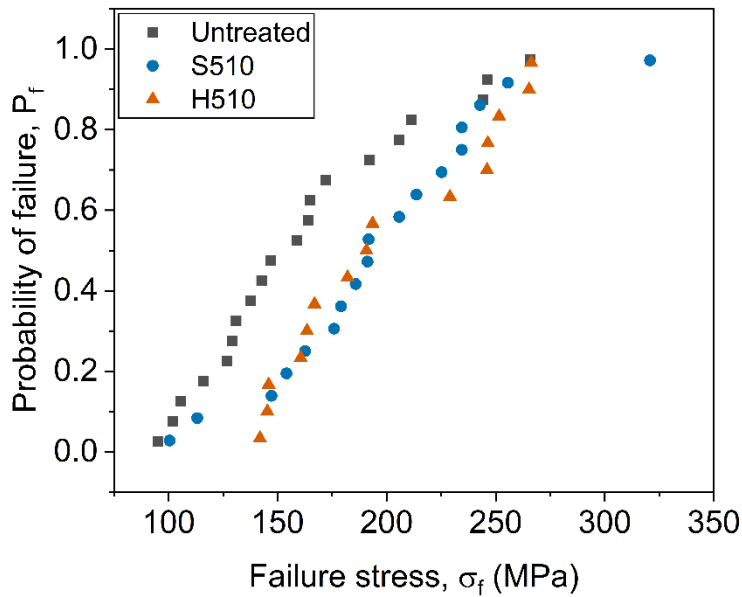


Figure A2.1 Failure stress vs probability of failure of untreated, H510 and S510 container SLS specimens

The corresponding parameters of the mean strengths ($P_f= 50\%$), characteristic strengths ($P_f= 63.2\%$) and Weibull moduli are tabulated in Table A2.1.

Table A2.1 Mean strength, characteristic strength and Weibull modulus of untreated, H510 and S510

Specimen	Mean Strength (in MPa) (Probability of Failure, $P_f = 50\%$)	Characteristic Strength (in MPa) (Probability of Failure, $P_f = 63.2\%$)	Weibull Modulus
Untreated	162.8	180.2	3.94
H510	196.3	217.7	4.30
S510	199.6	217.9	4.92

The evidence of the increase in the mean strength by approximately 20% is true for both the heat-treated (H510) and steam-treated (S510) specimens. This signifies the absence of any additional strengthening effect by the influence of superheated steam. This is in accordance with the expectations due to the absence of any ion-exchange reaction (see Section 3.2.2, Figure 3.9). Therefore, the marginal increase in strength is attributed to the “heat-strengthening” effect, analogous to annealing, at sub- T_g temperature of 510 °C for 30 minutes.

List of Figures

Figure 1.1. Two-dimensional schematic representation of soda-lime-silica glass structure. A fourth oxygen would be located above each silicon atom in the three-dimensional structure

Figure 1.2. Schematic representation of (a) isolated silanol (b) vicinal silanol (c) geminal silanol (d) non-interacting silanol. Si (yellow), O (red), H (gray)

Figure 1.3. Relationship between O-H stretching frequency and H...O distance in solid materials

Figure 1.4. Schematic representation of the glass network structure near a surface

Figure 1.5. Schematic illustration of the energy level diagram of XPS

Figure 1.6. (a) Basic instrumental setup of XPS [© 2023 Physical Electronics, Inc. (PHI)]
(b) PHI 5000 Versa Probe III

Figure 1.7. Failure strengths of glass products as a function of flaw size

Figure 1.8. Resultant cracking systems of Vickers indentation

Figure 1.9. Schematic representation of the indentation deformation stages. The dashed line indicates the indentation profile after unloading. Arrows indicate matter displacement. σ is the mean contact pressure

Figure 1.10. (a) Typical load-displacement curve illustrating the loading and unloading cycle during indentation (b) Physical processes involved in indentation

Figure 1.11. Model of the hydrated layers on the surface of alkali silicate glasses

Figure 1.12. Glass weathering process starting with (a) clean surface (b) formation of a water film (c) a leached layer containing hydrogen (d) crystalline weathering products on the glass surface

Figure 2.1. Determination of glass transition region (T_g) of the studied soda-lime-silica glasses by dilatometry (a) container glass (b) glass slide

Figure 2.2 Viscosity vs temperature curve of container glass and glass slide obtained by BatchMaker software

Figure 2.3 Process schematic of the experimental setup of superheated steam treatment

Figure 3.1 Variation of subsurface hardness of container SLS glass as a function of temperature and duration of superheated steam treatment. The applied load was 10 mN

Figure 3.2 Variation of hardness as a function of depth from the SLS glass surfaces (a) container glass (b) glass slide. Peak load: 10 mN

Figure 3.3 Variation of hardness of container SLS glass as a function of load

Figure 3.4 SEM images of the scratches generated at a load of 5 N on (a) untreated (b) heat-treated (c) steam-treated container SLS glass surfaces

Figure 3.5 ATR-IR spectra of (a) untreated and (b) S510 container SLS surfaces. Gaussian function was used for curve-fitting (R-square > 0.9)

Figure 3.6 Gaussian curve-fitted ATR-IR spectra of SLS glass slide (a) untreated (b) S460

Figure 3.7 Assignment of ATR-IR peaks to specific OH vibrations

Figure 3.8 Comparative illustration of the curve-fitted ATR-IR spectra of steam-treated (a) container glass (S510) (b) glass slide (S460)

Figure 3.9 Elemental depth profile of container glass surface (a) untreated (b) steam-treated (S510); glass slide (c) untreated (d) steam-treated (S460)

Figure 3.10. Typical illustration of (a) O1s and (b) Si2p curve-fittings by Gaussian-Lorentzian function

Figure 3.11 Variation of the atomic ratio of individual oxygen speciations to silicon, as a function of Ar⁺ sputtering time (below); variation of atomic ratio of total oxygen (sum of individual contributions) to silicon, as a function of Ar⁺ sputtering time (above) (a) untreated container glass surface (b) steam-treated container glass surface (S510). Connecting lines act as guideline to the eyes

Figure 3.12 Variation of the atomic ratio of individual oxygen speciations to silicon, as a function of Ar⁺ sputtering time (below); variation of atomic ratio of total oxygen (sum of individual contributions) to silicon, as a function of Ar⁺ sputtering time (above) (a) untreated glass slide surface (b) steam-treated glass slide surface (S460). Connecting lines act as guideline to the eyes

Figure 3.13 Variation of the atomic ratio of individual oxygen speciations to silicon, as a function of Ar⁺ sputtering time (below); variation of atomic ratio of total oxygen (sum of

individual contributions) to silicon, as a function of Ar⁺ sputtering time (above). Connecting lines act as guideline to the eyes. **(a)** sub-T_g steam-treated container glass surface (S510) **(b)** sub-T_g steam-treated microscopic glass slide surface (S460)

Figure 3.14 Difference in the increase in BO/Si and NBO/Si caused by the influence of superheated steam. Here, BO: O_{Si-O-Si} and NBO: O_{Si-O-Na} + O_{SiOH/H₂O}. Positive values indicate repolymerized network after steam-treatment, while negative values are indicative of depolymerized silicate network

Figure 3.15 Atomic ratio of total oxygen to silicon (O_{Total}/ Si) of untreated, heat-treated and steam-treated (a) container glass (b) glass slide as a function of Ar⁺ sputtering time

Figure 3.16 1x1 μm² third order flattened three-dimensional AFM images of (a) untreated (b) steam-treated container glass surface

Figure 3.17 Comparative surface profile heights as a function of lateral distance across the same surface diagonal of Figure 3.20 (a) and (b), from top-left to bottom-right

Figure 3.18 Comparative histogram representation of the distribution of void depths within the surface network of untreated and steam-treated specimens (S510)

Figure 3.19 Static contact angle of water on (a) untreated (b) steam treated (S510) SLS container glass surface. Volume of water droplet: 2.5μL

Figure 3.20 ²⁹Si MAS NMR spectral fits of (a) untreated and (b) sub-T_g steam-treated container SLS glass

Figure 3.21 ²⁹Si MAS NMR spectral fits of (a) untreated and (b) sub-T_g steam treated SLS glass slide

Figure 3.22 Evolution of subsurface hardness with ageing in ambient atmosphere (a) container glass (b) glass slide. Applied load: 10 mN. ANOVA single factor test: p<0.001 : ***

Figure 3.23 Variation of the atomic ratio of individual oxygen speciations to silicon, as a function of Ar⁺ sputtering time (below); variation of atomic ratio of total oxygen (sum of individual contributions) to silicon, as a function of Ar⁺ sputtering time (above) (a) steam-treated container glass surface (S510) (b) steam-treated container glass surface after 1 week of ageing in ambient atmosphere. Connecting lines act as a guideline to the eyes

Figure 3.24 Surface structural schematic representation of **(a)** untreated **(b)** sub- T_g steam-treated container glass **(c)** sub- T_g steam treated glass slide

Figure A1.1 Gaussian-Lorentzian curve-fits of O1s spectral lines of untreated container glass surface as a function of Ar⁺ sputtering time (i) 0 min. (ii) 5 min. (iii) 10 min. (iv) 50 min. (v) 80 min. (vi) 110 min.

Figure A1.2 Curve-fitted Si2p spectral lines of untreated container glass surface as a function of Ar⁺ sputtering time (i) 0 min. (ii) 5 min. (iii) 10 min. (iv) 50 min. (v) 80 min. (vi) 110 min.

Figure A1.3 O1s curve fittings of sub- T_g steam-treated container glass surface as a function of Ar⁺ sputtering time (a) 0 min. (b) 5 min. (c) 10 min. (d) 50 min. (e) 80 min. (f) 110 min.

Figure A1.4 Si2p curve-fittings of steam-treated container glass surface as a function of Ar⁺ sputtering time (a) 0 min. (b) 5 min. (c) 10 min. (d) 50 min. (e) 80 min. (f) 110 min.

Figure A1.5 O1s curve fittings of untreated microscopic glass slide surface as a function of Ar⁺ sputtering time (a) 0 min. (b) 5 min. (c) 10 min. (d) 50 min. (e) 80 min. (f) 110 min.

Figure A1.6 Si2p curve-fittings of untreated microscopic glass slide as a function of Ar⁺ sputtering time (a) 0 min. (b) 5 min. (c) 10 min. (d) 50 min. (e) 80 min. (f) 110 min.

Figure A1.7 O1s curve-fittings of superheated steam-treated microscopic glass slides as a function of Ar⁺ sputtering time (a) 0 min. (b) 5 min. (c) 10 min. (d) 50 min. (e) 80 min. (f) 110 min.

Figure A1.8 Si2p spectral fits of steam-treated microscopic glass slide surfaces as a function of Ar⁺ sputtering time (a) 0 min. (b) 5 min. (c) 10 min. (d) 50 min. (e) 80 min. (f) 110 min.

Figure A2.1 Failure stress vs probability of failure of untreated, H510 and S510 container SLS specimens

List of Tables

Table 2.1 Characteristic points on the viscosity-temperature curves of the SLS glasses, estimated by the BatchMaker software

Table 3.1 Comparative variation of the atomic ratios of different oxygen species (BO, NBO, hydrous species) to silicon as a function of Ar⁺ sputtering time before (UT: untreated) and after superheated steam treatment of the container SLS glass at 510 °C for 30 minutes (S510)

Table 3.2 Comparative variation of the atomic ratios of different oxygen species (BO, NBO, hydrous species) to silicon as a function of Ar⁺ sputtering time before (UT: untreated) and after superheated steam treatment of SLS glass slide at 460 °C for 30 minutes (S460)

Table A2.1 Mean strength, characteristic strength and Weibull modulus of untreated, H510 and S510

List of peer-reviewed publications in journals

- B. Roy, A. Rosin, T. Gerdes, S. Schafföner. Revealing the surface structural cause of scratch formation on soda-lime-silica glass. *Sci Rep* **12**, 2681 (2022).
- B. Roy, F. Baier, A. Rosin, T. Gerdes, S. Schafföner. Structural characterization of the near-surface region of soda-lime-silica glass by X-ray photoelectron spectroscopy. *Int. J. Appl. Glass Sci.* **14**, 229-239 (2023).
- B. Roy, A. Rosin, T. Gerdes, S. Schafföner. Transient subsurface hardening of soda-lime-silica glass by superheated steam. *Glass Technol.: Eur. J. Glass Sci. Technol., Part A*, **64 (6)**, 185-196 (2023).

List of conference presentations

- Roy B, Rosin A, Gerdes T. Modification of soda-lime-silica glass surface by high temperature steam treatment. 94th Conference on Glass Technology, online (10th-12th May 2021)
- Roy B, Rosin A, Gerdes T, Schafföner S. Effect of fictive temperature on surface structural chemistry of soda-lime-silica glass. 26th International Congress on Glass, Berlin, Germany (3rd-8th July 2022)
- Roy B, Rosin A, Gerdes T, Schafföner S. Transient subsurface hardening of soda-lime-silica glass accompanied by surface network depolymerization caused by superheated steam. 26th International Congress on Glass, Berlin, Germany (3rd-8th July 2022)
- Roy B, Rosin A, Gerdes T, Schafföner S. Relationship between subsurface hardness and silicate network connectivity of soda-lime-silica glass modified by superheated steam. USTV-DGG Joint Annual Meeting, Orléans, France (22nd-24th May 2023)
- B. Roy, A. Rosin, T. Gerdes. Vulnerability of superheated steam-treated soda-lime-silica glass surface to ageing in ambient atmosphere. Society of Glass Technology Annual Conference, Murray Edwards College, Cambridge, UK (4th-6th September 2023)

Curriculum vitae

Personal Information

FIRST NAME / SURNAME	Barsheek Roy
ADDRESS	Karlsruher Weg 24, 76185 Karlsruhe, Germany
TEL	+49 176 320 40029
EMAIL	roy.phdadm@gmail.com roy.barsheek@kit.edu
NATIONALITY	Indian
CURRENT RESIDENCE	Germany (since 2019)
DATE OF BIRTH	03.07.1995
GENDER	Male

Education and Training

DATE	September 2019 - April 2024
QUALIFICATION	PhD (Dr.-Ing.)
PRINCIPAL STUDIES	Materials Engineering
TITLE OF THESIS	Surface modification of soda-lime-silica glass by superheated steam
INSTITUTION	Keylab Glass Technology, University of Bayreuth, Germany
DATE	July 2018 - June 2019
QUALIFICATION	Master of Technology (M. Tech)
PRINCIPAL STUDIES	Ceramic Engineering Specialization: Industrial Ceramics
TITLE OF THESIS	Effect of alumina and aluminosilicate thin film on different physical properties of soda-lime-silica glass
INSTITUTION	National Institute of Technology, Rourkela, India
DATE	August 2014 - June 2018
QUALIFICATION	Bachelor of Technology (B. Tech) with Honours
PRINCIPAL STUDIES	Ceramic Engineering
INSTITUTION	National Institute of Technology, Rourkela, India

Work Experience

DATE September 2019 - March 2024
POSITION Research Assistant
ROLE Glass development scientist – Strengthening and sustainable production of silicate glasses
EMPLOYER Keylab Glass Technology, University of Bayreuth

DATE June 2024 - present
POSITION Postdoctoral researcher
ROLE Development of lithium orthosilicate based ceramic pebbles for tritium breeding blanket in nuclear fusion reactors
EMPLOYER Institute of Applied Materials, Karlsruhe Institute of Technology

First-author publications

- Revealing the surface structural cause of scratch formation on soda-lime-silica glass. Scientific Reports (2022). <https://doi.org/10.1038/s41598-022-06649-y>
- Structural characterization of the near-surface region of soda-lime-silica glass by X-ray photoelectron spectroscopy. International Journal of Applied Glass Science (2023). <https://doi.org/10.1111/ijag.16604>
- Transient subsurface hardening of soda-lime-silica glass by superheated steam. European Journal of Glass Science and Technology Part A (2023). <https://doi.org/10.13036/17533546.64.6.007>

Awards

Academic Excellence Award and Silver Medal (2020): National Institute of Technology, Rourkela, India

Skills and Competences

LABORATORY SKILLS Melt-quenching glasses, XPS, NMR, FTIR, Raman, AFM, SEM, LSM, XRD, DSC, DTA, STA, hardness, strength

LANGUAGES SPOKEN English (native), Bengali (bilingual), Hindi, German (A1)

SOCIAL SKILLS & COMPETENCES Fluent communication and advanced writing skills in English, MS office, Origin, C++, open water scuba diver, open-minded, flexible to relocate, adaptability